Dynamics of coupled nanomechanical pillar resonators

Dissertation submitted
for the degree of Doctor of Natural Sciences
(Dr.rer.nat.)

presented by

Juliane Doster

at the

Faculty of Sciences

Department of Physics

Date of oral examination: 10.02.2021
1. Reviewer: Prof. Dr. E. Weig
2. Reviewer: Prof. Dr. E. Scheer

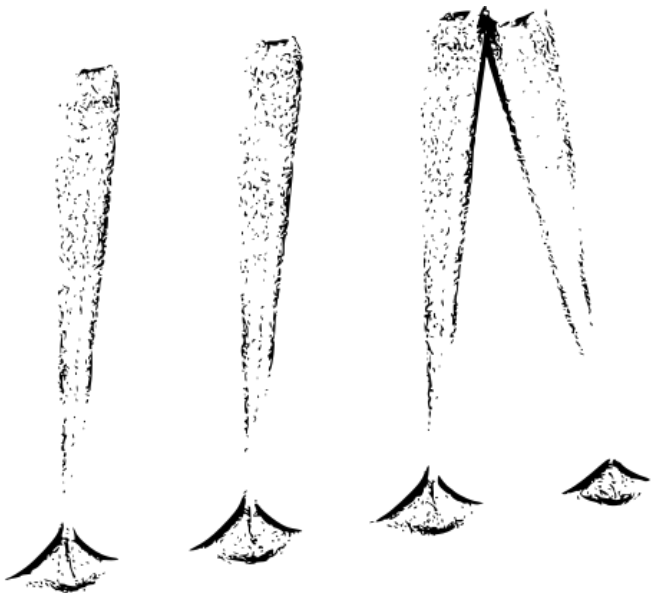

Zusammenfassung

Im Rahmen dieser Arbeit wird die Kopplung von nanomechanischen Säulenresonatoren untersucht. Eine vertikal aufgestellte Nanosäule aus Galliumarsenid weist zwei orthogonale Biegemoden auf. Da benachbarte Säulen im gleichen Substrat verankert sind, kann durch Verspannungen Energie zwischen den Säulen ausgetauscht werden. Diese intrinsische Kopplung zusammen mit einer einfachen Herstellung von kompakten Säulenfeldern machen das System ideal zur Untersuchung von Kopplungsphänomenen.

Zunächst wird das Wissen über einzelne Nanosäulen ausgebaut. Dabei wird neben einem etablierten theoretischen Modell ein Simulationsmodell erstellt basierend auf der Finite-Elemente-Methode. Die Ergebnisse der Simulationen zeigen sehr gute Übereinstimmung mit dem theoretischen Modell. Statistische Messungen von einzelnen Nanosäulen erlauben im Weiteren ein tieferes Verständnis des Herstellungsprozesses. So kann die Asymmetrie einer Nanosäule die Homogenität der Frequenzen in einem Säulenfeld verschlechtern, während gleichzeitig der Ätzprozess zu einem systematischen Frequenzgradienten in einem Säulenfeld führt. Hier können deutliche Verbesserungen im Herstellungsprozess erzielt werden. Zudem können die Resonanzfrequenzen der Säulen nachträglich durch laserinduzierte Frequenzverstimmung angepasst werden.

Im Folgenden wird starke Kopplung zwischen Pärchen von Nanosäulen, induziert durch eine Verspannung des Substrats, nachgewiesen. Hierzu kann sowohl Evidenz von hybridisierten Moden zwischen Nanosäulen als auch eine kopplungsinduzierte Aufspaltung von entarteten Moden gefunden werden. Die Modenaufspaltung erlaubt die Bestimmung der Kopplungsstärke für verschiedene Geometrien. Dadurch kann, erhärtet durch Simulationen, eine Geometrieabhängigkeit der Kopplungsstärke gefunden werden. So haben der Säulenabstand, deren Radius und die Höhe Einfluss auf die Kopplungsstärke.

Schließlich werden im letzten Teil Felder von mehreren hundert Nanosäulen untersucht. Zur Untersuchung dieser Felder wird eine Methode zur Abbildung von schwingenden Nanosäulen verwendet, die hochauflösende Abbildungen innerhalb eines großen Sichtfeldes erlaubt. Eine automatisierte Bildauswertungsmethode ermöglicht es, Bilder bei einer Großzahl verschiedener Frequenzen effektiv auszuwerten. Die untersuchten Felder zeigen deutliche Zeichen kollektiver Moden. Dabei können in einem Feld die beiden Schwingungspolarisationen einer Säule getrennt voneinander gekoppelt sein. In einem anderen

Feld gibt es einen Überlapp der Schwingungspolarisationen. Das führt zu komplexen Bewegungsmustern, in denen sogar elliptische Bahnen gefunden werden können. Dadurch könnte man in weiteren Messungen sogar topologische Polarisationssingularitäten von rein kreisförmigen und rein linearen Inseln (*C points* und *L lines*) im Feld finden.

Abstract

In this thesis, coupled modes of nanomechanical pillar resonators are investigated. Vertically oriented gallium arsenide (GaAs) nanopillars inhibit two orthogonal flexural modes. Neighboring pillars being clamped on the same substrate are able to exchange energy through their clamping points. This intrinsic coupling mechanism together with the possibility of dense integration into arrays makes nanomechanical pillars ideally suited for the examination of collective dynamics.
In a first step, control and understanding of a single pillar is achieved. A finite element simulation model, which is extensively studied and compared with measurements, complements the existing theoretical model. Further, understanding of the fabrication characteristics that may influence a possible collective behavior is obtained by statistical measurements. They reveal a slight random asymmetry in the pillar circularity as well as a systematic frequency gradient in pillar arrays due to a diffusion limited etch process. They both are addressed and improved in fabrication optimizations. Further control over a nanopillar is gained by establishing a laser-induced frequency tuning mechanism.
Strong strain-induced coupling is demonstrated in pairs of nanomechanical pillar resonators. Evidence of mode hybridization and avoided level crossings allow for the identification as well as characterization of the coupling mechanism. Finite element simulations and measurements show a dependence of the coupling strength on geometrical parameters, such as the pillar distance, their radius as well as their height.
In the final part, arrays of hundreds of nanomechanical pillar resonators are examined. An advanced imaging detection scheme is set up to allow for well-resolved imaging of large pillar arrays and their vibration patterns. An automatized image evaluation algorithm enables practical analysis of large frequency sweeps. The arrays show signatures of collective behavior. I observe coupled mode patterns with strict separation of the two polarizations in one array, as well as mixed vibration patterns of coupled pillars showing different polarization directions and elliptical trajectories in a second array. This paves the way towards the detection of topological polarization singularities called L lines and C points.

Contents

CHAPTER 1

INTRODUCTION

The conductor of an orchestra gives a beat and with that he keeps the orchestra in time. One could say, the conductor is the visible link between every member of an orchestra to keep them synchronized. Some 350 years ago, Huygens observed that two pendulum clocks hanging from the same structure move in unison just as the players in the orchestra.[1,2] No matter at what position the two pendulums are started, they synchronize eventually. Huygens wondered what it was, that mediated this "odd sympathy" as he called it. Huygens reasoned, that tiny vibrations in the supporting structure, where both clocks were hanging, are the link responsible for the observed synchronization, similar to the role of the conductor in the orchestra.

Synchronization of oscillators is a collective phenomenon that can be observed in coupled systems in such different fields as musical acoustics,[3] physics[4,5] or cell biology.[6] In the field of physics, not only synchronization in particular but coupled oscillators in general are a widely researched field. In addition to synchronization also topological phenomena[7] and metamaterials[8] open up large fields of fundamental research as well as new technologies.

Coupled phenomena have been investigated in optical cavities or microwave resonators for many years.[9] In recent years, nanomechanical resonators became more prominent in this field of research. Nanomechanical systems offer the advantage of on-chip integration, together with high sensitivity and frequencies located in the radio-frequency regime, which makes them well-suited for technological applications. Further, the functionality of nanomechanical systems can be increased by coupling to other degrees of freedom to form a hybrid system such as cavity optomechanical systems[10] or spin-mechanical systems.[11]
However, for the exploration of collective nanomechanical phenomena, a sufficiently

strong coupling mechanism needs to be established. Therefore, in most systems coupling is mediated through an external mechanism as in the following examples. So far, strong coupling between nanomechanical resonators for synchronization phenomena relies on external feedback[12] or optomechanical interactions.[13] Topologically protected transport in nanomechanical resonator arrays has only been achieved through parametric coupling[14] or phononic crystal structures.[15]

Intrinsic coupling has been demonstrated in two neighboring strings or beams[16–18] as well as chains or arrays of membranes.[19–21] In those cases, coupling is mediated by strain in a joint clamping point or a different physical link between the resonators.

However, the dense integration of intrinsically coupled nanomechanical resonators into arrays remains a challenge. Here, I present a platform for the investigation of collective dynamics in intrinsically coupled nanomechanical resonator arrays based on nanopillar structures.

Nanopillars are a very versatile platform for various nanomechanical applications. Ultraflexible nanopillars serve as a biosensor through detecting their deflection induced by cellular forces.[22,23] Mechanical nanopillar resonators have been studied intensively over the past years.[24–29] Coupling of the mechanical modes of a single pillar to an external force field has been used to achieve vectorial force field scanning.[27,28] Moreover, mechanical modes of such nanostructures couple to a variety of degrees of freedom, such as a surface acoustic wave[30], a quantum dot[26,31], a spin[32] or a confined electromagnetic mode[29].

However, single nanopillars not only offer the possibility of the integration of a broad range of functionalities, they also allow for the integration into compact arrays.[23,32] To fully exploit the potential of nanomechanical pillars a coupling mechanism between the pillars needs to be established.

In this work, I demonstrate collective dynamics between strain-coupled nanomechanical pillar resonators. The dynamics of single pillars are investigated separately as well as the principles of the underlying intrinsic coupling mechanism in pillar pairs. This knowledge is then brought together in the investigation of the collective dynamics of coupled nanomechanical pillar arrays.

The thesis is structured in a bottom-up approach. To understand the fundamentals of coupled pillar dynamics, one first has to understand the dynamics of a single pillar. In Chapter 2 the single nanopillar as a mechanical resonator is introduced. The mathematical model to describe flexural modes of nanopillars is reproduced and a finite element simulation model complements the theoretical foundation of the single nanopillar dynamics. The survey of single nanopillars goes on with the fabrication of a pillar with a focus on the symmetry of a nanopillar to ensure the homogeneity of eigenmodes when the number of pillars is scaled up. Afterward, the single pillar control and measurement mechanisms are introduced.

The first fabricated single pillars are investigated in the scope of a statistical analysis,

which also gives insight on the homogeneity of nanopillar groups influencing the collective dynamics in later chapters. The frequency can be controlled by a laser-induced frequency tuning mechanism.

In Chapter 3 the number of pillars is doubled. The investigation of the dynamics of only two pillars, allows for the close investigation and characterization of any inter-pillar influence. The theory of two coupled harmonic oscillators is described followed by an expanded finite element simulation tailored to pillar pairs. In the following, strain-induced strong coupling is demonstrated between two nanomechanical pillars by the investigation of hybridized modes and avoided level crossings. Further, the dependence of the coupling strength on the pillar geometry is characterized.

With all the understanding of the single pillar dynamics and the coupling mechanism itself, arrays of 400 nanopillars are investigated in Chapter 4. A theoretical tight-binding model to describe an array of nanopillars is developed in a collaboration by Tirth Shah, Thomas Fösel and Florian Marquardt from the Max-Planck Institute for the Science of Light in Erlangen. Following the theoretical model, experimental techniques specifically suitable for the detection of nanopillar arrays are explained.
Further statistical measurements on different array layouts allow to quantify the frequency homogeneity in a pillar array. Finally, collective dynamics is investigated in nanopillar arrays.

CHAPTER 2

THE NANOMECHANICAL PILLAR RESONATOR

In this chapter, the nanopillar as a nanomechanical resonator is introduced. Particularly, the theoretical description of nanomechanical pillar modes as well as a basic finite element modeling template for the simulation of the vibrations of a single nanopillar are discussed. These fundamentals of the nanopillar dynamics pave the way for an introduction in the nanopillar fabrication as well as actuation and detection schemes for the examination of the nanoresonators. With these techniques, we will then investigate single pillar resonances with a focus on statistical deviations. These basics will set the stage to scale up the number of nanopillars and investigate collective dynamics.

2.1 The nanopillar as a mechanical resonator

In this work, the dynamics of vertically oriented, inversely tapered gallium arsenide (GaAs) nanopillars is investigated. A sketch of such a nanopillar is depicted in Figure 2.1**a**. A nanopillar can be characterized by its foot radius r, its height H and a taper angle φ, which leads to a variable, i.e. non-prismatic cross-section along the nanopillar. The taper angle can also be calculated with the help of the head radius R.

Such a nanopillar can support a number of mechanical modes, such as radial and elongational breathing modes as well as higher order flexural modes. In this work, however, the focus lies solely on fundamental transversal flexural modes. All other modes are typically found at much higher frequencies, which is why there is no interference with these modes. A nanopillar promotes two orthogonal flexural modes,[27,28] one of which is depicted in Figure 2.1**b**.

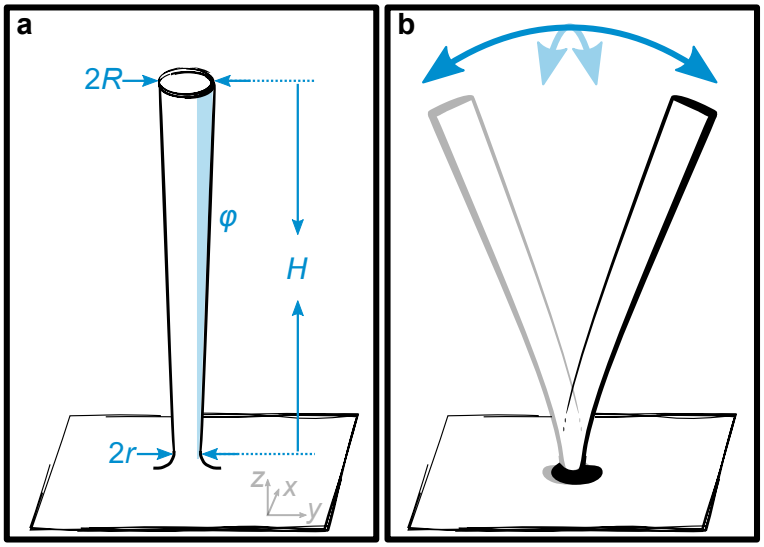

Figure 2.1: **Single nanopillar. a**, Sketch of a single nanopillar, with geometry parameters: foot radius r, height H and taper angle φ, which depends on the head radius R. **b**, Transversal flexural mode, oscillating in the plane of the sketch. The second mode, orthogonal to the first one is only indicated.

2.1.1 Theoretical description

The flexural eigenfrequencies of a singly clamped beam, i.e. a cantilever, which is much longer than wide, is commonly described in the framework of Euler-Bernoulli beam theory.[33] The general Euler-Bernoulli differential equation of a cantilever can be found as[33]

$$E\frac{\mathrm{d}^2}{\mathrm{d}z^2}\left(I(z)\frac{\mathrm{d}^2X(z,t)}{\mathrm{d}z^2}\right) = -\rho S(z)\frac{\mathrm{d}^2X(z,t)}{\mathrm{d}t^2}, \tag{2.1}$$

where $X(z,t)$ describes the deflection of the cantilever at height coordinate z (cf. Figure 2.1**a**) and time t, $I(z)$ the area moment of inertia, $S(z)$ the cross-section along the cantilever, E the Young's modulus and ρ the mass density of the material.

For a general cantilever, the following boundary conditions must apply

$$X(0) = 0, \quad \left.\frac{\mathrm{d}X(z,t)}{\mathrm{d}z}\right|_{z=0} = 0, \quad \left.\frac{\mathrm{d}^2X(z,t)}{\mathrm{d}z^2}\right|_{z=H} = 0, \quad \left.\frac{\mathrm{d}^3X(z,t)}{\mathrm{d}z^3}\right|_{z=H} = 0. \tag{2.2}$$

The first two conditions give a fixed clamping of the cantilever at $z = 0$. The latter two conditions result in zero force, i.e. no bending, and zero torque, i.e. no shearing, at the free end at $z = H$.

Considering in a first approach a simple cantilever with a prismatic cylindrical cross-section $S(z) = S_{\text{cyl}}$ with radius r_{cyl}, height H_{cyl} and area moment of inertia $I(z) = I_{\text{cyl}} = \pi/4 \cdot r_{\text{cyl}}^4$, one can solve the general Euler-Bernoulli differential Equation (2.1). This yields the well-known equation for the flexural fundamental eigenfrequency $f_{0,\text{cyl}}$ of a cylindrical cantilever[33]

$$f_{0,\text{cyl}} = \frac{1}{2\pi} 1.875^2 \sqrt{\frac{E \cdot I_{\text{cyl}}}{\rho S_{\text{cyl}} H_{\text{cyl}}^4}} = \frac{1}{2\pi} 1.758 \sqrt{\frac{E}{\rho}} \frac{r_{\text{cyl}}}{H_{\text{cyl}}^2}. \tag{2.3}$$

However, for the nanopillars sketched in Figure 2.1, the cross-section along the pillar is not prismatic but increases with z as $S(z) = \pi(r + z \tan\varphi)^2$. The area moment of inertia $I(z) = \pi/4 \cdot (r + z \tan\varphi)^4$ varies accordingly. Thus, the simple cantilever solution in Equation (2.3) does not hold for the nanopillars in this work. A new approach described by Paulitschke et al.[24] has shown good agreement with the measured eigenfrequencies of inversely tapered nanopillars.

Paulitschke et al.[24] also consider the general Euler-Bernoulli differential Equation (2.1). The right hand side of this Equation can be interpreted as the differential force acting on the nanopillar at height coordinate z. Under certain conditions, for example when driving the mechanical motion via a piezo, this force can be assumed constant K_x along the nanopillar z-axis. The mathematical expression of this condition is $\tau \ll 1/f_0$. This means the acoustic traveling time along the nanopillar $\tau = H/v$, with velocity of sound v in z-direction, i.e. the time the acoustic wave generated by the piezo needs to travel from the foot of the pillar to its head has to be much smaller than the time the nanopillar needs to swing back and forth, i.e. its oscillation period $1/f_0$. For the GaAs nanopillars in this work this condition is generally fulfilled.

Under this condition Equation (2.1) reduces to

$$E \frac{\mathrm{d}^2}{\mathrm{d}z^2} \left(I(z) \frac{\mathrm{d}^2 X(z,t)}{\mathrm{d}z^2} \right) = K_x. \tag{2.4}$$

This simplified problem with the boundary conditions in Equation (2.2) and a harmonic ansatz $X(z,t) = X_0(z) \cdot \sin(\omega_0 t + \phi)$ can be analytically solved.

The approach finally leads to the fundamental flexural eigenfrequency of an inversely tapered nanopillar[24]

$$f_0 = \frac{1}{2\pi} \sqrt{\frac{E}{\rho}} G(r, H, b) \tag{2.5}$$

with geometry factor

$$
\begin{aligned}
G^2 = \Big(&90b^4r^3\left(bH(b^3H^3 - 2b^2H^2r + 6bHr^2 + 12r^3)\right. \\
&\left.+12r^3(bH + r)(\log(r) - \log(bH + r))\right) / \Big(bH\left(24b^8H^8\right. \\
&- 18b^7H^7r + 72b^6H^6r^2 + 207b^5H^5r^3 - 21b^4H^4r^4 \\
&+ 375b^3H^3r^5 + 1490b^2H^2r^6 + 1410bHr^7 + 420r^8) \\
&+ 60r^3(bH + r)^3(3b^3H^3 - 6b^2H^2r + 12bHr^2 + 7r^3 \\
&\left.+6r^3(\log(r) - \log(bH + r)))(\log(r) - \log(bH + r))\right)\Big).
\end{aligned}
\tag{2.6}
$$

For a circular nanopillar the resonator exhibits two degenerate fundamental flexural modes with frequency f_0. G reduces to $1.765\frac{r}{H^2}$ for $\varphi \to 0$, reproducing Equation (2.3) for the case of a cylindrical nanopillar. Paulitschke et al.[24] show the validity of this theory over a large range of nanopillar geometries.

These flexural modes can now for small driving forces $F_0 e^{i(2\pi f)\cdot t}$ be described as a driven, damped harmonic oscillation of a point mass with effective mass m_{eff}. The effective mass of a inversely tapered nanopillar has been derived in Reference [23]. The frequency dependence of the squared vibration amplitude $|A(f)|^2$ is then found to have a Lorentzian form

$$
|A(f)|^2 = \left| \frac{F_0}{(2\pi)^2 m_{\text{eff}}} \cdot \frac{1}{f_0^2 - f^2 + i\Gamma/(2\pi)\cdot f} \right|^2 \tag{2.7}
$$

with linear damping term Γ accounting for the energy relaxation rate. The full width at half maximum is given by $\Delta f = \Gamma/2\pi$. The dissipation in such a system leads to the definition of the quality factor

$$
Q = 2\pi \frac{\text{energy stored}}{\text{energy dissipated per period}} = \frac{f_0}{\Delta f}. \tag{2.8}
$$

2.1.2 Finite element modeling of a nanopillar

Finite element modeling with *Comsol Multiphysics* is implemented to extend the analytical description and to include more detailed geometrical features of the nanopillars. The simulation model also allows to describe even more complex systems than that of a single nanopillar.

To implement a model of the nanopillar, that resembles the real pillar, we have a look at the micrograph of a nanopillar to extract its geometrical details. Figure 2.2**a** shows a nanopillar micrograph with a close-up of the nanopillar foot. As a result of the fabrication process, the transition of the resonator to the substrate is not a sharp transition, but a rather smooth one. The simulation model incorporates such a smooth transition as

shown in Figure 2.2**b**.

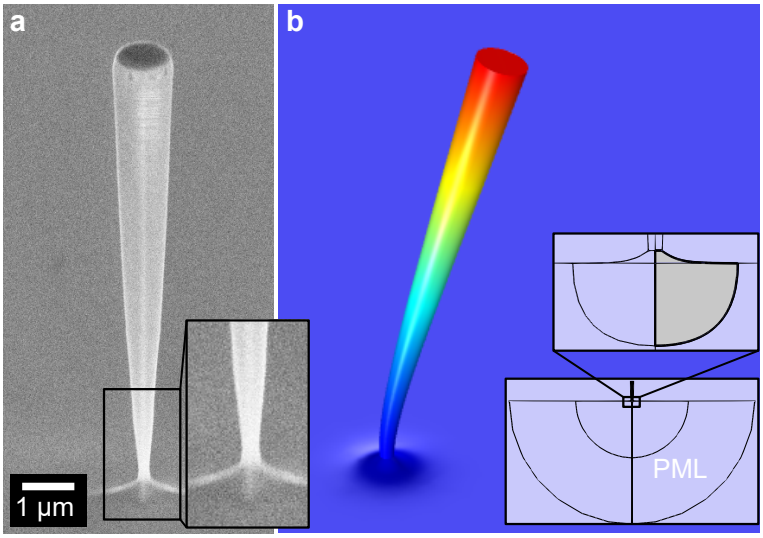

Figure 2.2: **Single pillar simulation model.** **a**, Electron micrograph of a nanopillar with a close up on the foot in a 60° tilted view. **b**, Simulation of a deflected nanopillar, with color coded amplitude. Insets show the 2-dimensional representation of the model including the PML and a close up on the clamping area.

For the implementation of this smooth transition, a *Bézier* curve[34, Chapter 15] draws the outline of the transition region in a 2-dimensional work plane. The curve is then revolved to build a 3-dimensional object, building the transition between the pillar element and the substrate. The Bézier curve allows for the implementation of the height and width of the transition region according to the ones extracted from the micrograph.

The region with the narrowest pillar cross-section at the clamping point experiences most of the bending (cf. Figure 2.2**b**). This, in turn, requires a fine resolved mesh around the clamping point, to ensure a reasonable resolution of that region. However, in the case of a single pillar, the mesh by *Comsol Multiphysics* is automatically refined towards the clamping point as for the narrowing geometry. When considering larger groups of nanopillars this becomes more complex (cf. Chapter 3).

To further adopt the real system in the simulation model a perfectly matched layer (PML) is implemented, which dampens the waves radiating from the pillar into the substrate, to simulate an infinitely large substrate. The size of the PML has to approximately match c/f with the resonance frequency f of the pillar and the velocity of sound c. Thus, a rough frequency estimation is necessary.

In Figure 2.3 the analytical and simulated frequencies are compared. For both, simulation and theory, the pillars have a density $\rho = 5307\,\mathrm{kg\,m^{-2}}$ and Young's modulus $E = 45\,\mathrm{GPa}$.[24,35] This anomalous Young's Modulus for GaAs nanopillars deviates from the one of the bulk material 85.9 GPa, a well known phenomenon for nanometer-sized objects. In the simulation, only the substrate is described with the bulk Young's Modulus. On a further side note, all the nanopillars investigated later in this work inhibit geometry factors in the regime displayed in Figure 2.3.

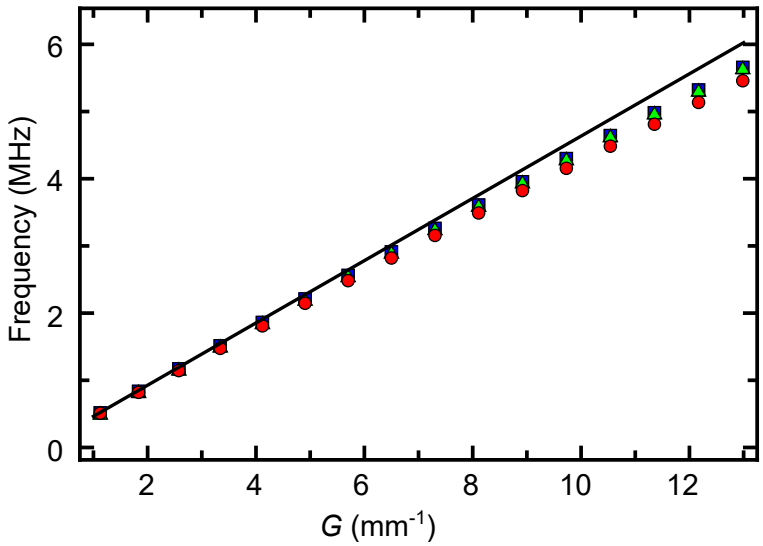

Figure 2.3: **Simulated and calculated frequencies.** Simulated frequencies for different geometry factors G for both clamping conditions with PML (● curved clamping, ■ simple $\sim 90°$ sharp transition) and without PML for a simple $\sim 90°$ sharp transition (▲) as well as the analytical solution of Equation (2.5) (black line).

Figure 2.3 shows a good agreement between theory and simulation data. However, towards larger geometry factors G, which roughly translate to larger aspect ratios $\frac{r}{H}$ for a constant taper angle, the theory yields frequencies up to $10\,\%$ higher than the simulated data within the displayed range. This deviation could be an indication of non-negligible shear forces on the pillar, which are not considered in the Euler-Bernoulli approach but come into play for large aspect ratios $\frac{r}{H}$. While the influence of the PML is very small in the displayed regime, the implementation of the curved clamping further lowers the eigenfrequency very slightly. Albeit the overall agreement between the analytical and simulated models is still rather good, one should be careful when considering nanopillars with large geometry factors. Although the different simulation models do not significantly deviate from another, the model including PML as well as the curved clamping condition makes the most realistic assumptions and are thus used throughout this work.

2.2 Fabrication of a nanopillar

The fabrication of GaAs nanopillars as shown in Figure 2.2**a** is realized in a top-down fabrication process. The basics of the fabrication process have already been established in previous works.[36–38] There, the focus lay on achieving smooth pillar sidewalls, which correlate with low damping due to a usually strong influence of surface defects to the overall damping. In turn, the circularity of the pillar cross-section is now of high priority as it leads to degenerate eigenfrequencies in a pillar, which becomes especially important when considering groups of nanopillars in Chapter 4. In the course of this work, the process is refined with respect to the circularity of the nanopillars' cross-section.

In this section, an optimized fabrication process is described with a focus on the optimized circular cross-section in Section 2.2. However, not all pillars studied in this work were fabricated with this final version of the process but a slightly different one. The fabrication details of all different nanopillar batches as well as additional approaches are discussed in Appendix A.

The process consists of three main fabrication steps as displayed in Figure 2.4 with the result shown in Figure 2.4**d**:

1. pattern definition with electron-beam lithography ensuring high resolution circular pillar heads with good parameter control and reproducibility (Figure 2.4**a**);

2. pattern transfer of the lithographically defined structure onto a silicon dioxide hard mask (Figure 2.4**b**);

3. anisotropic chlorine-based inductively coupled plasma (ICP) reactive ion etch with nitrogen passivation resulting in high aspect ratio structures and smooth pillar sidewalls (Figure 2.4**c**).

Electron-beam lithography. Careful studies of electron-beam lithography[1] for the definition of the 2-dimensional pillar head reveal the best results for a circle for *Poly methyl methacrylate (PMMA) 950k A6* resist on GaAs with 10 µm aperture, 5 kV extra high tension (EHT), 8.6 mm working distance and an area dose of 110 µC cm^{-2}.

[1] *Zeiss CrossBeam 1540XB* with *Elphy Plus* (software version 4.0) and *Neomicra* (software version 2.0.2.9) lithography systems.

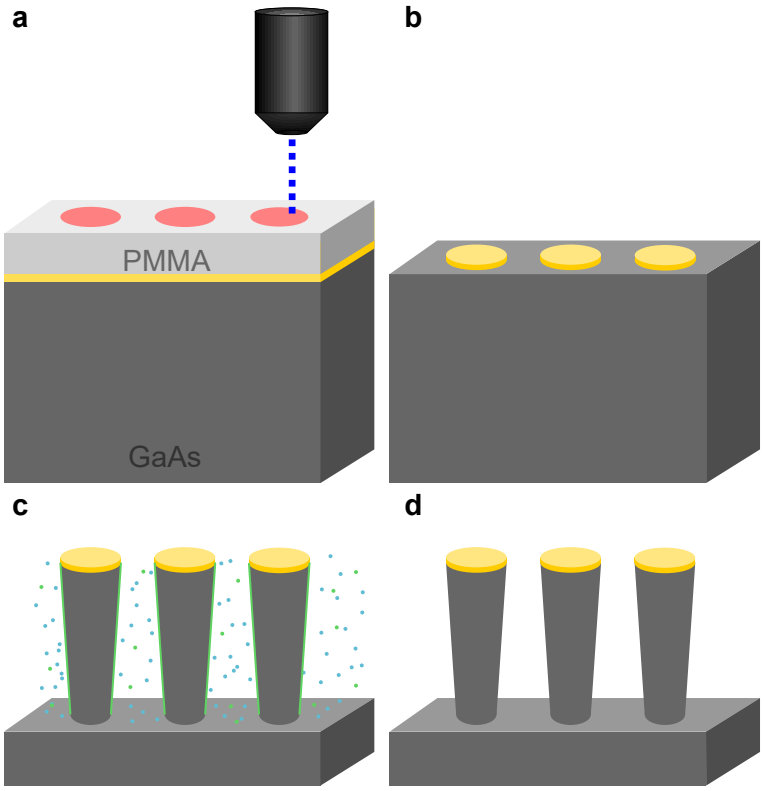

Figure 2.4: **Fabrication scheme.** **a**, Electron beam lithography of circles (red). **b**, Etch mask (yellow) after pattern transfer. **c**, Anisotropic reactive ion etch (plasma in blue) with sidewall passivation (green). **d**, Resulting nanopillars after fabrication.

For a perfect circular shape, the use of *circular mode* in *Elphy Plus* or *Concentric Pattern Generator* in *Neomicra* is crucial. Furthermore, for rendering a circle a point number of around 100 - for a diameter around 1 µm - are usually sufficient. A larger point number mostly increases the buffer time without any notable impact on the results. Finally, development of the resist is done at room temperature for 50 s in one part *Methyl isobutyl ketone (MIBK)* and three parts isopropanol.

Pattern transfer. Once the pattern is lithographically defined, it needs to be transferred to a hard mask. As a hard mask for the following chlorine-based ICP reactive ion etching process 100 nm of either nickel or silicon dioxide (SiO_2) are suitable to protect the pillar structures. Due to easier post-processing and better long-term stability, SiO_2 is chosen as a more practical hard mask (cf. Appendix A.3).

Although a direct lift-off with SiO_2 is a possible approach for the pattern transfer here, the resulting mask shows a rather uneven profile as discussed later in this section. To obtain a well-defined mask, 100 nm SiO_2 are evaporated via electron-beam evaporation on the

bare GaAs substrate before lithography with a 2.0 Å s^{-1} evaporation rate. Subsequently, electron-beam lithography on this two-layer chip is performed as described above. After development 30 nm of chromium are evaporated (evaporation rate: 0.5 Å s^{-1}), which yields a circular chromium etch mask after lift-off. Then an anisotropic ICP reactive ion etch (cf. Table 2.1) based on silicon hexafluoride (SF_6) and argon (Ar) transfers the circular pillar pattern from the chromium mask to a SiO_2 mask. The etch selectively etches SiO_2 with chromium serving as hard mask.

parameter	setting
SF_6 flow	2 sccm
Ar flow	4 sccm
RF power	65 W
ICP power	350 W
pressure	2 mTorr
temperature	10 °C

Table 2.1: **Etch parameters fluorine etch.** Etch parameters for the fluorine-based anisotropic ICP reactive ion etch to reveal the SiO_2 etch mask.[2]

Anisotropic reactive ion etching.

`All etch runs for the samples investigated in this work were performed at the Ludwigs-Maximilians-Universität in Munich (LMU Munich) in collaboration with Philipp Paulitschke and Heribert Lorenz.`

The final step of the fabrication of nanopillar resonators is an anisotropic ICP reactive ion etching process. The etch process is silicon tetrachloride ($SiCl_4$) based with a very small amount of nitrogen added, which in turn favors the formation of a very thin SiO_2 passivation layer on the pillar side walls.[39] The SiO_2 most likely originates from the quartz carrier wafer.

Since this process tends to be unstable, several precautions are met and described in more detail in Appendix A.4. Amongst other things, it is especially important to block the machine from running any other process and it involves long seasoning runs. Due to the instability, the optimal etch parameters are not the same for every batch of samples. Thus, any parameters given here can merely serve as a starting point from which the process can be adjusted. Good etch parameters from a past run are listed in Table 2.2. On a further note a small amount of oil is added between the sample and the carrier wafer of the etch machine to ensure thermal contact.

[2] These parameters have been used at a *Oxford PlasmaLab 100* in the Nanostructure Laboratory at the University of Konstanz.

parameter	setting
$SiCl_4$ flow	13 sccm
N_2 flow	0.1 sccm to 0.2 sccm
RF power	130 W
ICP power	55 W
pressure	2 mTorr
helium flow	5 Torr

Table 2.2: **Etch parameters chlorine etch.** Exemplary etch parameters for the chlorine-based anisotropic ICP reactive ion etch used in *batch 2019* (cf. Appendix A).[3]

An overview of structures resulting from this etch process is given in Figure 2.5.

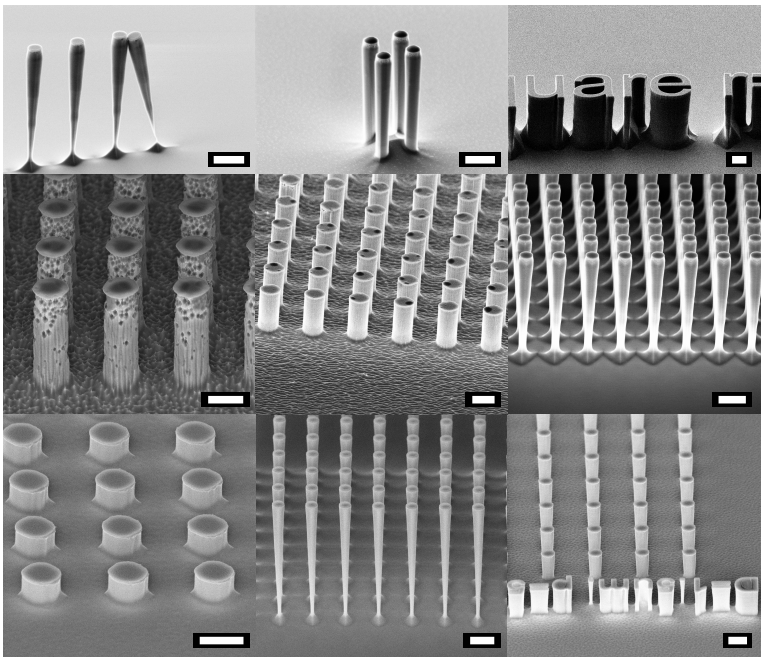

Figure 2.5: **Etch results.** Scanning electron micrograph of different structures fabricated with the anisotropic ICP reactive ion etch. White scale bars indicate 2 µm. The samples are imaged in a 60° tilted view.

The chlorine-based etch discussed here yields good results in terms of sidewall smoothness and is used for all samples throughout the thesis with slightly adapted parameters

[3]These parameters have been used at a *Oxford PlasmaLab 100* at Ludwigs-Maximilians-Universität Munich.

(cf. Appendix A.1.1). However, the tuning in of the process is rather tedious and a hardware change is necessary before running the process. As mentioned above, it requires blocking the equipment for other users and long stabilization runs as well as parameter adjustments (cf. Appendix A.4). Furthermore, the access to the etch equipment at the LMU in Munich requires more planning and provides less flexibility in the sample preparation. Especially, iterative optimization of the fabrication, where the fabricated nanopillars are measured and parameters are adjusted according to these results, is rather slow. Because of that, alternative etch solutions were investigated. A chlorine-based etch on GaAs was employed in the *Nanostructure Laboratory* at the University of Konstanz as well as a fluorine-based etch on a silicon substrate. Both attempts did not yet yield results comparable to the ones shown in Figure 2.5. Nevertheless, these preliminary results can built the foundation for the development of a new etch routine. The two approaches are discussed in Appendix A.5.

Circularity of pillar head. A main issue for later collective measurements is the deviation from the circularity of the pillar cross-section. In Section 2.4, measurements are discussed that pinpoint the necessity of the improvement on the circularity. Here, we show how the anisotropy in the pillar cross-section can be improved down to presumably random fluctuations.

It can be assumed, that the main anisotropy originates in the definition of the etch mask. The etch process can only reproduce features of the etch mask and should not add any anisotropy that is not already present in the etch mask. Thus, the lithography and pattern transfer are the fabrication steps that need to be improved.

In the first fabrication runs a 30 µm aperture and a 10 kV EHT turn out to produce a "knob" at the edge of the lithographically defined circle, as shown in Figure 2.6**b**. Decreasing the aperture and EHT gradually decreases this "knob", till the edges are rather smooth for a 10 µm aperture and 5 kV EHT. Especially the aperture seems to have a large impact on the smoothness of the pattern. Further, the beam speed for the former parameters was at the maximum limit for the desired area dose. This can cause problems for small fluctuations in the beam current and for lowering the dose which can be necessary due to e.g. temperature fluctuations. With the new parameters, the optimum area dose lies far from the limits of the machine, ensuring the stability of the process.

In a second run, the influence of a circular write mode compared to a linear write mode was tested, along with the number of points in the circle and the influence of the software itself. Both, *Elphy* and *Neomicra* software and pattern generators were available and tested.

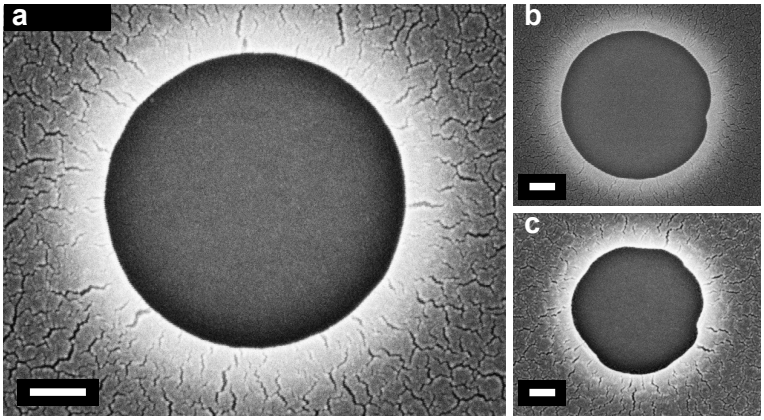

Figure 2.6: **Lithography optimization.** **a**, Final lithography results for the optimized process. **b**, Lithography results for too large aperture resulting in a "knob" on the right side of the circle. **c**, Lithography results for linear write mode with slight underexposure. All images show PMMA resist after development and with a thin layer of sputtered gold on top. Within the circle the resist is removed. White scale bars indicate 200 nm.

Figure 2.6**c** shows the lithography result of the linear write mode with slight underexposure. The shape of the circle disappears very fast below the optimum area dose, whereas with circular write mode (*Concentric Pattern Generator* for *Neomicra*), the result is much more stable with regard to the area dose. In further studies, 100 points at the outline of an approximately 1 µm diameter circle turned out to give good results. *Elphy* and *Neomicra* lithography tools do not seem to have a significant impact on the written circle. An example of the developed PMMA resist for the final process parameters is shown in Figure 2.6**a**.

The ellipticity of the now defined circles is up to $1\,\%$, which is still considerable. However, in fabricating a batch of samples, it became apparent, that this ellipticity seems to be random in a way, that the ellipticity is consistent over a lithography run on a sample, but can even change signs from run to run. Therefore, even compensation in the writing file does not solve the problem. A rather time consuming calibration before each run could solve the problem in the future.

It should be noted, that the determination of the ellipticity also comes with a rather large error, estimated to $\pm 0.5\,\%$, as the absolute deviations are still very small. Nevertheless, an improvement on the ellipticity and especially on the roundness of the pillar has been achieved from roughly $3\,\%$ ellipticity for the first results mostly caused by the "knob" to roughly $1\,\%$.

Although the pattern transfer to a nickel mask has produced comparable results in the

past, the post-processing of this mask comes with some challenges (cf. Appendix A). A SiO_2 mask shows a similar selectivity, however, the pattern transfer via a SiO_2 lift-off is not beneficial. The result of such a lift-off can be seen in Figure 2.7**c** & **d**. In both panels, one can identify several contrast changes in the mask. These contrast changes indicate the boundary between SiO_2 of different morphology or thickness. In Figure 2.7**d** these can be identified: the innermost layer is a rather flat SiO_2 layer with reasonable thickness. The next layer indicates the transition to the substrate, which instead of a sharp transition exhibits a positive taper. The outermost layer seems to be a very thin SiO_2 layer, transcending the originally defined circle. Due to these different regions of SiO_2 thickness, the use of it as an etch mask is not recommended as it can produce steps, when the thin parts are etched away.

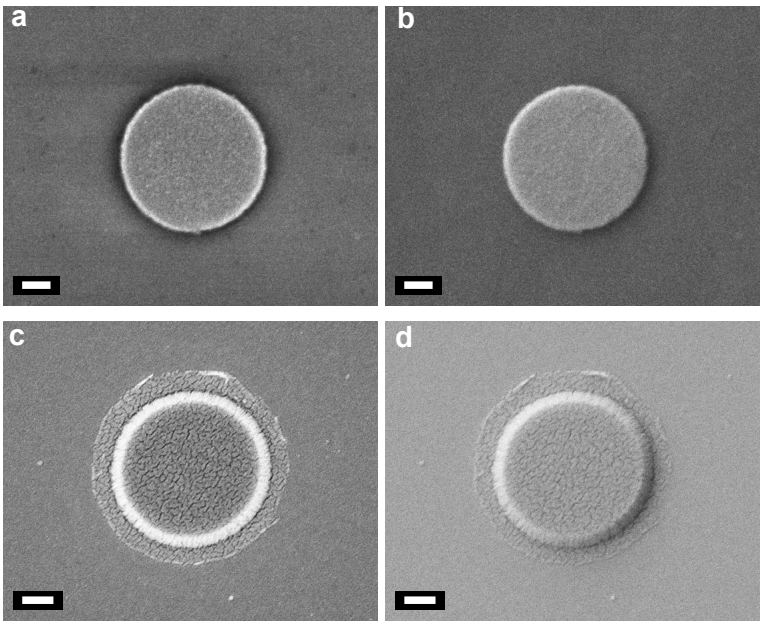

Figure 2.7: **Hard mask optimization. a** & **b**, Scanning electron micrograph of the final SiO_2 mask with chromium on top, taken with in-lens & secondary electron detector, respectively. **c** & **d**, Scanning electron micrograph of a SiO_2 lift-off, taken with in-lens & secondary electron detector, respectively. White scale bars indicate 200 nm.

The solution is provided by a negative process as described in this chapter. A homogeneous SiO_2 layer is evaporated on the bare chip before lithography and resist deposition. Afterwards, the pattern definition and transfer is done as described above. This results in a smooth SiO_2 mask with sharp transitions to the substrate as can be seen in Figure 2.7**a** &**b**, and thus, provides a good etch mask.

2.3 Measurement schemes for a resonant nanopillar vibration

Once fabricated, the dynamics of a nanopillar needs to be characterized. Therefore, a frequency response curve is recorded to determine the pillar's two fundamental flexural resonance frequencies. Additionally, the vibration direction belonging to the respective resonance frequency can be determined. Different measurement schemes, that bare various advantages, are employed according to the respective requirements.

In all response measurements, the pillars are driven via a shear piezo[4]. As the sample is glued onto a shear piezo, to which an AC voltage is applied, this mechanism drives all pillars on a samples at once using their inertia.

All measurements are done at room temperature. Further, depending on the measurement technique, the pillars are under different pressure conditions. Measurements are performed at atmospheric pressure, or vacuum below 10^{-4} mbar.

2.3.1 Laser-based detection scheme

A laser-based detection scheme allows for the measurement of the frequency response curve of a single nanopillar. [26,36,40,41]

A red diode laser with wavelength $\lambda = 635\,\text{nm}$ is focused onto the top part of a single nanopillar. The pillar head acting as a mirror reflects the light, which is then detected with a photo detector and resolved spectrally. The reflected light is modulated by the vibrating pillar and is linearly transduced such that the signal on the photo detector is proportional to the vibration amplitude of the nanopillar.

An estimation of the laser spot size gives a diameter of approximately 2 µm. Therefore, the detected signal originates mainly from a single nanopillar, but can also carry stray signal from objects nearby. In-situ imaging of the laser spot and sample allows for the precise position of the laser on the desired nanopillar. More details on the setup can be found in Appendix B. All laser measurements are conducted in vacuum.

The special advantage of this detection scheme besides its good displacement sensitivity is the straight-forward implementation of a frequency tuning mechanism, which is explained in detail in Section 2.5.

[4] *PI Ceramic GmbH*: PQYY+0769 (measures $(5 \times 5 \times 0.2)\,\text{mm}^3$, CuNi-electrodes, frequency at 4.5 MHz, material PIC255)

2.3.2 Scanning electron microscope imaging

This technique allows for the imaging of the envelope of a driven flexural vibration of a nanopillar with a scanning electron microscope (SEM) as shown in Figure 2.8.

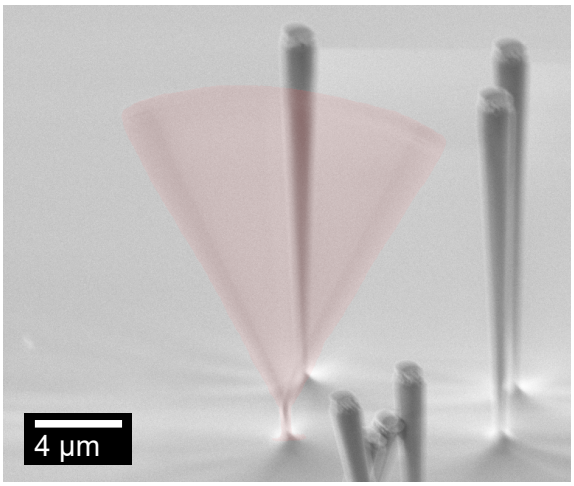

Figure 2.8: **Micrograph of nanopillar vibration.** False color scanning electron micrograph of a vibrating nanopillar with the envelope of the vibrating pillar in red. The sample is imaged in a 60° tilted view.

The sample, mounted on the same shear piezo sample holder, is inserted in the SEM main chamber, by venting the whole chamber. The holder is simply taped to the standard SEM sample holder. The *Zeiss Crossbeam* SEM is equipped with a triaxial cable feed through to the main chamber and before pumping down, the shear piezo is connected to it. The piezo sample holder is grounded via the feed through. Thus, no direct electrical connection between the SEM sample holder and the piezo sample holder is necessary. The sample is then driven with a frequency generator.

When examining a particular nanopillar, the pillar is imaged with line average and a relatively fast scan speed rather than pixel average or a slow scan speed, as justified in the following. Figure 2.9 shows an exemplary SEM measurement on two neighboring nanopillars. A significant increase of the noise can be observed in the image as soon as the driving AC voltage is switched on. This can be seen in the difference between Figure 2.9**a** (without drive) and Figure 2.9**b** (with drive). The AC driving voltage strongly affects the electron beam and thus, the scanned image. A rather small scan speed leads to ripples in the micrograph, thus, a larger scan speed is preferable.

The drive strength, i.e. the peak to peak voltage of the AC signal, is chosen depending on the geometry of a pillar. The expected amplitude for a given drive mainly depends on the flexibility of the pillar. A rather large drive voltage, may result in entering the

nonlinear regime, but can be necessary to detect a resonance in the first place. Additionally, it is strongly recommended, to find the resonance frequency of the investigated pillars before the SEM measurement by some other means, e.g. laser-based detection, to narrow down the frequency sweep range. However, one should note that there frequently appears a deviation in the measured frequencies between the different methods, which can for example be explained by laser induced heating (cf. Section 2.5). Finally, one should choose adequate increments between the applied frequencies in the sweep for the search of a resonance, to make sure the resonance frequency is not missed. With a typical linewidth of a few kHz for resonance frequencies in the MHz regime, a step size of 1 kHz is sufficient to find the resonance frequencies and be time efficient at the same time.

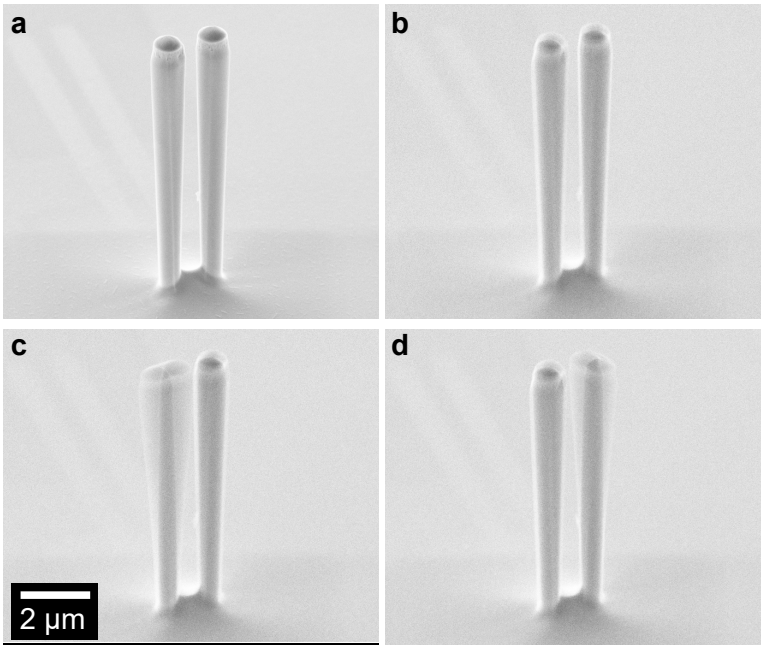

Figure 2.9: **Measurement scheme SEM measurements.** Micrograph of two nanopillars **a** without and **b** with AC voltage applied. **c & d**, micrographs of exemplary nanopillar vibrations of the same two nanopillars. The sample is imaged in a 60° tilted view.

Two examples for a SEM measurement of flexural modes of two nanopillars are shown in Figure 2.9**c** & **d**.

As it might becomes apparent from Figure 2.9**b**, the distortion of the electron beam by the AC voltage can make it appear as though the pillar is vibrating. An especially delicate frequency range is around 1 MHz. Here, the distortion effect is very strong and the pillars seem to move with large amplitudes as well as in circular and elliptical shapes. In order to check for that, a non-vibrating feature on the sample can be imaged

at the relevant frequencies. This feature can appear to vibrate when the electron beam is distorted too much by the applied field. In such a case, these frequencies have to be avoided in the SEM imaging measurements.

A great advantage of this method over the laser-based detection is the possibility to determine the vibration direction of a pillar. This can be seen in Figure 2.10. By imaging the sample from the top one can clearly identify the two orthogonal modes of a pillar and identify their vibration direction with respect to e.g. the sample edge, which follows the $[100]$ crystal direction, or with respect to neighboring pillars, which comes into play in later chapters.

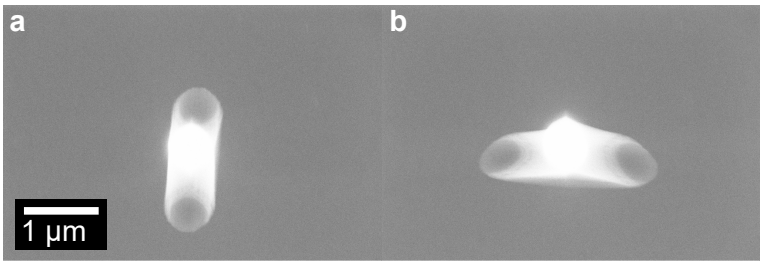

Figure 2.10: **Determination of vibration direction.** Scanning electron micrographs of a nanopillar vibrating in its fundamental modes in **a** vertical and **b** horizontal direction imaged from above.

2.4 Statistic measurements

In this section, statistical resonance frequency measurements of nanopillars are discussed. In previous works,[24,36,42] it was already shown that the theory from Section 2.1.1 can be applied adequately to this type of nanoresonators. The pillars in these works[24,36,42] are fabricated by the same basic fabrication process as the ones investigated in this work.

On this foundation, it is possible to make general resonance frequency predictions for a given nanopillar with given bottom radius r, height H and taper angle φ. However, as known from other nanomechanical resonators, there is a certain amount of frequency disorder for nominally identical nanopillars. In nanofabrication, even small geometrical fluctuations are significant with respect to the general object size, which in turn leads to a rather large influence of small random geometry fluctuations on the properties of nano-objects in general.
On top of this well-known random frequency disorder, however, a systematic frequency disorder can be found, when several nanopillars are grouped together. Furthermore, the two nominally identical orthogonal fundamental frequencies for a circular pillar can split due to fabrication induced anisotropy. Both of these systematic frequency disorder mechanisms will be discussed in the following.

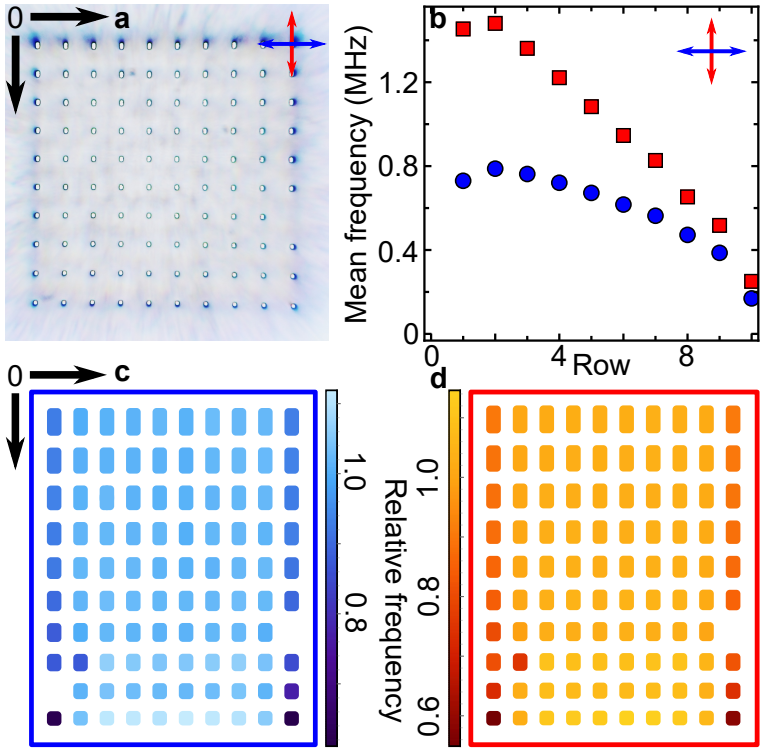

Figure 2.11: **Systematic disorder in nanopillar groups.** **a**, Micrograph of the investigated group of rectangular nanopillars. **b**, Mean measured eigenfrequency of each row of nanopillars in **a**. Geometries within one row are nominally identical. Polarization of the pillar motion is indicated in blue ● (red ■) for horizontal (vertical) vibration as marked in the image. **c & d**, Frequency maps of the array for both polarizations. Horizontal (vertical) vibration is shown in **c** (**d**). The frequencies are normalized to the mean row frequency to disregard of the engineered frequency trend along the array. Missing points are either missing pillars or undetectable frequencies.

To examine the systematic frequency disorder in nanopillar groups, a widely spread group of nanopillars, which is displayed in Figure 2.11, is investigated. The array consists of nanopillars with rectangular cross-section placed in 10 µm distance. Within each row the pillar cross-sections are the same but they vary from row to row. In row 10 all pillars have a square cross-section with extension a in both directions. In row 9 the extension in horizontal (blue) direction remains constant while the one in vertical (red) direction increases to $1.1 \cdot a$ giving a cross-section of $1.1 \cdot a \times a$. In the next row, the cross-section increases to $1.2 \cdot a \times a$. Following that evolution we end up in row 1 with rectangular cross-sections of $1.9 \cdot a \times a$ where the longer extension is along the vertical (red) direction.

First, we have a close look on how the frequency develops following the vertical direction of the array, thus with increasing cross-section. The fluctuation within one row

is omitted for now and the mean row frequency is plotted in Figure 2.11**b**. Neglecting the first and last row, one finds an approximately linear decrease of the resonance frequency for both polarization directions. Although both polarization directions show a dependence of the frequency on the cross-section, the influence on the vertically polarized vibration is significantly stronger, shown in a steeper decrease of the resonance frequency.

However, the mean frequency of the first and last row of the group introduce a discontinuity in the trend of the frequency evolution. The frequencies for the respective rows 1 and 10 lie below the trend.
Figure 2.11**c** & **d** display frequency maps of the whole array, allowing for resolving the frequency dispersion within each row. To omit the frequency evolution with increasing cross-section, every frequency in the maps is normalized to its mean row frequency. From Figure 2.11**c** & **d** it is apparent, that the resonance frequency of the pillars in the first and last column (on the left and right of the maps, respectively) drop significantly below the row average.

These two observations have been confirmed in all investigated groups of pillars. Summarizing, we find, that the frequencies of nanopillars close to the edge of a group drop significantly below the array average. To be more precise, the frequency deviation is larger than random frequency fluctuations. This becomes apparent, when comparing the deviation of the frequencies of the inner pillars (rows and columns two to nine) to the frequencies of the outer pillars (rows and columns one and ten). The standard deviation of the frequency of the inner pillars averaged over all rows and both polarizations is approximately 2.6 % of the respective mean row frequency[5]. Now we consider the deviation of the frequencies of the pillars in the first and last column from their mean row frequency and find 18.1 % deviation, widely spread between 6 % and 40 %, roughly.

This phenomenon has already been observed by P. Paulitschke.[43] In his work, it is explained it by looking at the profile of the underground below the pillars with a confocal microscope. Paulitschke finds an uneven height profile, resulting in the central pillars standing on a pedestal. Assuming a flat substrate before the fabrication, one can conclude, that the etch process in the center of the group is slowed down by the confinement of the plasma between structures, i.e. outer pillars are etched faster, since there is an only half-sided confinement of the plasma. This so called diffusion-limited etch process results in different heights of the nanopillars when they are grouped together: central pillars have shorter heights than outer pillars. According to Equation (2.5), shorter height H with otherwise constant parameters increases the resonance frequency, hence explaining the frequency dispersion in Figure 2.11. Micrographs of the group from Figure 2.11 (Figure 2.12**a**) as well as other exemplary groups (Figure 2.12**b-d**) show that in this work the central pillars of a group are standing on a pedestal, too, similar to the findings from

[5] The standard deviation reduces to 1.3 % if the pillar in row 8, column 2 is regarded as an outlier and omitted.

Paulitschke.[43] Especially noteworthy is that even the rather large distance between the rectangular nanopillars of roughly 10 µm (Figure 2.11 & Figure 2.12**a**) is not enough to suppress this effect. Approaches to overcome this effect are investigated in Chapter 4.

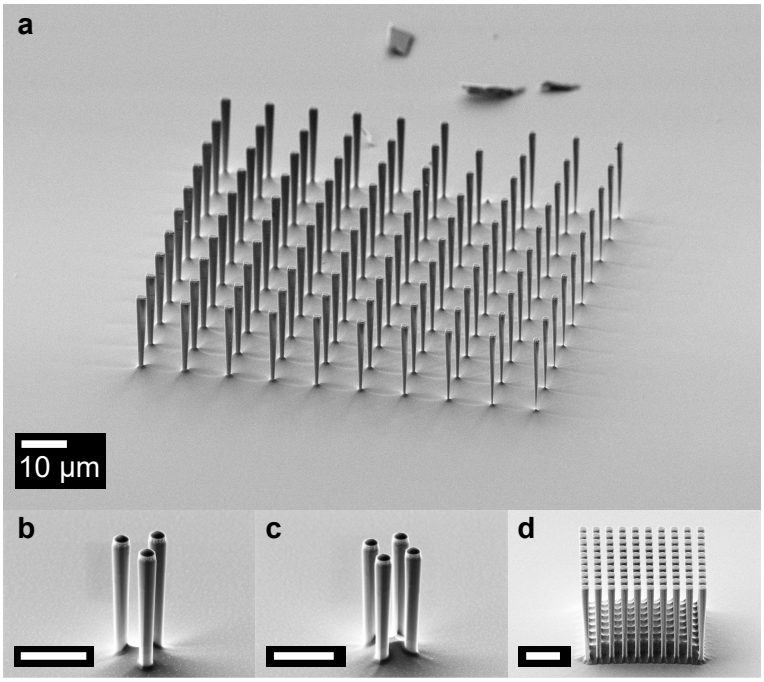

Figure 2.12: **Height profile in nanopillar groups.** **a**, Micrograph of the nanopillar group investigated in Figure 2.11 in a 60° tilted view. **b-d**, Micrographs of exemplary nanopillar groups showing the same height profile as in **a** also in a 60° tilted view. Scale bars in **b-d** indicate a 4 µm length.

The second systematic disorder effect lies in the frequency anisotropy of a single pillar. This originates from fabrication induced deviations from a perfectly round circular shape. A perfectly circular cross-section leads, according to the underlying theory (Section 2.1.1), to two degenerate resonance frequencies. However, non-degenerate frequencies are not necessarily a sign of systematic asymmetry, but could also be explained by the random fabrication induced asymmetry within a pillar. Non-degenerate eigenfrequencies indicate, that the frequency asymmetry of a single pillar is larger than the resonance linewidths. The question, whether we have systematic or random frequency anisotropy will be discussed in the following.

For the investigation of frequency anisotropy, samples fabricated in a previous work[38] are reexamined. We consider a central column of a 40×40 array of circular nanopillars with lattice constant 2.2 µm. 5 rows from the edges of the array are neglected to exclude the effects discussed above. One finds in Figure 2.13**a** two distinct eigenfrequency branches, a higher and a lower frequency branch, which can over all considered pillars

(row 6 to row 35) consistently be assigned to the same vibration direction. That means at all higher frequencies the pillars move in one direction (e.g. x), while at all lower frequencies they move in the orthogonal direction (e.g. y).
While the standard deviation within a mode branch is only around 0.8 %, the mean of the frequency anisotropy is around 4 %. Intra-pillar coupling effects can be neglected, as they are expected to be relatively small.[44] Thus, the statistics suggest a systematic or at least a not fully random anisotropy in $x-$ and $y-$direction, as these deviations are much larger, than the supposedly random fluctuations within one branch. Another indication for a systematic pattern is the fact, that there is no mixing between branches with regards to vibration direction.

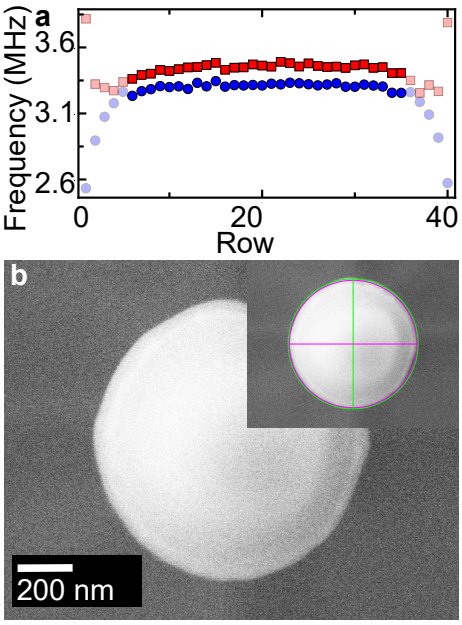

Figure 2.13: **Circularity of pillars. a**, Resonance frequencies for pillars in row 20 of a 40×40 array, separated in higher frequencies (■) and lower frequencies (●). The pillars neglected in the statistical analysis are rendered transparent. **b**, Scanning electron micrograph of a pillar from the sample. Inset shows circles with radii of either horizontal (pink) or vertical (green) pillar extends. The sample is taken from a batch of a previous work.[38]

The cause of this systematic frequency anisotropy lies in a systematic ellipticity of the nanopillars' cross-section. Figure 2.13**b** shows the top view of one of these nanopillars. The deviation of the horizontal and vertical radius is around 1.5 %. This translates for the estimated geometry of this pillar (exact height measurements are not feasible in the center of the array) with Equation (2.5) to a frequency deviation of 3 % to 5 %, which can to a large extent explain the observed anisotropy. The frequency isotropy is a crucial point especially when considering groups of nanopillars as explained in more detail in Chapter 4. Thus, an improvement on the circularity compared to previous works

was necessary. The alterations in the fabrication process implemented in this work is described in Section 2.2.

Now, we neglect systematic frequency disorder and frequency anisotropy in the two examples from this section to find the random frequency disorder. This means we only consider the inner pillars of the rectangular 10×10 array and we only look at separate branches of the measurement on the 40×40 circular pillar array. One finds a very rough frequency disorder around $1\,\%$ which coincides with experiences in the group from other nanomechanical devices. For both, Chapter 3 and Chapter 4 the frequency homogeneity plays an important role as a foundation for the observation of coupling effects.

Section 2.2 describes the improvement of the systematic anisotropy of the pillar head down to $1\,\%$. For the parameters of the 40×40 circular pillar array this would reduce the frequency anisotropy to $2\,\%$ – $3.5\,\%$ but varies for different pillar parameters. However, it should be noted, that there is still some seemingly randomly occurring separation of the frequency branches. This anisotropy is consistent over a whole sample, but varies from sample to sample even changing sign.

2.5 Frequency control

The following section is partly based on the publication J. Doster, S. Hoenl, H. Lorenz, P. Paulitschke, E. M. Weig, Dynamics of strain-coupled nanomechanical pillar resonators, *Nature Communications*, 10(1):5246, 2019. Reference [45].

The frequency disorder between two or more nominally identical pillars (see Section 2.4) induced by random geometrical fluctuations can be detrimental for the investigation of nanopillar groups as will become apparent in Chapter 3. For that reason, a frequency tuning mechanism is established, that allows the reversible or even irreversible control of the resonance frequency of one single nanopillar even after fabrication.

Considering Equation (2.5), there are several parameters contributing to the resonance frequency:

- geometrical factors r, H and φ,
- material parameters E and ρ.

To tune the frequency of a ready-built nanopillar one has to address one or more of these parameters. Post-fabrication geometry tuning to customize the resonance frequency has been shown before for GaAs.[46] However, here, a different approach is employed by

targeting the material parameters, more specifically the Young's modulus E. While the approach by Gil-Santos et al.[46] is irreversible, the tuning mechanism presented here has the advantage to be reversible, at least within a certain range.

We make use of the circumstance, that the Young's modulus of GaAs is temperature dependent. The warmer the pillar is, the less bending rigidity it has. In a cubic system, the $[100]$ Young's modulus $E_{[100]}(T)$ can be calculated with the elastic constants $C_{11}(T)$ and $C_{12}(T)$[47]

$$E_{[100]}(T) = \frac{(C_{11}(T) + 2C_{12}(T))\,(C_{11}(T) - C_{12}(T))}{C_{11}(T) + C_{12}(T)} \tag{2.9}$$

$$\underset{[47]}{\approx} \frac{7.45 \times 10^{14} - 1.77 \times 10^{11} T + 1.05 \times 10^{7} T^2}{8475.96 - T}\,\mathrm{Pa}, \tag{2.10}$$

for temperatures T in the range $0\,\mathrm{K} < T < 1513\,\mathrm{K}$.

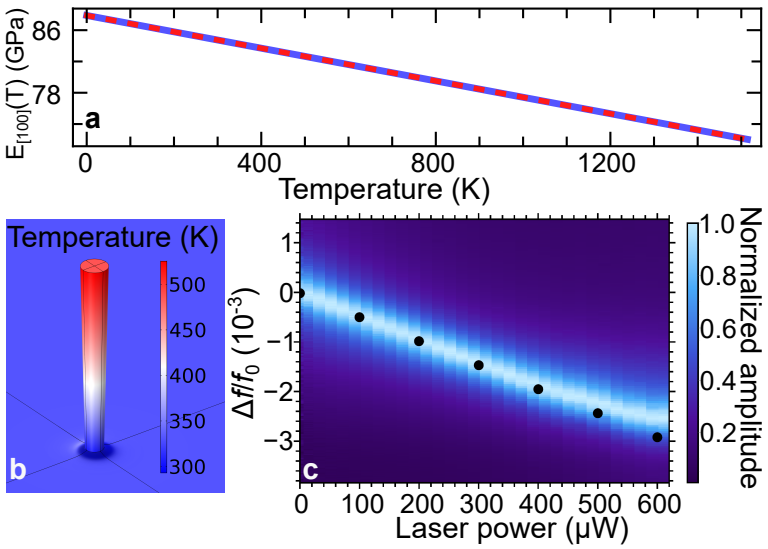

Figure 2.14: **Frequency tuning mechanism.** **a**, Temperature dependence of the $[100]$ Young's modulus $E_{[100]}(T)$ of GaAs. Comparison of literature[47] (blue) and linear approximation from Equation (2.10) (red, dashed). **b**, Temperature profile along a nanopillar with $r = 291\,\mathrm{nm}$, $H = 6.1\,\mu\mathrm{m}$ and $\varphi = 1.38°$ hit with 700 µW laser power, simulated by finite element method (cf. Section 2.1.2). **c**, Measured frequency response of the nanopillar from **b** for different laser powers (color map) overlaid with simulated frequency tuning of the same pillar (black circles). Parts **b** & **c** of the figure are reproduced from Reference [45].

Figure 2.14**a** depicts the Young's modulus $E_{[100]}(T)$ in the specified temperature range.

From that, one can find a decrease of the Young's modulus with increasing temperature, which can be approximated by a linear dependence

$$E_{[100]}(T) \approx E_{[100]}(300\,\mathrm{K})(1 + \alpha(T - 300\,\mathrm{K})) \tag{2.11}$$

$$\approx 84.74\,\mathrm{GPa}(1 + 1.23 \times 10^{-4}\,\mathrm{K}^{-1}(T - 300\,\mathrm{K})). \tag{2.12}$$

Equation (2.12) reproduces the trend of Equation (2.10) perfectly in the specified range (cf. Figure 2.14**a** (red, dashed)).

As the resonance frequency of a nanopillar depends on the square-root of the Young's modulus, heating up a nanopillar decreases its resonance frequency.

However, often it is required, to tune the frequency of only a single pillar while the frequency of surrounding pillars remain constant. Thus, heating the hole sample, and therefore tuning all pillars equally, is often not helpful. Hence, a scheme to only heat up a single pillar is required. This scheme is ready provided by the laser-based detection scheme (see Section 2.3.1). When the 635 nm wavelength laser is perfectly focused on a single pillar's head[6], 65 % [48] of the red light is reflected by the GaAs surface and collected by a photo detector, as described in Section 2.3.1. However, the remaining 35 % of laser light is absorbed by the nanopillar, which is then transformed into heat, softening the nanopillar and decreasing its eigenfrequency. The general mechanism is similar to the thermal tuning of an optical transition in quantum dots or cavities. [49–51]

Under these assumptions, finite element simulations allow the determination of the temperature profile and resulting frequency shift for a nanopillar hit with 700 µW of a perfectly focused 635 nm laser. There, the previously used constant Young's modulus in the material parameters of the model is replaced by Equation (2.12). The resulting simulated temperature distribution of the a nanopillar is displayed in Figure 2.14**b**. One finds, that under these conditions the nanopillar temperature can be locally increased by a few hundred degrees. The increase depends on the laser power as well as on the nanopillar geometry.

With this foundation set, we now investigate the effect of the laser-induced heating on the resonance of a nanopillar. Figure 2.14**c** shows both, the measured and simulated laser-induced frequency tuning. The frequency response is measured as described in Section 2.3.1, while the laser power is continuously increased via a neutral density filter. In Figure 2.14**c** the measured frequency response (color map) shows a continuous lowering of the resonance frequency of the nanopillar with increasing laser power. The simulated

[6] Here, only GaAs at the pillar head is considered, which serves as an approximation. Usually there is a small layer of the mask's material left, however the thickness of this layer far below the light's wavelength and thus, its impact should be negligible here.

frequency tuning (black dots) is overlaid on the measurement and it follows the measurement over a long range. This shows, that laser-induced frequency tuning allows for the continuous frequency control within a range of roughly 0.3 % of the resonance frequency.

However, at rather high laser powers, towards the right side of the graph in Figure 2.14**c** the measurement deviates from the simulation. This is a sign of permanent damage, which can be induced by a laser at high laser powers heating the nanopillars so much, that local melting occurs.[36] The permanent damaging of a nanopillar allows for a controlled irreversible frequency increase within a small range, if the pillar is irradiated at moderate powers over a long time.

CHAPTER 3

PAIRS OF COUPLED NANOMECHANICAL PILLAR RESONATORS

The following chapter is mostly based on the publication
J. Doster, S. Hoenl, H. Lorenz, P. Paulitschke, E. M. Weig, Dynamics of strain-coupled nanomechanical pillar resonators, *Nature Communications*, 10(1):5246, 2019. Reference [45].

With the understanding of the dynamics of a single nanopillar, the dynamics of two pillars are investigated in the following chapter. As shown in previous works,[16–18] strain in the clamping point can lead to coupled modes. The underlying theory and extended simulation model lay the foundation for the demonstration of coupling between two nanopillars and a comprehensive study of the coupling strength for different pillar pairs.

3.1 Coupled harmonic oscillators

First, the theory underlying two coupled nanopillars and its manifestation in measurements are described.

The dynamics of a nanomechanical pillar can be considered as a driven damped harmonic oscillation with an effective mass m_{eff} (cf. Section 2.1.1). To simplify even further damping and driving are neglected for now, leaving a plain harmonic oscillator as a model system for a nanomechanical pillar. If we now consider two coupled nanomechanical pillar resonators we therefore use two coupled harmonic oscillators as a

theoretical model for the system. A more thorough description of the theoretical background on coupled harmonic oscillators is given by L. Novotny.[52]

A simple system of two harmonic oscillators is depicted in Figure 3.1. The two independent systems are labeled 1 and 2, with effective masses m_i and spring constants k_i where $i = \{1, 2\}$, leading to the uncoupled eigenfrequencies $\omega_{i,0} = \sqrt{\frac{k_i}{m_i}}$. The two harmonic oscillators are coupled via a spring with spring constant κ, which then determines the coupling strength. The coupled system can then be described by the equations of motion

$$\begin{aligned} m_1\ddot{x}_1 + k_1 x_1 + \kappa(x_1 - x_2) &= 0 \\ m_2\ddot{x}_2 + k_2 x_2 + \kappa(x_2 - x_1) &= 0 \end{aligned} \tag{3.1}$$

where x_i is the displacement of each oscillator $i = \{1, 2\}$ from their resting position.

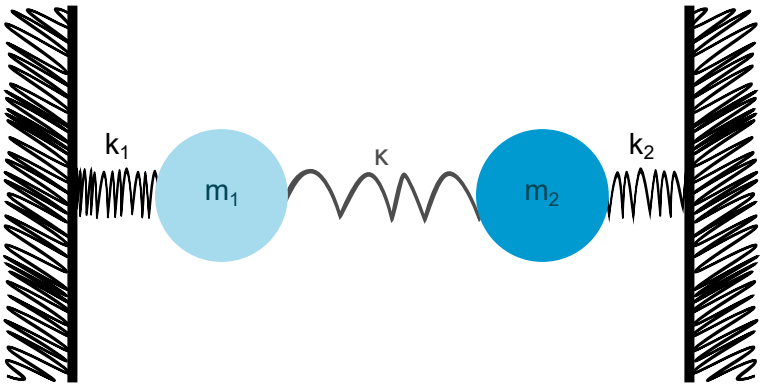

Figure 3.1: **Two coupled harmonic oscillators.** Schematics of two harmonic oscillators with masses m_1 & m_2 and spring constants k_1 & k_2, respectively. The two oscillators are coupled via a spring κ.

This system of coupled differential equations has two non-zero eigenfrequency solutions

$$\omega_\pm^2 = \frac{\omega_1^2 + \omega_2^2}{2} \pm \sqrt{\frac{(\omega_1^2 - \omega_2^2)^2 + 4g^2\omega_1\omega_2}{4}} \tag{3.2}$$

with

$$\omega_i = \sqrt{\frac{k_i + \kappa}{m_i}}, \quad i = \{1, 2\} \tag{3.3}$$

and coupling rate

$$g = \frac{\kappa}{\sqrt{m_1 m_2 k_1 k_2}}. \tag{3.4}$$

With $g \propto \kappa$, the coupling rate is a measure of the coupling strength in units of a frequency as an alternative to κ measuring the coupling strength in units of a spring stiffness.

In the case of two identical systems $m_1 = m_2 = m$ and $k_1 = k_2 = k$, the presence of a coupling κ leads to a splitting of the two originally identical frequencies $\omega_{1,0} = \omega_{2,0} = \omega_0$ to

$$\begin{aligned} \omega_+ &= \sqrt{\frac{k + 2\kappa}{m}} \\ \omega_- &= \sqrt{\frac{k}{m}} \end{aligned} \tag{3.5}$$

where a larger coupling induces a larger splitting.

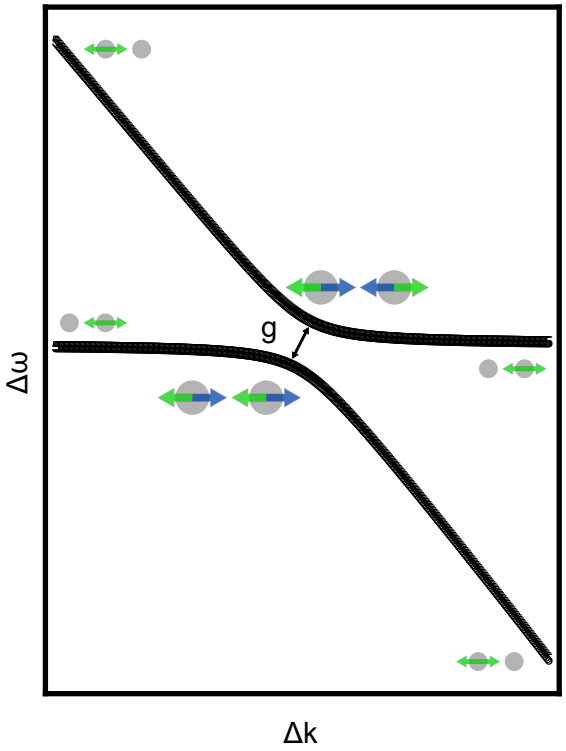

Figure 3.2: **Avoided level crossing.** Schematic avoided level crossing, when one spring constant is changed by a sweeping parameter Δk. The two branches don't intersect in the coupled case. The respective mode shapes are depicted at their places on each branch, the two oscillators are indicated as gray circles. Colors of the arrows indicate the phase relation between the two oscillators in the avoided crossing. Far from the avoided crossing only one oscillator vibrates, so that no specific phase relation appears.

Now, we approach this limit of identical oscillators gradually with masses $m_1 = m_2 = m$ and a gradually tuned spring constant $k_1 = k_2 + \Delta k$, which is swept across an interval around k_2 while k_2 is constant. The eigenfrequencies $\omega_\pm$ behave accordingly. Figure 3.2 shows the behavior of this system. In the uncoupled case $\kappa = 0$, the two frequency branches would cross, at the point of $\Delta k = 0$. However, in the coupled case, the frequencies are split (cf. Equation (3.5)) by the coupling rate g.
In the center of the avoided level crossing, the coupling leads to the formation of hybridized modes, an antisymmetric higher energy mode and a symmetric lower energy mode (cf. insets in Figure 3.2). For the case of the two coupled pillars the former corresponds to an anti-phase, the latter to an in-phase vibration of the two pillars. Far from the avoided crossing no coupled modes are visible, but the two masses oscillate individually on their respective branch.

So far, the description does not include damping. However, damping has to be taken into account to describe a real system of nanomechanical pillars. Equation (3.1) can be extended by a damping term with damping constants Γ_i to

$$\begin{aligned} m_1\ddot{x}_1 + m_1\Gamma_1\dot{x}_1 + k_1x_1 + \kappa(x_1 - x_2) &= 0 \\ m_2\ddot{x}_2 + m_2\Gamma_2\dot{x}_2 + k_2x_2 + \kappa(x_2 - x_1) &= 0. \end{aligned} \tag{3.6}$$

The analytical solution contains an imaginary frequency part, which reflects the damping of the respective modes. Qualitatively, the mode branches in Figure 3.2 will be broadened, so the squared amplitude is the usual Lorentzian (cf. Equation (2.8)) instead of being infinitesimally sharp. If the coupling rate g which separates both branches is much larger, than the smear out of the branches, the dynamics of the system appears to be as described before. In the opposite limit, where g is much smaller than the width of the modes, the avoided level crossing won't be visible anymore. Thus,

$$g > \frac{\Gamma_1 + \Gamma_2}{2} = \frac{\Delta\omega_+ + \Delta\omega_-}{2} \tag{3.7}$$

defines an important threshold and marks the transition to the strong coupling regime.

To measure an avoided level crossing the frequencies of one or both oscillators have to be swept towards each other and beyond.

3.2 Finite element modeling of pillar pairs

Now, the model of two coupled harmonic oscillators is transferred to a nanomechanical pillar pair system. The underlying mechanism for coupling as well as mode identification and an estimation of the coupling strength are investigated in finite element simulations

of two identical nanopillars.

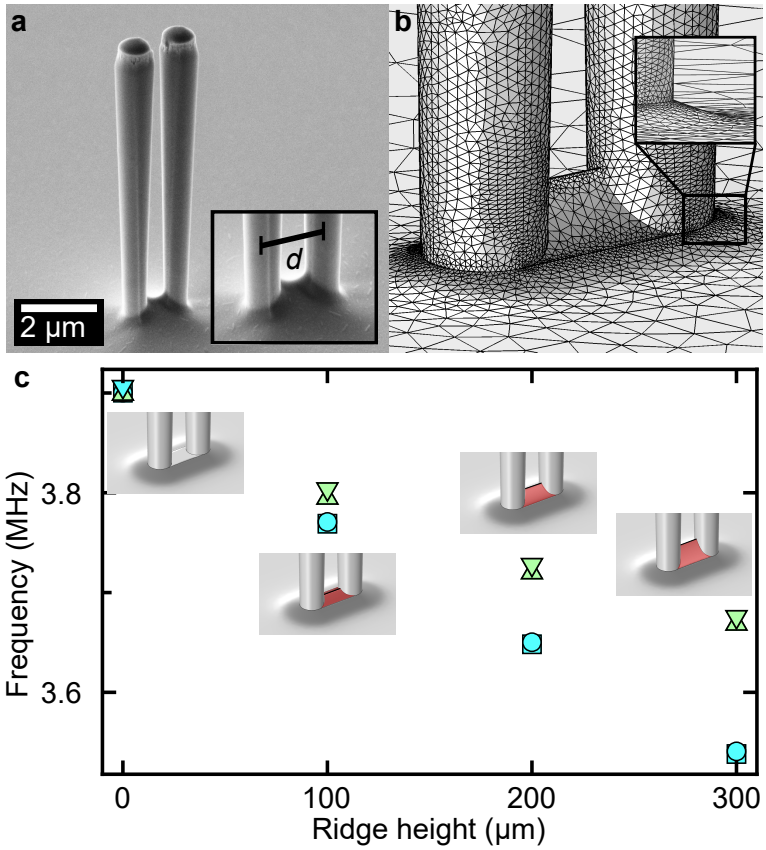

Figure 3.3: **Pillar pair simulation model.** **a**, Electron micrograph of a nanopillar pair with center-to-center distance d. Inset shows a zoom on the nanopillar clamping point with ridge between the two pillars. **b**, Zoom on the clamping point of the simulation model, where the ridge is incorporated additionally to the Bézier clamping introduced in Section 2.1.2. **c**, Resonance frequencies of the pillars depending on the ridge height. Insets show a close up on the clamping points for the respective model with the ridge colored in red. Different colors and symbols show different mode branches split in two higher frequency modes (△, ▽) and two lower frequency modes (○, □). Parts **a** & **b** are taken from Reference [45].

Building on the model introduced in Section 2.1.2, two identical neighboring pillars with center-to-center distance d are simulated. Additionally, there is an extension to the simple model of two single pillars as introduced in Section 2.1.2 to match the geometry of a real nanopillar pair displayed in Figure 3.3**a**. Due to the diffusion limited etch process (cf. Section 2.2), which inhibits a slow etch rate in confined spaces, there is a ridge between the two pillars at the height of their clamping points as shown in the inset of

Figure 3.3**a**. The extended pillar pair simulation model includes a ridge between the pillars as in Figure 3.3**b** additionally to the Bézier curve transition at the clamping point from Section 2.1.2. An automatic mesh leads to a very coarse mesh at the ridge, which, however, plays an important role in strain-coupling and needs to be refined manually to ensure sufficient resolution of the simulation model.

The dimension of the ridge is assimilated to the real pillar pair. However, to investigate the influence of the ride in general a parametric sweep of the ridge height is performed. The effect of the ridge height on the resonance frequencies of the pillars is shown in Figure 3.3**c**. We find four fundamental eigenfrequencies per pair. While these four eigenfrequencies should all be degenerate in the case of an uncoupled system without a ridge, the inclusion of the ride adds an asymmetric feature to the system and splits the modes into two higher frequency modes (Figure 3.3**c**, green) and two lower frequency modes (Figure 3.3**c**, cyan). The evolution of the ridge height shows how this splitting into two main branches increases from basically zero for a flat ridge to $\gtrsim$ 100 kHz for 300 nm ridge height. The two higher modes are called in-plane modes, the lower modes out-of-plane modes. The specified plane refers to the plane defined along the ridge and along the pillar height – the modes vibrate along (in-plane) or orthogonal (out-of-plane) to it. The ridge between the pillars introduces an additional stiffness, which is especially strong when the pillars vibrate in the direction of the ridge. This stiffening leads to an increase of the in-plane frequencies.

Comparing this influence of the ridge on the pillars' resonance frequencies to observations in measurements, one finds a slightly larger asymmetry in real pillar pairs in the range of 500 kHz. For the measured pillar pairs, all fabricated in *batch 2017*, however, not only the ridge contributes to the asymmetry but also the shape of the nanopillar head (cf. Appendix A.1.1). Nonetheless, the ridge height for all pillar pair simulations is set to 300 nm as this approximately matches the measured height and puts the asymmetry in a reasonable range. Even though the ridge for real nanopillar pairs varies slightly with their distance, all simulations are done with the same ridge height as a suitable approximation.

With this model, the coupling between two neighboring pillars can be simulated. Figure 3.4**a** shows the strain field induced by the pillar vibrations, which extends even into the substrate. One finds that the strain fields of the two neighboring pillars overlap, which enables energy transfer between vibrational modes of the two pillars via strain-induced coupling. Figure 3.4**a** shows the in-plane antisymmetric mode of a pillar pair.

To further quantify the coupling strength via an avoided level crossing, a tuning mechanism is implemented in the simulation model. To mimic the laser-induced tuning in Section 2.5, the Young's modulus of one of the nanopillars is set to $E + \Delta E$, with ΔE as a sweep parameter (cf. Figure 3.4**b**). The resulting avoided level crossings are shown in Figure 3.4**c**. It shows an avoided level crossing between the two in-plane modes and

a separate one between the two out-of-plane modes, respectively.

The two higher frequency mode branches correspond to in-plane motions, where the antisymmetric mode is found as the higher energy mode as predicted in the theoretical model Section 3.1. The lower frequency mode branches correspond to out-of-plane motions with the higher energy mode manifesting as antisymmetric mode, accordingly.

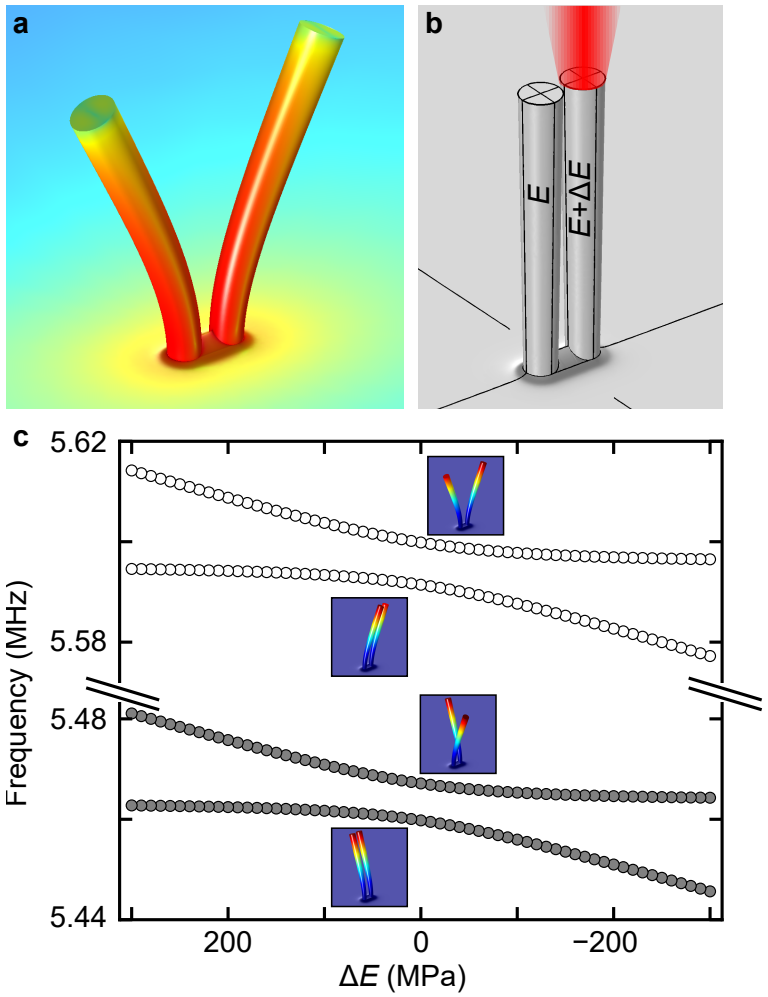

Figure 3.4: **Coupling simulation.** **a**, Strain distribution of a nanopillar pair vibrating in the antisymmetric mode. Red (light blue) corresponds to high (low) strain. **b**, Simulation model with tuning parameter ΔE and laser beam. **c**, Simulated avoided crossings between in-plane (○) and out-of-plane (●) vibrations of the pillar pair, respectively. Insets show the corresponding hybridized modes in the center of the avoided crossing. The color scheme of the insets shows the displacement for illustrative reasons. Images are taken from Reference [45] and part **c** is slightly altered.

For the extraction of the coupling strength, the simulated avoided level crossing can be fitted with the theoretical model from Section 3.1. This will be used in the following sections for the comparison of simulated and measured coupling strengths.

3.3 Strain-induced coupling between pairs of nanomechanical pillar resonators

With the theoretical background laid out, strain-induced coupling in nanomechanical pillar pairs is demonstrated via the identification of hybridized modes and the measurement of avoided level crossings. The strength of the coupling is quantified by fitting the theoretical model deduced in Section 3.1 to the measured avoided level crossings. The coupling strength dependence on the distance d of the two pillars as well as their height H and radius r is investigated via measurements and finite element simulations.

3.3.1 Mode hybridization

A nanopillar pair with pillar foot radius $r \approx 310\,\text{nm}$, pillar height $H \approx 7\,\mu\text{m}$ and center-to-center distance $d \approx 1\,\mu\text{m}$ shown in Figure 3.5**a** is investigated in SEM measurements where the envelopes of the eigenmodes are imaged (cf. Section 2.3.2).

As predicted from the theoretical model, four fundamental flexural modes can be identified in Figure 3.5 – two for the left `L` and two for the right pillar `R`. Despite an orientation angle of the pair which is tilted with respect to the $[110]$ crystal direction, which follows the lower edge of the top view SEM images, the vibration is along or orthogonal to the $[110]$ direction. The labels horizontal `H` for the $[110]$ and vertical `V` for the $[1\bar{1}0]$ crystal direction refer to the vibration directions in the top view SEM images.

The four fundamental modes are spectrally well separated from each other, which becomes apparent by comparing the frequency insets in Figure 3.5**b-e**, keeping in mind that pillar resonances usually have a linewidth of a few kHz. A very large separation between the horizontal and the vertical modes is caused by the asymmetry induced by the ridge in between the two nanopillars as shown in finite element simulations in Section 3.2. The somewhat smaller separation between the two horizontal modes and the two vertical modes, respectively, can be addressed to fabrication imperfections.

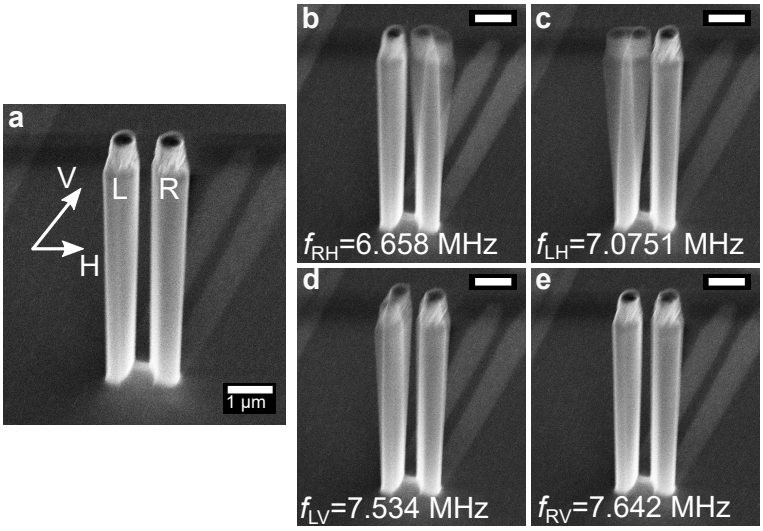

Figure 3.5: **Identification of eigenmodes. a** Electron micrograph of nanopillar pair with $r \approx 310\,\text{nm}$, $H \approx 7\,\mu\text{m}$, $d \approx 1\,\mu\text{m}$. The two pillars are labeled right `R` and left `L`, the two eigenmodes horizontal `H` and vertical `V`, according to their direction of motion. **b**-**e**, Electron micrographs of the four eigenmodes of the pillar pair from **a** with their respective eigenfrequencies $f_{\mathtt{XY}}$ (`X`$\in${`L`,`R`}, `Y`$\in${`H`,`V`}). All scale bars indicate 1 µm. Images are taken from Reference [45].

Now, one of the four modes, $f_{\mathtt{LV}}$ depicted in Figure 3.5**d** is examined more closely by sweeping the drive frequency in small steps across the resonance (sketch in Figure 3.6). The frequency sweep is performed in a small range around the `LV` resonance, far from the other resonances.

Figure 3.6 shows the evolution of the envelope of the pillar pair vibration from a top (upper) and a 60° tilted view (lower). When sweeping the drive frequency in a small window across the eigenfrequency of $f_{\mathtt{LV}} = 7.534\,\text{MHz}$, the amplitude of the left pillar shows the expected response curve for a harmonic oscillator with a peak at the eigenfrequency. Since, the resonance is assorted to the left pillar, this behavior is entirely expected according to the amplitude evolution in a driven damped harmonic oscillator.

However, the right pillar also starts vibrating at a rather small amplitude even though the frequencies under investigation are far from its eigenmodes. The amplitudes of the two pillars evolve simultaneously with increasing frequency. A more extensive sweep is shown in the Movies M1 & M2[1]. There the simultaneous amplitude evolution becomes even clearer and thus, confirms the above observations. Hence, the measurements show a hybridized mode between two neighboring pillars mediated by coupling.

[1]Movies are taken from the supplementary material of Reference [45] (see attached USB stick).

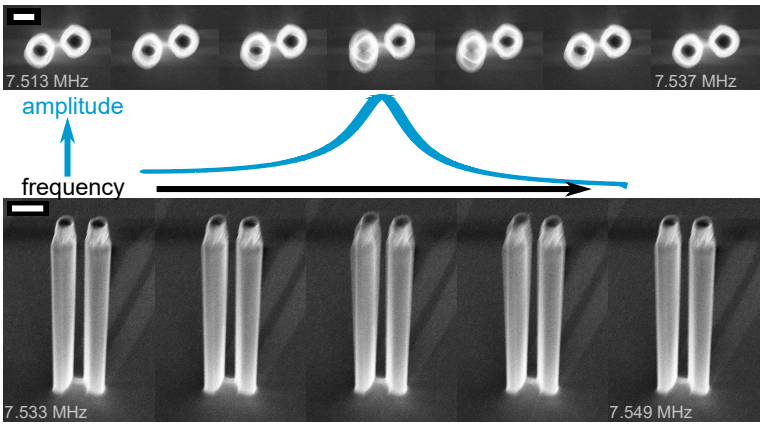

Figure 3.6: **Hybridized mode imaging.** Scanning electron micrograph of the driven pillar pair from Figure 3.5 with frequency increasing from left to right across the exemplary linear response curve as shown in the sketch. The images are taken at equally distributed frequency steps of 4 kHz. The pair is shown in a top view (upper row, scale bar $\widehat{=}$ 500 nm)) and a 60° tilted view (lower row, scale bar $\widehat{=}$ 1 µm)[2].

On a side note, the resonance frequencies in Figure 3.6 are slightly different between the tilted and the top view measurements. This is due to rather strong electron beam-induced deposition during the top view measurements, which are done after the tilted view measurements. Electron beam-induced deposition (EBID) deposits material on the sample and thus, adds mass to the nanopillar which in turn shifts the resonance towards lower frequencies according to $f \propto \sqrt{1/m_{\text{eff}}}$. Additionally, the resonance is not only shifted to lower frequencies but also it appears slightly broadened.

To further confirm the hypothesis of the observation of a hybridized mode and to not rely only on visual confirmation, a routine to extract the amplitude of each nanopillar is developed. For this purpose, only the top view images are taken, since there the amplitude can be read out more easily. Figure 3.7 shows the routine for two exemplary images. The original images are shown in Figure 3.7**a**. Both images are taken with a drive applied to the sample to account for the blurring out of all shapes which should not be mistaken for a resonant vibration as explained in Figure 3.7. The upper image taken off-resonance serves as a reference.

In the next step, shown in Figure 3.7**b** a threshold is set to binarize the image, in order to separate the pillars from their background. Note that for imaging reasons the two pillars melt into one shape in the binarized image. This connection however appears in a horizontal image plane only between the pillars, while the pillar motion of interest in this case is in the vertical image plane. The image is cut in two, in order to separate the

[2] A drift of the SEM stage has been compensated using the *StackReg* tool for *ImageJ* or *python*.

melted shape into two pillars.

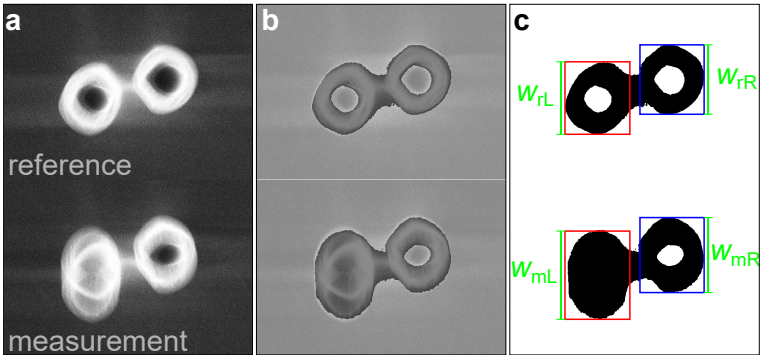

Figure 3.7: **Amplitude extraction method.** **a**, Electron micrograph of the driven pillar pair from Figure 3.5 far from resonance $f_{\mathtt{LV}}$ (`reference`) and on resonance $f_{\mathtt{LV}}$ (`measurement`). **b**, Binarization of the two images from **a**. **c**, Bounding rectangles on the two pillar shapes and vertical length of it $w_{\mathrm{r}i}$ for the reference and $w_{\mathrm{m}i}$ for the measurement for the left and right pillar $i \in \{\mathtt{L},\mathtt{R}\}$, respectively. For illustrative reasons, bounding rectangles in horizontal directions are fit to visual estimations carrying no information about the pillar and the vibration.

A bounding rectangle is fit to the two pillar shapes then, where the vertical parameter $w_{\mathrm{r}i}$ for the reference and $w_{\mathrm{m}i}$ for the measurement ($i \in \{\mathtt{L},\mathtt{R}\}$) are extracted. The difference between measurement and reference $w_{\mathrm{m}i} - w_{\mathrm{r}i}$ is here approximated as the peak-to-peak amplitude. Comparatively small deviations in height during deflection of the pillar are not taken into account here, which is a good approximation if the amplitude is much smaller than the height of the pillar (cf. Appendix B.2), which is valid here.

This amplitude evolution with the drive frequency f_{drive} is shown in Figure 3.8. The simultaneous evolution of the amplitudes of the two pillars is apparent and supports the hypothesis of the formation of a hybridized mode. However, it is obvious from both, Figure 3.6 and Figure 3.8, that the amplitudes of the two pillars are not the same, as they should be for a fully hybridized mode.

This can again be explained by fabrication imperfections. For perfectly identical nanopillars we would observe a fully hybridized mode. However, the nanopillars in the investigated pair are not perfectly identical. Thus, the mode in Figure 3.6 is not fully hybridized but only partially because the two uncoupled modes are not degenerate (cf. Figure 3.5). This means, we only observe the beginning of a mode hybridization.

A tuning mechanism would allow to shift the non-degenerate frequencies closer together to observe a fully hybridized mode. However, the tuning mechanism introduced in

Section 2.5 is not fit to be implemented in the SEM. That way, we can still observe the beginning of a mode hybridization mediated by coupling.

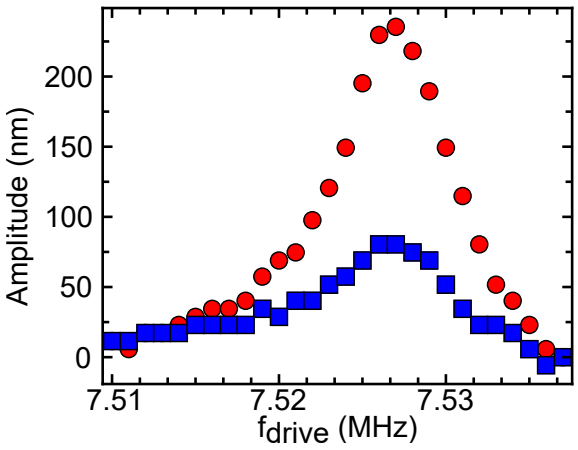

Figure 3.8: **Hybridized mode amplitude evolution.** Extracted peak-to-peak amplitude of the left (red, ●) and right (blue, ■) pillar from the pair in Figure 3.5. Negative values are due to small uncertainties in the amplitude values. The image is taken from Reference [45].

On a further note, it is not possible to determine if the observed hybridized mode is a symmetric or an antisymmetric one without phase resolution. Although judging from the frequency order the lower frequency should be the symmetric mode (cf. Section 3.1). However, this would need to be confirmed and is not within the scope of this thesis.

3.3.2 Avoided level crossing

The demonstration of mode hybridization in the previous chapter is evidence of coupling between two neighboring nanomechanical pillars. With this proof of concept, the next step is the determination of the coupling strength for particular pillar pairs. As laid out in the theory in Section 3.1, the most direct way to do this is by measuring an avoided level crossing between the two coupled modes and to determine the coupling strength via a fit of the model to the data.

As described in Section 3.2, the fundamental modes of two neighboring pillars appear in two pairs, each pair showing a separate avoided level crossing. The following measurements focus solely on the investigation of the two higher frequency modes. In simulations (Section 3.2) they are assigned to an in-plane motion. However, as seen before, real pillars of a pair vibrate along the main crystal directions, disregarding of the orientation of their symmetry axis on the substrate. The two directions are, thus, referred to as horizontal and vertical rather than in-plane and out-of-plane. SEM measurements show,

that the higher frequency modes of real pillar pairs vibrate in the previously defined vertical axis as shown in the insets of Figure 3.9**b**.

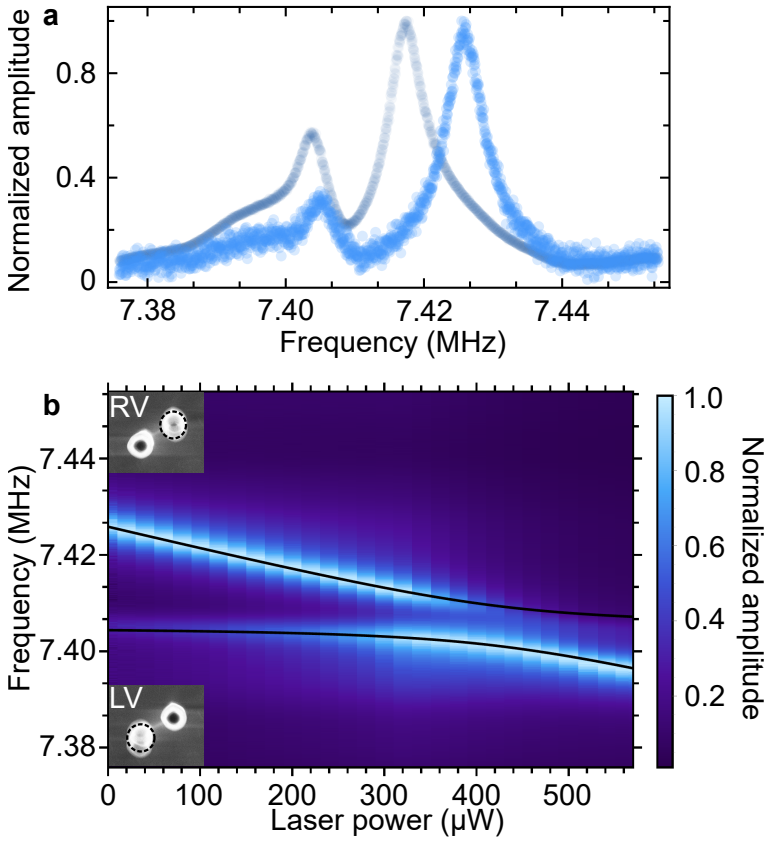

Figure 3.9: **Avoided level crossing for pair with $\mathbf{r} \approx 310\,\mathrm{nm}$, $\mathbf{H} \approx 7\,\mu\mathrm{m}$, and $\mathbf{d} \approx 1.3\,\mu\mathrm{m}$. a**, Frequency response measurement of the right pillar of the pair for almost zero laser power (●) and 200 µW laser power (●). **b**, Laser-induced tuning reveals an avoided level crossing which is fitted with the theory from Section 3.1 (black line). The fit yields the coupling rate $g/2\pi = (8.3 \pm 1.8)\,\mathrm{kHz} > \Delta f \approx 3.5\,\mathrm{kHz}$, with the linewidth Δf. Insets show the respective electron micrographs of the two modes when driven far from the avoided crossing at the respective frequencies f_{LV} (lower inset) and f_{RV} (upper inset). The smallest possible laser power is referenced to zero, as it is small compared to the whole range of used laser power. Part **b** of the image is taken from Reference [45].

These two modes are now detected in the laser-based detection scheme (cf. Section 2.3.1) for a pillar pair with $r \approx 310\,\mathrm{nm}$, $H \approx 7\,\mu\mathrm{m}$, and $d \approx 1.3\,\mu\mathrm{m}$. The laser spot is focused onto the nanopillar with the higher resonance frequency, in this case the right pillar. Since the laser spot is rather small, the reflected signal shows mainly the

vibration of this one pillar. However, stray light allows for the simultaneous detection of the second pillar's vibration albeit with a much smaller signal amplitude.

Exemplary frequency responses for a rather small laser power as well as a significantly higher laser power is shown in Figure 3.9**a**. Because of the laser induced heating, the increased laser power leads to a shift of the resonance frequency for the higher frequency mode, which belongs to the irradiated pillar. The second pillar, which resonates at the lower frequency mode, is only hit by stray light and thus, shows a slight frequency shift, which is, however, negligible.

When we consider two coupled pillar modes of neighboring pillars with no tuning applied, the modes are split by two mechanisms. The coupling rate g as shown in Figure 3.2 as well as fabrication imperfections. Thus, with no tuning applied, we start out at the very left of the avoided level crossing shown in Figure 3.9**b**. With increasing laser power, the higher frequency is slowly tuned towards the lower frequency. The two modes show an avoided level crossing as depicted in Figure 3.9. A fit of the model to the data yields the coupling rate $g/2\pi = (8.3 \pm 1.8)$ kHz. The linewidths average around $\Delta f \approx 3.5$ kHz, which puts the coupling of these two modes in the strong coupling regime $g/2\pi > \Delta f$. Thus, strong coupling between these two particular resonators is demonstrated.

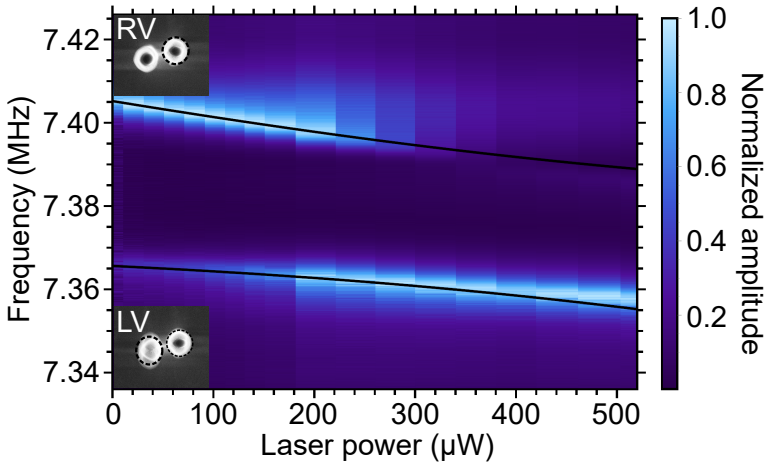

Figure 3.10: **Avoided level crossing for pair with $\mathbf{r} \approx 310$ nm, $\mathbf{H} \approx 7$ µm, $\mathbf{d} \approx 1$ µm.** Frequency response measurement of the right pillar of the pair. Laser-induced tuning reveals and avoided level crossing which is fitted with the theory form Section 3.1 (black line). The fit yields the coupling rate $g/2\pi = (33.3 \pm 3.0)$ kHz. Insets show the respective electron micrographs of the two modes when driven far from the avoided crossing at the respective frequencies f_{LV} (lower inset) and f_{LV} (upper inset). The image is taken from Reference [45].

Moreover, the amplitude evolution in the avoided level crossing is additional confirmation for the evidence of strong coupling. Since mainly, the right pillar is detected, the transition of the strong signal amplitude from the upper to the lower branch indicates mode hybridization at the point of the avoided level crossing at 425 µW and 7.401 MHz followed by a transition of the right pillar resonance from the upper to the lower branch.

To find the coupling rate of the pair which showed evidence of the mode hybridization in Section 3.3.1, the same pair with $r \approx 310\,\text{nm}$, $H \approx 7\,\mu\text{m}$ and $d \approx 1\,\mu\text{m}$, is now investigated under laser tuning. The resulting avoided crossing is shown in Figure 3.10. Insets of the respective modes are at the leftmost edge of the avoided crossing, where the mode hybridization measurements are taken, since laser-induced tuning is not possible in the SEM. In principle, however, the modes should be fully hybridized in the center of the avoided crossing. The fit yields a coupling rate of $g/2\pi = (33.3 \pm 3.0)\,\text{kHz}$ exceeding the coupling rate of the first pair in Figure 3.9.

Thus, strong intrinsic coupling between neighboring pillar pairs has been demonstrated. It also became apparent, that the coupling strength can vary from pair to pair. The most pronounced difference between the two investigated pairs is the distance d between the two pillars. This indicates that the distance between the pillars affects the coupling strength. This will be further examined in the following chapter.

3.3.3 Geometry dependence of the coupling strength

The results in the previous chapter indicate, that there is a dependence of the coupling strength on the geometry parameters of the pillar pair. Assuming strain-induced coupling, the coupling strength should depend on the strength of the created strain field, which in turn depends on the geometry of each pillar, but also on the separation of the pillars, since the strain field decreases with distance from its origin as Figure 3.4 indicates.

Finite element simulations with different parameters allow to pinpoint this dependence of the strain-induced intrinsic coupling on the relevant parameters. The simulation results are displayed in Figure 3.11. They show the dependence of the coupling on the most influential parameters, the center-to-center distance d (**a**), the bottom radius r (**b**) and the height H (**c**).

The simulation results show a clear decrease of the coupling strength with larger pillar distance d. This is a typical signature of strain-induced coupling as the strain field decays with distance.[53] Furthermore, the coupling strength increases with larger foot radius r and smaller height H.

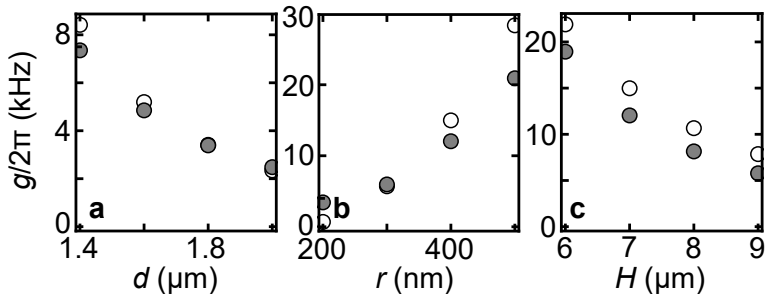

Figure 3.11: **Simulated geometry dependence of the coupling.** Simulated coupling rate $g/2\pi$ for in-plane (○) and out-of-plane (●) modes depending on **a** the center-to-center distance d, **b** the bottom radius r and **c** the height H. The taper angle is constant throughout all simulations. Images are taken from Reference [45].

It becomes additionally apparent, that the in-plane and out-of-plane coupling strengths are very similar. Comparative simulations in Appendix C.1 show, that this is an effect induced by the ridge between the pillars. Thus, the ridge seems to homogenize the coupling strength of the different modes.

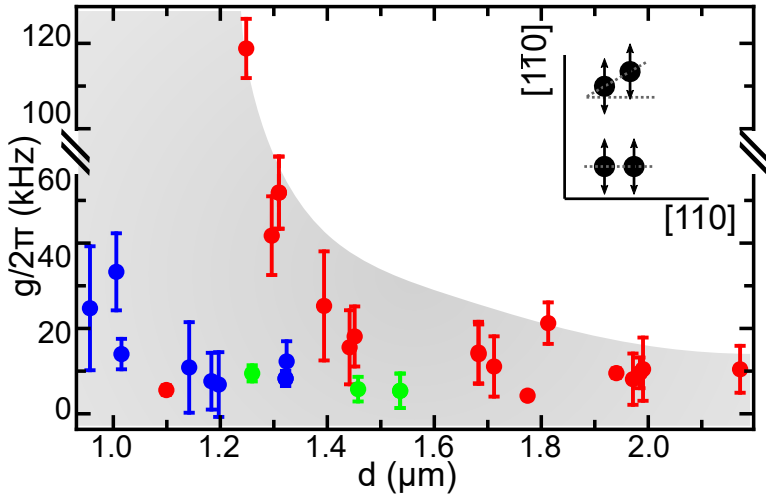

Figure 3.12: **Experimental geometry dependence of the coupling.** Measured coupling strength $g/2\pi$ of vertical modes depending on the center-to-center distance d for different geometries. Colors indicate different pillar pair geometries with $r = 430\,\text{nm}$ & $H = 7\,\mu\text{m}$ (●), $r = 335\,\text{nm}$ & $H = 7\,\mu\text{m}$ (●), $r = 330\,\text{nm}$ & $H = 8.2\,\mu\text{m}$ (●) and with varying orientation on the substrate as shown in the inset. Error margins indicate the tolerance of the fitted coupling rate. The gray area serves as a guide to the eye for the decay of coupling rates with larger pillar distance. The image is taken from Reference [45].

Figure 3.12 shows the experimentally determined dependence of the coupling rate on the pillar pair geometry. All avoided crossings for these data points can be found in Appendix C.2.

A clear drop of the coupling rate $g/2\pi$ with increasing pillar distance can be seen for each of the three data sets. Thus, the intrinsic coupling is most likely mediated by strain through the joint clamping point.

Further, the increase of the coupling rate with larger bottom radius r, as suggested in the simulations, can be seen in Figure 3.12. The height dependence of the coupling rate as seen in the simulations, however, can not clearly be confirmed due to the rather large error bars.

Angle dependence. With the influence of the three most important geometry parameters clarified, this section will deal with a fourth one, separately.

The zinc blende structure of the gallium arsenide substrate, induces an anisotropic Young's modulus. The theoretical direction dependence of the Young's modulus [47,54] for a (100) GaAs wafer is displayed in Figure 3.13**a**. As the coupling is mediated by strain, the stiffness of the substrate between the pillars presumably influences the coupling rate. In other words, the orientation of the pillar pair on the substrate with respect to the crystal directions (cf. inset in Figure 3.12) should influence the coupling strength.

First, the variation of the coupling strength with orientation angle is determined in finite element simulations. To that end, the Young's modulus of the isotropic substrate is set to the value calculated for the respective angle. The simulation results in Figure 3.13**b** indicate, that the coupling rate $g/2\pi$ varies with the orientation angle, showing a behavior opposite to the Young's modulus in Figure 3.13**a**. Hence, a smaller Young's modulus along the two pillars' connecting line prompts a stronger intrinsic coupling between these two pillars in the simulation model.

To investigate the angular coupling dependence in measurements, the experimentally determined coupling rates shown in Figure 3.12 are resolved by the angular orientation of their position on the substrate (cf. sketch in Figure 3.13**c**). This is shown in Figure 3.13**c**, where the angular orientation is depicted with different symbols.

However, opposite to the predictions, the data in Figure 3.13**c** does not reveal any clear correlation between the coupling strength $g/2\pi$ and the orientation angle of the pillar pair on the substrate.

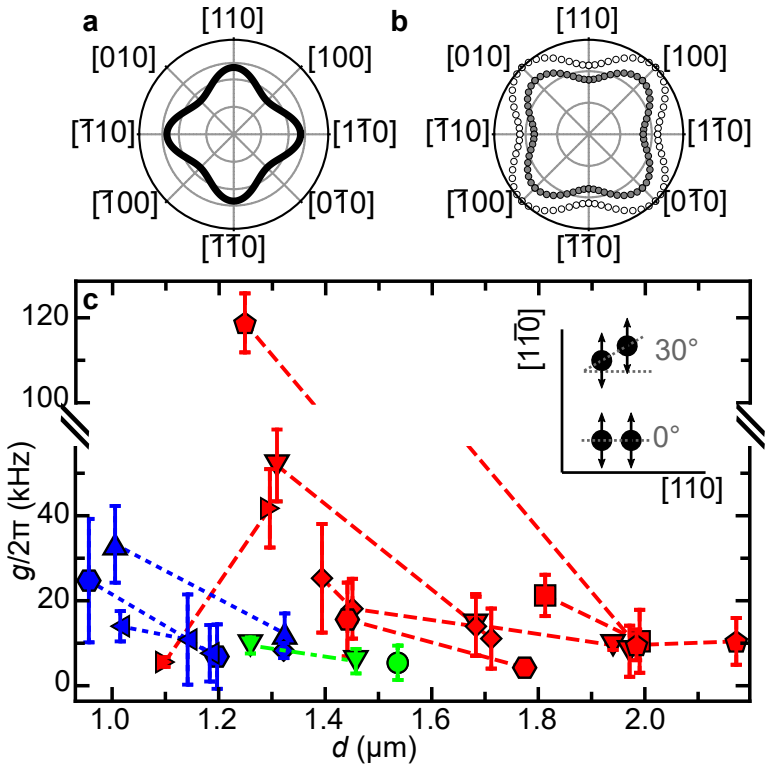

Figure 3.13: **Angle dependence of the coupling.** **a**, Angular dependence of the Young's Modulus on a (100) GaAs wafer calculated from.[47,54] **b**, Simulated angular dependence of the coupling rate $g/2\pi$ for in-plane (○) and out-of-plane (●) modes. The simulation model incorporates an isotropic substrate with a Young's modulus corresponding to the simulated orientation angle. **c**, Experimentally determined coupling strength $g/2\pi$ from Figure 3.12 ($r = 430\,\text{nm}$ & $H = 7\,\mu\text{m}$ (●), $r = 335\,\text{nm}$ & $H = 7\,\mu\text{m}$ (●), $r = 330\,\text{nm}$ & $H = 8.2\,\mu\text{m}$ (●)) with different symbols indicating the orientation of the pillar pair with respect to the [110] crystal direction, 0° (●), 10° (■), 15° (▲), 20° (▼), 25° (⬟), 30° (◆), 35° (⬣), 40° (▶) and 45° (◀). Images are taken from Reference [45].

Thus, the correlation found in the simulation can not be validated. This is probably due to the large scatter and large error bars in the experimental data. Furthermore, the vibration direction for all measured pillar pairs differs from the simulated ones: instead of in-plane and out-of-plane vibrations, the pillars move along the horizontal and vertical direction regardless of their orientation on the substrate. This is probably caused by the large geometrical asymmetry in the nanopillars from *batch2017* (cf. Appendix A.1.1).

CHAPTER 4

ARRAYS OF COUPLED NANOMECHANICAL PILLAR RESONATORS

In the previous chapters, I introduced the nanopillar as mechanical resonator and demonstrated intrinsic strain-induced coupling between two nanopillars and measures to control that coupling. Now, the collective dynamics of two dimensional nanopillar arrays are studied. As before, the theoretical background is laid out first, followed by new detection techniques suited for the examination of nanopillar groups. The chapter is completed with statistical measurements in arrays and finally measurements of collective dynamics effects in nanopillar arrays.

4.1 Tight-binding model

This model has been developed in collaboration with Tirth Shah, Thomas Fösel and Florian Marquardt from the Max-Planck Institute for the Science of Light in Erlangen and is printed under their permission.

In this section, a theoretical tight-binding model is introduced to describe an array of coupled nanomechanical pillars. We first consider a case without disorder in the array, which means that all single pillar eigenmodes in one direction are identical, while there can still be a difference between the two orthogonal eigenmodes.

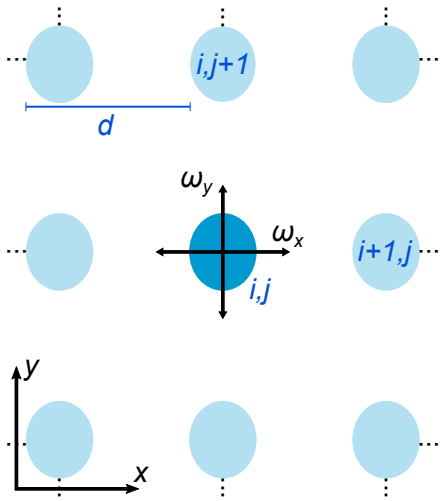

Figure 4.1: **Pillar array schematics.** Schematics of a pillar array. For site i, j located in row i and column j the frequencies of the displacement of the center of the pillar in the orthogonal directions x and y are ω_x and ω_y and the angle $\alpha = 0$. All pillars are identically elliptical (with major axis in y-direction in this example).

The pillars are arranged in a square $N \times N$ lattice with lattice constant d. The displacement of the center of the pillar at site i, j $(i, j = 1, ..., N)$ located in row i and column j from its neutral position $|\psi^{i,j}(t)\rangle$ can be written as

$$|\psi^{i,j}(t)\rangle = \begin{pmatrix} x^{ij}(t) \\ y^{ij}(t) \end{pmatrix} = \begin{pmatrix} x^{i,j}_{\text{zpf}}(b(t)^{i,j}_x + b(t)^{i,j\dagger}_x) \\ y^{i,j}_{\text{zpf}}(b(t)^{i,j}_y + b(t)^{i,j\dagger}_y) \end{pmatrix} \tag{4.1}$$

where $x^{i,j}_{\text{zpf}} = \sqrt{\hbar/(2m\omega_x)}$ and $y^{i,j}_{\text{zpf}} = \sqrt{\hbar/(2m\omega_y)}$ with effective mass m and frequencies ω_x and ω_y[1]. We assume that every individual pillar is slightly elliptical with its major axis oriented along either x or y direction which is defined as $\alpha = 0$. [2] This means that the two principal modes of a pillar are oriented along these directions as well with the corresponding frequencies ω_x and ω_y. At the same time however, we assume that all pillars in the array are identical ellipses since disorder is neglected for now. The ellipticity is exemplary indicated in Figure 4.1.

[1] For clarity, the explicit mention of the time dependence is omitted from now on, e.g. $b(t)^{i,j}_x = b^{i,j}_x$.
[2] For $\alpha \neq 0$ the major axis of the pillars is oriented along a direction different from x or y, which will not be discussed here.

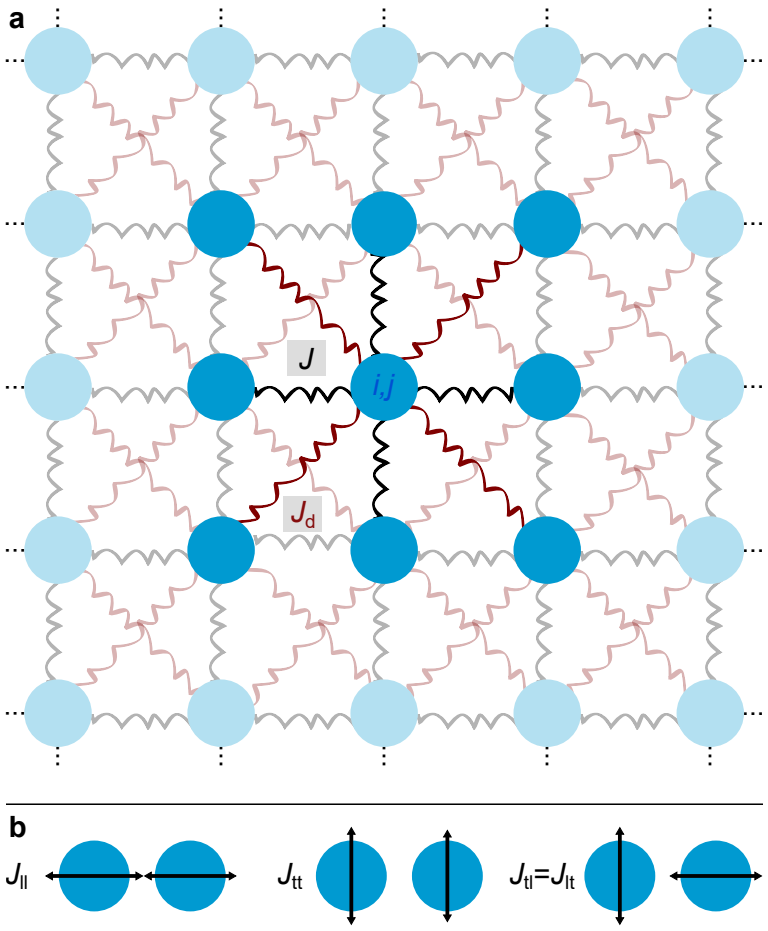

Figure 4.2: **Coupled pillar array schematics. a**, Scheme of an array of coupled pillars with all considered coupling springs drawn. The central pillar and all its direct neighbors and involved couplings are highlighted. Couplings to nearest neighbors J (black) and next nearest neighbors J_d (red) are considered. **b**, Different configurations of coupling for relative transversal or longitudinal motion.

The Hamiltonian H_0 for a single pillar site without coupling to any neighbor is then

$$H_0^{i,j} = \begin{pmatrix} \overline{\omega} & 0 \\ 0 & \overline{\omega} \end{pmatrix} + R(\alpha) \begin{pmatrix} \Delta & 0 \\ 0 & -\Delta \end{pmatrix} R^{-1}(\alpha) \tag{4.2}$$

$$\underbrace{=}_{\alpha=0} \begin{pmatrix} \overline{\omega}+\Delta & 0 \\ 0 & \overline{\omega}-\Delta \end{pmatrix} = \begin{pmatrix} \omega_x & 0 \\ 0 & \omega_y \end{pmatrix} \tag{4.3}$$

with mean frequency $\overline{\omega} = (\omega_x + \omega_y)/2$, asymmetry parameter Δ and angle of orientation of the ellipse α. In case the ellipse is oriented along either x or y direction the angle is

$\alpha = 0$ as stated before.

Now, we can extend the single pillar system by couplings to surrounding pillars. For an overview of the involved couplings, Figure 4.2 shows the surroundings of a single pillar site within the array.

In Section 3.3.3 it has been shown, that the coupling strength between nanopillars decreases with their distance. Thus, in this model only the coupling to direct neighbors, i.e. nearest neighbors and next nearest neighbors, is taken into account. These couplings are added as coupling springs in Figure 4.2. Both, the coupling to nearest neighbors J and to next nearest neighbors J_d is further distinguished by the relative vibration directions of the two involved pillars as schematically shown in Figure 4.2**b**. If a pillar moves orthogonally to the connection to its neighbor, the contribution is called transversal t. If the pillar moves along the connection to its neighbor this is referred to as longitudinal l. Thus, eight different hopping coefficients emerge in the form of transversal-transversal coupling J_tt ($J_\mathsf{d,tt}$), longitudinal-longitudinal coupling J_ll ($J_\mathsf{d,ll}$) and mixed couplings transversal-longitudinal or longitudinal-transversal $J_\mathsf{tl} = J_\mathsf{lt}$ ($J_\mathsf{d,tl} = J_\mathsf{d,lt}$), which are both equal due to symmetry.

Focusing on the single site i, j in the bulk of the array all parts contributing to the Hamiltonian can be identified in Figure 4.3. For more clarity, the next nearest neighbor coupling via J_d is not shown in the schematics in Figure 4.3 but follows correspondingly.

Each of these contributions is added to the unperturbed Hamiltonian (Equation (4.2)). In each of the four components, there is a pair of Hermitian conjugate (h.c.) contributions to the Hamiltonian due to their symmetry. Thus, the Hamiltonian for a single site i, j in the bulk of the array $H^{i,j}$ is

$$
\begin{aligned}
H^{i,j} = \quad & \underbrace{\omega_x^{i,j} b_x^{i,j\dagger} b_x^{i,j} + \omega_y b_y^{i,j\dagger} b_y^{i,j}}_{\text{single pillar contribution}} \\
& - \underbrace{\left[\left(J_\mathsf{ll} b_x^{i,j\dagger} b_x^{i+1,j} + J_\mathsf{tt} b_x^{i,j\dagger} b_x^{i,j+1}\right) + \text{h.c.}\right]}_{\text{x-x contribution}} - \underbrace{\left[\left(J_\mathsf{ll} b_y^{i,j\dagger} b_y^{i+1,j} + J_\mathsf{tt} b_y^{i,j\dagger} b_y^{i,j+1}\right) + \text{h.c.}\right]}_{\text{y-y contribution}} \\
& - \underbrace{\left[\left(J_\mathsf{lt} b_x^{i,j\dagger} b_y^{i+1,j} + J_\mathsf{lt} b_x^{i,j\dagger} b_y^{i,j+1}\right) + \text{h.c.}\right]}_{\text{x-y contribution}} - \underbrace{\left[\left(J_\mathsf{lt} b_y^{i,j\dagger} b_x^{i+1,j} + J_\mathsf{lt} b_y^{i,j\dagger} b_x^{i,j+1}\right) + \text{h.c.}\right]}_{\text{y-x contribution}} \\
& + H_\mathsf{d}^{i,j}.
\end{aligned}
\tag{4.4}
$$

The contributions from next nearest neighbor coupling J_d are here summarized in $H_\mathrm{d}^{i,j}$. Its form follows correspondingly so that transversal or longitudinal couplings are incorporated with their relative contribution. The explicit form of $H_\mathrm{d}^{i,j}$ can be found in Appendix E.

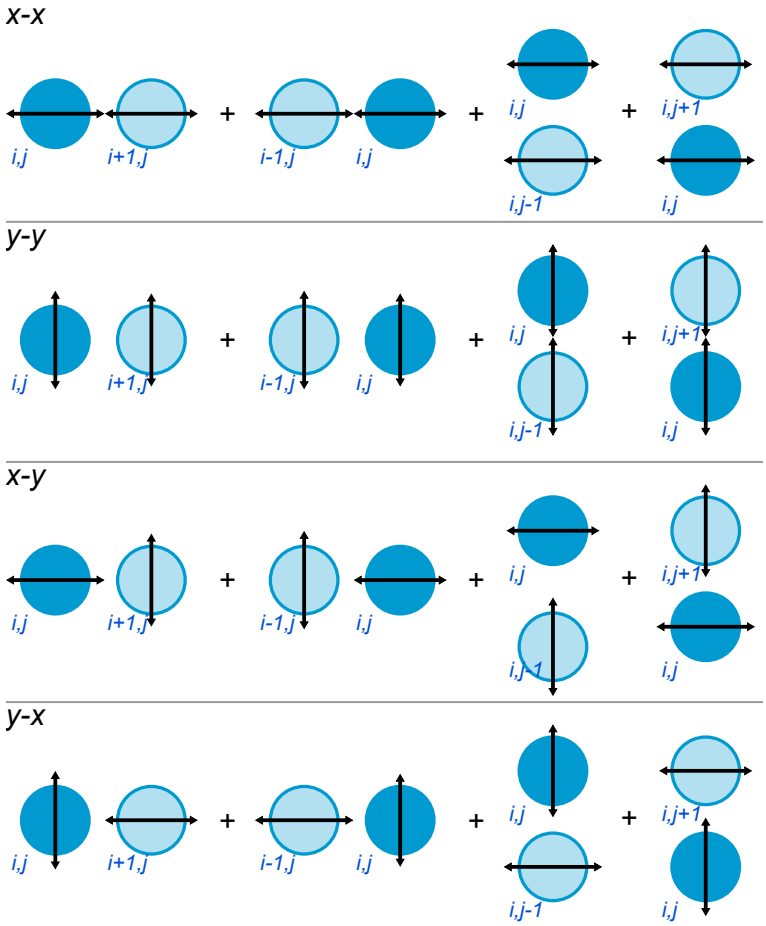

Figure 4.3: **Contributions to the Hamiltonian on site i,j.** Pillar on site i,j (●) and coupled nearest neighbors (●) with all possible contributions for either of the pillars vibrating in x or y direction. x-x (y-y): both pillars vibrate in x-direction (y-direction), x-y (y-x): pillar on i,j vibrates in x-direction (y-direction) while the coupling partner vibrates in y-direction (x-direction).

For pillars at the edge or corner of the array some of the interaction terms from Equation (4.4) are zero, as there are less neighbors to be taken into account. While a bulk pillar has eight direct neighbors, an edge pillar only has five direct neighbors and a pillar at the corner only three. This is not explicitly shown here.

Now, a general form of the single pillar Hamiltonian $H^{i,j}$ is found. The coupling $J_\mathrm{lt} = J_\mathrm{tl}$

is small compared to the other coupling strengths because the model assumes that the pillars are almost circular. Therefore, it can be neglected in the following.

To find a Hamiltonian for the whole system, a creation $|b^\dagger\rangle$ and annihilation operator $|b\rangle$ is defined to describe the whole array

$$|b\rangle \equiv \begin{pmatrix} b_x^{1,1} \\ b_y^{1,1} \\ b_x^{1,2} \\ b_y^{1,2} \\ \vdots \\ b_x^{1,N} \\ b_y^{1,N} \\ b_x^{2,1} \\ \vdots \\ b_x^{N,N} \\ b_y^{N,N} \end{pmatrix} \tag{4.5}$$

with the creation operator $|b^\dagger\rangle$ following correspondingly. With this, the total Hamiltonian of the system can be written as

$$H = \sum_{ij} H^{ij} = \langle b| \, \tilde{H} \, |b\rangle \tag{4.6}$$

with the matrix form of the Hamiltonian given by $\tilde{H}$ and $\langle b|$ is the row vector defined as $(|b\rangle)^\dagger$.

Now that the bare system is set, a drive is added to every nanopillar in the array in form of

$$|b(t)_{\mathsf{in}}\rangle = \begin{pmatrix} b_{\mathsf{in,x}}^{1,1} \\ b_{\mathsf{in,y}}^{1,1} \\ b_{\mathsf{in,x}}^{1,2} \\ b_{\mathsf{in,y}}^{1,2} \\ \vdots \\ b_{\mathsf{in,x}}^{1,N} \\ b_{\mathsf{in,y}}^{1,N} \\ b_{\mathsf{in,x}}^{2,1} \\ \vdots \\ b_{\mathsf{in,x}}^{N,N} \\ b_{\mathsf{in,y}}^{N,N} \end{pmatrix} \mathrm{e}^{-i\Omega_{\mathsf{exc}}t} = |b_{0,\mathsf{in}}\rangle \, \mathrm{e}^{-i\Omega_{\mathsf{exc}}t} \tag{4.7}$$

with drive frequency Ω_{exc}. Further, a similar damping constant of Γ is added to every nanopillar.

According to the input-output relations, the equation of motion of the pillar array is given by[55]

$$\frac{\mathrm{d}}{\mathrm{d}t}\left|b\right\rangle = -i\tilde{H}\left|b\right\rangle - \frac{\Gamma}{2}\left|b\right\rangle + \sqrt{\Gamma}\left|b(t)_{\mathsf{in}}\right\rangle . \tag{4.8}$$

Now, the time dependence can be separated with

$$\left|b(t)\right\rangle = \int_{-\infty}^{\infty} \mathrm{e}^{-i\omega t}\left|b(\omega)\right\rangle \mathrm{d}\omega. \tag{4.9}$$

Consequently, the equation of motion (4.8) reduces to

$$\left|b(\omega)\right\rangle = \left[i(\tilde{H} - \omega\mathbb{1}) + \frac{\Gamma}{2}\mathbb{1}\right]^{-1} \sqrt{\Gamma_{\mathsf{in}}}\left|b_{0,\mathsf{in}}\right\rangle \delta(\omega - \Omega_{\mathsf{exc}}). \tag{4.10}$$

With time dependence included, this leads to a steady state solution $\left|b_s(t)\right\rangle$

$$\left|b_s(t)\right\rangle = \int_{-\infty}^{\infty} \mathrm{e}^{-i\omega t}\left|b(\omega)\right\rangle \mathrm{d}\omega \tag{4.11}$$

$$= \left[i(\tilde{H} - \Omega_{\mathsf{exc}}\mathbb{1}) + \frac{\Gamma}{2}\mathbb{1}\right]^{-1} \sqrt{\Gamma_{\mathsf{in}}}\left|b_{\mathsf{in}}\right\rangle . \tag{4.12}$$

With these equations, the whole system of a coupled nanopillar array without disorder can be described. After solving the equations, one can now go back to a single pillar at site i, j to determine its steady state. The components

$$\begin{pmatrix} b(t)_x^{i,j} \\ b(t)_y^{i,j} \end{pmatrix} = \begin{pmatrix} A\mathrm{e}^{-i\Phi_x} \\ B\mathrm{e}^{-i\Phi_y} \end{pmatrix} \mathrm{e}^{-i\Omega_{\mathsf{exc}}t} \tag{4.13}$$

with amplitude A (B) can be extracted from the solution $\left|b_s(t)\right\rangle$. With Equation (4.1) this leads to

$$\begin{pmatrix} x(t)^{i,j} \\ y(t)^{i,j} \end{pmatrix} = 2\mathrm{Re}\begin{pmatrix} x_{\mathsf{zpf}} b(t)_x^{i,j} \\ y_{\mathsf{zpf}} b(t)_y^{i,j} \end{pmatrix} = 2\begin{pmatrix} x_{\mathsf{zpf}} A\cos\left(\Omega_{\mathsf{exc}}t + \Phi_x\right) \\ y_{\mathsf{zpf}} B\cos\left(\Omega_{\mathsf{exc}}t + \Phi_y\right) \end{pmatrix}. \tag{4.14}$$

In the most general case, this leads to an elliptical trajectory which can also be found in the single pillar case if the two orthogonal eigenfrequencies overlap. Special cases of the ellipse are a circle with minor and major axis of the ellipse equal and a linear motion where the minor axis vanishes. From the above parameters, the shape of the ellipse can be determined with Figure 4.4.

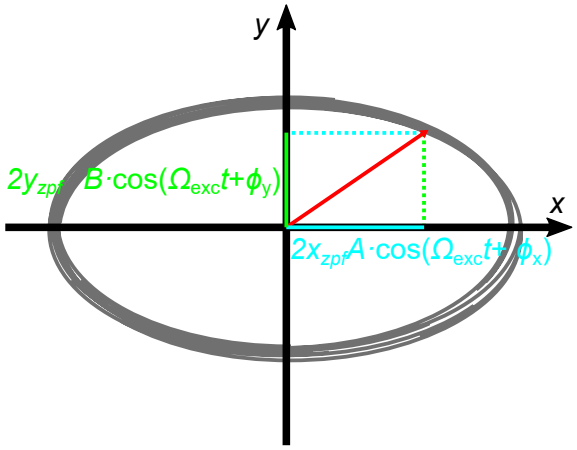

Figure 4.4: **Sketch of the pillar trajectory.** Sketch from a general pillar trajectory viewed from above. Amplitudes A and B as well as phases Φ_x and Φ_y determine the shape of the trajectory from pure circular or linear to elliptical shapes.

The exact formulas for the calculation of the pillar head trajectory can be found in Appendix E.

All these considerations apply to a homogeneous array without disorder. However, as it is shown in Section 2.4 and confirmed in Section 4.3, there is disorder in real pillar nanostructures. We find random and systematic disorder in nanopillar arrays (cf. Section 4.3). This fabrication induced disorder affects all experimentally determined parameters: the two orthogonal eigenfrequencies ω_x and ω_y and their vibration angle relative to the main lattice axes – note that the angle between the two modes remains at 90°. Additionally, supported by measurements in Section 3.3.3, we assume disorder in all involved coupling parameters.

All coupling parameters are perturbed with a Gaussian distribution. The distribution is centered at the respective parameter X – J_{tt}, J_{ll}, J_{lt}, $J_{\mathrm{d,tt}}$, $J_{\mathrm{d,ll}}$, $J_{\mathrm{d,lt}}$ – with a standard deviation $\sigma(X)$ depending on a *disorder* parameter

$$\sigma = \frac{\mathit{disorder}}{100}\mathrm{mean}(X). \tag{4.15}$$

This relative disorder is assumed constant for all parameters. The disorder of the eigenfrequencies is simulated by two separate forms of disorder, an isotropic disorder δ_{iso} and an anisotropic one δ_{aniso}. The isotropic disorder simulates the isotropic spread affecting both eigenfrequencies of a pillar which might be caused by different height of different nanopillars. The anisotropic disorder parameter simulates the disorder that can be found in the anisotropy varying from pillar to pillar. Thus, Equation (4.2) of the single site

Hamiltonian without coupling $H_0^{i,j}$ is extended to

$$H_0^{i,j} = \begin{pmatrix} \overline{\omega} + \delta_{\text{iso}} & 0 \\ 0 & \overline{\omega} + \delta_{\text{iso}} \end{pmatrix} + R(\alpha) \begin{pmatrix} \Delta & 0 \\ 0 & -\Delta \end{pmatrix} R^{-1}(\alpha) + R(\beta) \begin{pmatrix} \delta_{\text{aniso}} & 0 \\ 0 & \delta_{\text{aniso}} \end{pmatrix} R^{-1}(\beta). \tag{4.16}$$

Here, β is randomly distributed between 0° and 360°. δ_{iso} is modulated in a Gaussian distribution around 0 with standard deviation $\sigma(\delta_{\text{iso}}) = \textit{disorder}/100 \cdot \overline{\omega}$. Finally, the anisotropic disorder parameter is simulated with a Gaussian distribution around 0 with standard deviation $\sigma(\delta_{\text{aniso}}) = \textit{disorder}/100 \cdot \Delta$. The single site Hamiltonian without coupling $H_0^{i,j}$ can than be extended to the full Hamiltonian $H^{i,j}$ via Equation (4.4), where all couplings are taken from a Gaussian distribution as stated above.

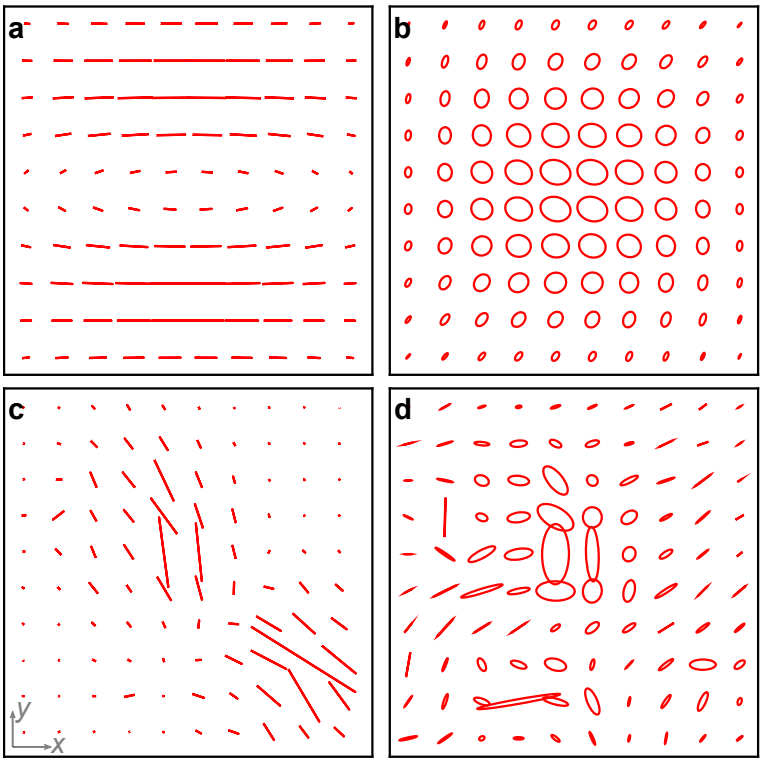

Figure 4.5: **Disorder comparison.** All panels show trajectories along x- and y-direction of a 10×10 pillar array with unperturbed eigenfrequencies $\omega_x = 1\,\text{MHz}$, $\omega_y = 1.005\,\text{MHz}$, coupling rates $J_{\text{ll}} = 10\,\text{kHz}$, $J_{\text{tt}} = J_{\text{d,ll}} = 5\,\text{kHz}$, $J_{\text{d,tt}} = 2.5\,\text{kHz}$ and $J_{\text{tl}} = J_{\text{d,tl}} = 0$. Exemplary eigenstate of the described array with **a** *disorder* $= 0$ at 0.96 MHz and **c** *disorder* $= 2$ at 0.95 MHz. Steady state for the array with **b** *disorder* $= 0$ at $\Omega_{\text{exc}} = 0.96\,\text{MHz}$ and **d** *disorder* $= 2$ at $\Omega_{\text{exc}} = 0.95\,\text{MHz}$. Damping is $\Gamma = 5\,\text{kHz}$.

Figure 4.5 illustrates the influence of disorder on eigenstates and steady states of a pillar

array. A 10×10 array is simulated with coupling and asymmetry parameters given in the caption of Figure 4.5. To identify the influence of disorder a first simulation does not incorporate any disorder ($\textit{disorder} = 0$) while in the second one *disorder* is set to 2. Both, in the eigenstate as well as the steady state a clear difference is visible. While in the homogeneous array the vibration pattern is spread over the whole array with rather smooth spatial variations, the disordered array shows more localized vibration patterns with rather sharp spatial variations.

This random disorder model serves as a first approach, that can, however, in the future be extended to a systematic frequency disorder with a gradient towards the edges as observed in our systems.

4.2 Imaging detection scheme

The vibration of each single nanopillar within an array can be detected via the laser based detection technique introduced in Section 2.3.1. This technique is nevertheless not efficient to measure the vibration pattern of a whole array since the focused laser spot would have to be moved across the array to measure each pillar individually. For this reason, we developed an imaging detection scheme that allows for the simultaneous detection of all pillars in the array and provides information about the vibration direction of each pillar.

As in Section 2.3.1, the driven nanopillar array is optically imaged from above. The large amplitudes of nanopillars combined with a high resolution of the setup allow for the visualization of the vibration amplitudes of many nanopillars at once.

In the following, two main components of this technique and their challenges are described: the imaging setup, which allows to record the full driven array with high resolution and the automated analysis technique, which is necessary to process a large number of recorded images in an automatized way with sub-pixel amplitude resolution.

4.2.1 Imaging setup

A high image resolution for the imaging detection technique can be achieved by using a commercial optical microscope with large magnification up to $100\times$. However, a commercial microscope with multiple users comes with a few disadvantages, which minimize the flexibility. Among these limitations are the control of the surrounding atmosphere, controlled positioning and long-term position stability of the sample, limited access as well as rearranging all added components for every measurement.

Thus, the in-situ imaging of the laser detection setup is upgraded to achieve a high resolution. This provides the advantage of a controllable pressure in a vacuum chamber,

positioning via a piezo positioning stage as well as flexibility for the use of the setup. Additionally, just a few rearrangements allow to switch between the laser-based detection and the imaging detection, thus, providing additional flexibility in the detection technique without remounting the sample.

Figure 4.6 shows a sketch of the imaging setup.

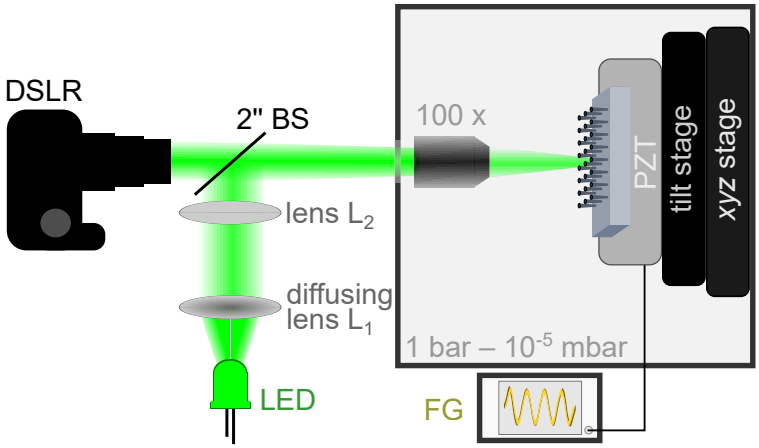

Figure 4.6: **Imaging setup.** Schematic of the imaging detection setup with green LED illumination, 2.5 mm diffusing condenser lens (L_1), a second 10 mm focusing lens (L_2), a 2″ beam splitter (BS) with $R : T$ split ratio 50 % : 50 % and anti reflection coating, a 100× microscope objective, a DSLR camera, an electrically controlled xyz-piezo positioning stage, a manually controlled tilt stage, a piezoelectric transducer (PZT) and a function generator (FG).

The imaging setup mainly consists of a self-built optical microscope, with green light-emitting diode (LED) illumination with a diffusing condenser lens and a second focusing lens, a microscope objective and a digital single-lens reflex (DSLR) camera with an 18 megapixel CMOS sensor.

The green LED provides monochromatic illumination of the sample, thus, preventing chromatic aberration, which would diminish the image quality and therefore, the sensitivity. Since the number of green pixels in our camera is twice the number of red or blue pixels as it has a *Bayer*-CMOS sensor grid, a green LED is chosen as monochromatic light source. This way, we benefit from the enhanced sensitivity of the camera in the green color range. The diffusing condenser lens has a grainy surface and aids to diffuse the LED light pattern, which prevents that the LED's inner structure is imaged on the sample and ensures homogeneous illumination. The second lens focuses the beam at a plane far behind the objective in order to narrow the beam at the aperture of the objective and feed more light through the rather narrow aperture. A $100\times$ microscope

objective ensures a large magnification and thus, a high resolution of the recorded images. A commercial Canon DSLR camera with a *Matlab* interface provides a high image resolution as well as remote access recording.

The sample is mounted on a mechanical tilt stage, which is mounted on top of an *Attocube* x-y-z positioning stage. This allows for positioning the sample with µm precision in all 5 degrees of freedom. The stack is placed in a vacuum chamber with optical access. The pressure in the vacuum chamber can be controlled from atmospheric pressure down to 10^{-6} mbar.

Furthermore, irises and beam dumps are used to keep stray light from the camera, which could decrease the contrast significantly. All optical components from the original laser detection setup that are not strictly necessary here are removed to increase the illumination efficiency and to reduce unnecessary reflections which could reduce the image contrast. Moreover, 2 inch optics are used for a large field of view, allowing for a field of view of more than $(100 \times 100)\,\mu m^2$ while keeping a high resolution.

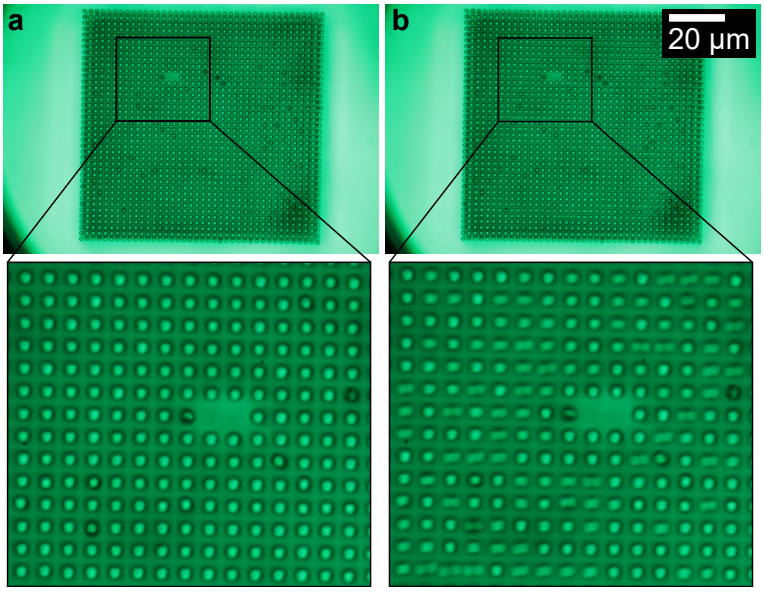

Figure 4.7: **Imaging of driven nanopillar array.** **a**, Image of a 40 × 40 nanopillar array with $R = 500\,nm$, $a = 2.4\,\mu m$ and $H \approx 12\,\mu m$ in the imaging setup without drive. **b**, Image of the array in **a** with on-resonant drive applied at ambient conditions. A zoom on the images from **a** & **b** shows a region with several moving pillars[3].

[3]Some pillar heads show an irregular contrast, which is probably due to mask degrading since the shown array is several years old. Further, in the zoom region there is a hole, which indicates two missing pillars.

This setup allows for remote controlled, long-time measurements under variable pressure with precise and stable positioning technique.

Figure 4.7 shows exemplary image recordings in the imaging setup of a 40×40 nanopillar array. The resonantly driven vibrations in Figure 4.7**b** can be clearly distinguished from the non-moving pillars in Figure 4.7**a**, where no driving force is applied.

4.2.2 Recording routine

A *Matlab* measurement script remotely controls the function generator and *Canon* DSLR camera via the open source software *digiCamControl* to capture measurement images in a pre-defined frequency sweep. A continuous frequency sweep prevents a clear assignment of image and drive frequency, thus, a slow step wise frequency sweep is used. A fixed drive frequency is fed to the function generator. Subsequently, an image is taken before the script goes on to the next frequency.

A measurement based on this scheme, however, will produce a data set with a very slight, arbitrary drift of the positioning stage in all three directions. While x & y in-plane drifts can be compensated in the following image analysis, a correction of the random z-drift, i.e. a very small drift of the sample in and out of focus can not be compensated analytically. Although the drift is visually barely detectable, it strongly affects the data extracted from the image, namely the size of the pillar outline. Therefore, every image is referenced to a respective non-driven image, which is taken immediately before the driven image. This way the number of recorded images and thus, the size of the recorded data is doubled, but at the same time, the sensitivity of the measurement is considerably enhanced.

It is worth noting that the software *digiCamControl* runs out of memory if too many pictures are taken in one session. Thus, the script includes a counter to reset the software after 2000 images.

4.2.3 Image analysis algorithm

A frequency sweep that covers the whole relevant spectrum and provides a high frequency resolution usually produces 10 000 images including reference images. A manual search or analysis of these images would be impractical. Thus, I developed an automatized image analysis algorithm based on *OpenCV* in *Python*.

A stepwise description of this algorithm is given in this section with all relevant intermediate stages explained. Additionally, exemplary fragments of the code can be found in Appendix D.

In a first optional step, the images are aligned to one another to compensate for the in-plane drift utilizing the openly available *StackReg* plugin.[4] This is not strictly necessary, since the reference images are taken right before the measurement images (Section 4.2.2). However, it can still be helpful when considering a specific pillar over the whole range of a frequency sweep. An example for such a compensation is indicated in Figure 4.8, where the green lines indicate the compensation added to the image.

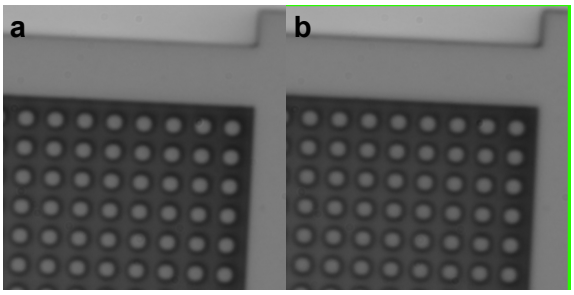

Figure 4.8: **In-plane drift compensation.** **a**, Reference image. **b**, False color image aligned to the reference image in **a**. Green lines are added pixels compensating for the drift. The two images are taken several hours apart.

Figure 4.9 shows the analysis routine with all intermediate steps displayed for an on-resonance driven image and the corresponding reference image. The unmodified recorded images are shown in Figure 4.9**a** for the resonantly driven image in the upper panel and the corresponding non-driven reference image in the lower panel.

In the first step, the colored image is converted to a gray scale image as seen in Figure 4.9**b**. This allows to deal with a gray value alone instead of the three parameters in the red-green-blue (*rgb*) system. Although the green intensity is much higher than the red and blue one, one always finds a non-zero red and blue value in the recorded images.

For the conversion to gray scale, there are basically two methods: On the one hand, the *rgb* image can be converted to gray-scale using all three color components. Here the three intensity values for the colors red r, green g and blue b are averaged $(r+g+b)/3$. In a second approach, one neglects the red and blue channel and only extracts the green color component, since the green LED illumination suggests that the main intensity contribution is in the green channel.

In a comparison, both methods yield good results. Although, the green channel alone should yield better resolution due to suppression of chromatic aberration, the averaged image seems to yield slightly better contrast, which is crucial for the next step. Thus, the averaging approach is used for the analysis. Note, however, that the contrast can

[4] `https://pypi.org/project/pystackreg/`

change from sample to sample and from array to array, which is why it can be useful, to decide for every array individually, which method yields better results.

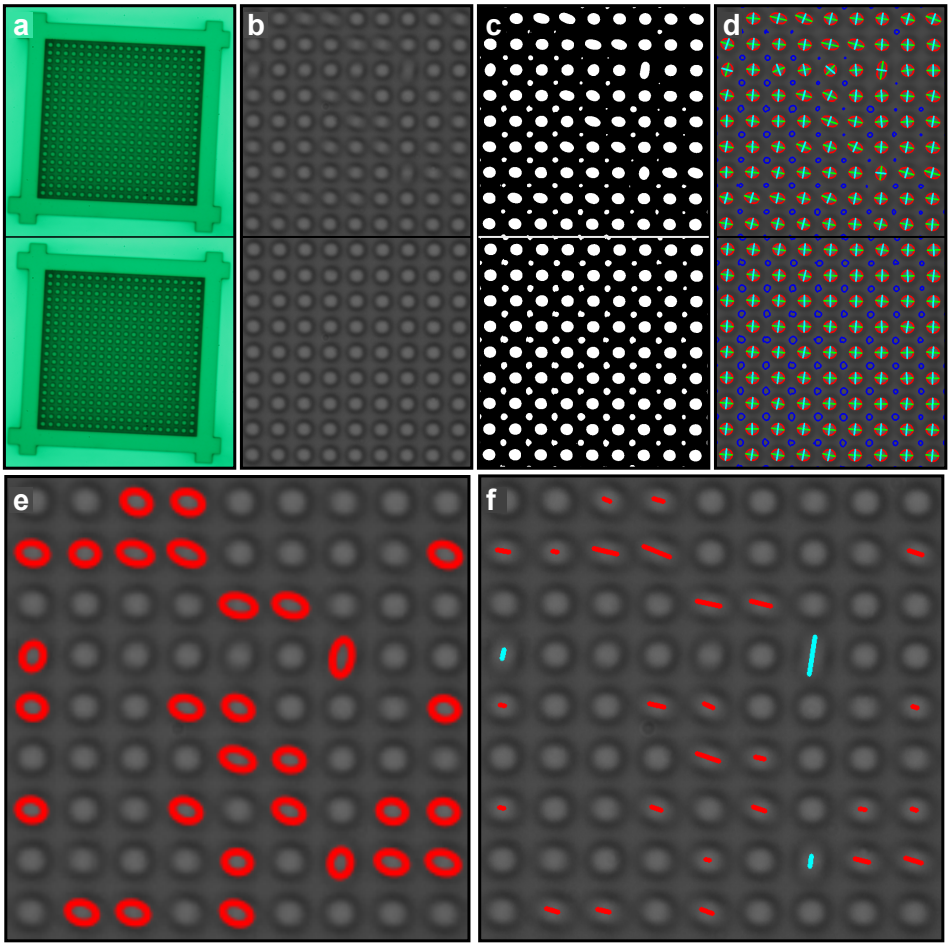

Figure 4.9: **Image analysis routine. a-d**, Stepwise analysis routine for an exemplary driven measurement (upper panel) and the respective non-driven reference image (lower panel): **a**, original recorded images; **b**, gray-scale images cut to the array size; **c**, binarized images using an adaptive threshold; **d**, gray-scale images overlaid with detected outlines of pillars (red) and smaller or larger features (blue) as well as the major (green) and minor axes (cyan) of all red outlines. **e**, Moving pillars marked with red elliptical outlines. **f**, Amplitudes of the detected moving pillars (enlarged by a factor of 3) in approximately horizontal (red) and vertical (cyan) direction.

In the next step, the image is binarized with the result shown in Figure 4.9**c**. In the most simple way, a global threshold would be set for the gray value. Above this threshold, values are set to 255 (white) and below it values are set to 0 (black). In order to compensate for a gradient along the image due to slightly inhomogeneous lightning or a

small tilt in the sample positioning, there is no global threshold set but a local threshold. To that end, *OpenCV* provides the function `cv2.adaptiveThreshold`.

The local threshold is calculated with respect to the mean of an area with given *block size*. The mean can be calculated as a simple average by `cv2.ADAPTIVE_THRESH_MEAN_C` or as a weighted average with a Gaussian distribution `cv2.ADAPTIVE_THRESH_GAUSSIAN_C`. The final threshold value can be controlled by a parameter `C`, which is subtracted from the calculated mean. For the analysis of the pillar images, the weighted average is chosen, since it yields smoother contours around the moving pillars.

The resulting contours are sorted via their size. Contour outlines in the size of a pillar head are drawn in red, the ones with too small or too large enclosing area are drawn in blue (cf. Figure 4.9**d**). For the array in Figure 4.9, one finds small white artifacts right between two next-nearest neighbors. The large distance between next-nearest neighbors gives a rather large open area that allows for the light to be reflected off unhindered and sets the gray value above the threshold. On the other hand, the smaller distance to nearest neighbors combined with the rather large pillar height decreases the reflectivity in this region and produces a shadow with low gray value. These artifacts can become larger or even vanish depending on the inter-pillar distance and pillar height.

Now, the center position, the major and minor axes as well as the orientation of all "blobs" are determined. To that end, the function *image moments* is employed.

Image moments. *Image moments* is used in image processing and uses the pixels' intensities to calculate weighted averages, called moments. These image moments can be used to find general properties of a random shape as the center position or orientation of a blob. This makes it ideally suited to analyze the images of moving pillars. In the following, the fundamental concept of image moments is outlined. [56,57]

For a two dimensional image with pixels (x, y) and intensity function $I(x, y)$, the $(p+q)$th order image moment m_{pq} is defined as

$$m_{pq} = \int \int_{\Omega} x^p y^q I(x, y) \mathrm{d}x \mathrm{d}y \tag{4.17}$$

with Ω the space of all image pixels.

For a binarized image, the intensity function simplifies to

$$I(x, y) = \begin{cases} 1 & \text{object pixel} \\ 0 & \text{background pixel.} \end{cases} \tag{4.18}$$

Further, the two integrals are each replaced by a summation in the case of a digital

image. Thus, the image moments reduce to

$$m_{pq} = \sum_{\xi} x^p y^q \tag{4.19}$$

with ξ the object pixel space as a subset of Ω.

From there, first object properties can be described:

1. **Object area**, i.e. the number of object pixels N given by the zero-order moment

$$m_{00} = \sum_{\xi} x^0 y^0 = N. \tag{4.20}$$

2. **Object centroid** (x_c, y_c), given by a combination of zero-order and first-order moments

$$x_c = \frac{m_{10}}{m_{00}} = \frac{\sum_{\xi} x}{N} \tag{4.21}$$

$$y_c = \frac{m_{01}}{m_{00}} = \frac{\sum_{\xi} y}{N}. \tag{4.22}$$

With the object centroid, the translation invariant central moments μ_{pq} can be defined

$$\mu_{pq} = \sum_{\xi} (x - x_c)^p (y - y_c)^q. \tag{4.23}$$

The examination of an object is now simplified by considering the ellipse of inertia, which corresponds in the binarized image to the best fit ellipse. This prompts the definition of the inertial tensor J

$$J = \frac{1}{\mu_{00}} \begin{pmatrix} \mu_{20} & \mu_{11} \\ \mu_{11} & \mu_{02} \end{pmatrix}. \tag{4.24}$$

The eigenvectors e_1 and e_2 of J correspond to the orthogonal major and minor axes of the best fit ellipse. Therefore, the orientation of the blob is given by the two eigenvectors. In the next step, the extension of the blob l and w can by calculated with the two eigenvalues $\lambda_{1,2}$ of the matrix

$$l = 2\sqrt{\lambda_1}, \tag{4.25}$$

$$w = 2\sqrt{\lambda_2}. \tag{4.26}$$

Thus, using the tool of *image moments* integrated in *Python*, one can determine the

characteristic parameters of a best fit ellipse to the outline of every pillar blob.

On a further note, the approach based on image moments is equivalent to the method utilizing the covariance matrix. To identify the connection, we consider the covariance matrix C of N points (x, y)

$$C = \begin{pmatrix} \mathrm{Cov}(x,x) & \mathrm{Cov}(x,y) \\ \mathrm{Cov}(y,x) & \mathrm{Cov}(y,y) \end{pmatrix}. \tag{4.27}$$

The covariance $\mathrm{Cov}(x, y)$ for a binarized image is

$$\mathrm{Cov}(x,y) = \sum_{\xi}^{N} (x - \overline{x})(y - \overline{y})/N \tag{4.28}$$

with the average values $\overline{x}$ and $\overline{y}$. The covariances $\mathrm{Cov}(x, x)$ and $\mathrm{Cov}(y, y)$ are calculated accordingly.

By identifying $(\overline{x}, \overline{y})$ with the formerly defined centroid (x_c, y_c), the covariance matrix C is found to be equal to the inertial tensor J

$$J = C. \tag{4.29}$$

The in *Python* integrated function for *image moments* `cv2.moments`, allows to call the $(p + q)$th order moment by `'mpq'`, e.g. `'m00'` for the zero-order image moment.

This procedure to identify a major and minor axis of a blob can determine the shape of any moving pillar, whether it is a linear movement, where the blob will be a very flat ellipse; an elliptical movement, with the ellipticity slightly reduced; or a circle, where the two axes can become equally long. The reduction from the three dimensional amplitude to a two dimensional one is justified for small amplitudes (cf. Appendix B.2).

However, the procedure can be misleading when considering a pillar that is not moving. A small ellipticity in the pillar head or a slight distortion in the imaging can already produce an ellipticity in the detected pillar shape, even though, the pillar is not moving. Since every moving pillar is compared to a non-moving reference, the ellipticity of the reference can play an important role. If the reference pillar shape is analyzed by moments, it is possible that the extension of the reference pillar is measured along a different axis than for the moving pillar. This can yield wrong results, when these two extensions are compared, especially for small amplitudes. To prevent this, the extension of the reference pillar is not measured along its own major and minor axes, but it is measured along the major and minor axes directions identified for the moving pillar. This way, a change in these quantities is directly measured and compared.

In the previous steps, the extensions of both the driven pillar image and the non-driven pillar image have been determined. In the next step, these extensions are compared for every single pillar and direction. If there is a significant enlargement with a minimum threshold of 1 px from a reference pillar's head to a driven pillar's head in any of the two directions, the pillar is marked as vibrating with its outline drawn as in Figure 4.9**e**. Furthermore, the amplitude is drawn in Figure 4.9**f**. If only the pillar's major axis is enlarged, we identify the motion as purely linear. If, however, both axes are enlarged, we identify the motion as elliptical. The amplitudes are drawn in red (cyan) for predominantly horizontal (vertical) linear motion and green for elliptical motion (not apparent in Figure 4.9**f**). The amplitudes are enlarged by a factor of 3 in order to make the amplitudes clearly visible.

The distinction between vibrating and non-vibrating pillars mainly depends on the comparison between the two outlines. Because there are always some random fluctuations between the size of the two outlines a threshold needs to be set above which the deviation is defined as an amplitude, which is to be distinguished from purely random fluctuations. A suitable threshold needs to be found for every measurement set individually, since contrast changes greatly influence the performance of the algorithm. The lowest reasonable threshold for the deviation in a blob is a single pixel 1 px, which makes the minimum amplitude threshold 0.5 px. However, depending on the contrast of the images, this can lead to falsely identified vibrating pillars. A larger threshold, on the other hand, reduces the sensitivity of the measurement. Therefore, the two aspects have to be balanced for every measurement set individually to identify a suitable threshold. Typically, 1 px is used as a compromise.

Visual inspection of the results of the algorithm reveals that the algorithm seems to be efficient to detect moving pillars with their direction of motion over a large range of data sets. However, there are some limitations to the algorithm, which will be addressed in the following.

First, it becomes apparent that extremely large amplitudes, as shown in Figure 4.10, are not detected by the image processing routine. A moving pillar has its longest dwell time at the turning points of the vibration. Since the shutter time of the camera ($\approx 0.5\,\mathrm{s}$) is much longer than a vibration period ($\approx 10^{-6}\,\mathrm{s}$), the image is a time integration over several periods of vibration. This way, the contrast of the turning points is much higher than at any other deflection point of the pillar. When amplitudes exceed the radius of the pillar head, the moving pillar appears as two disjunct circles at the places of the two turning points.

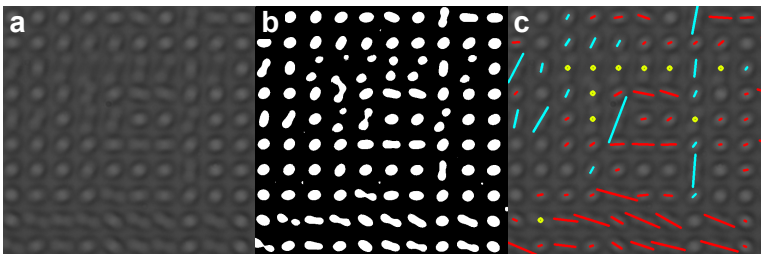

Figure 4.10: **Limitations for large amplitudes. a**, Recorded reference image converted to gray-scale. **b**, Binarized image. **c**, Marked vibrations with yellow dots for pillars with amplitudes that are too large to be detected with the algorithm.

In that case, the pillar exhibiting the large-amplitude vibration appears too close to its neighbor to be distinguished as a separate blob. Because of that, these pillars are merely marked with a yellow dot as displayed in Figure 4.10. Extremely large amplitudes are to be avoided in general, to stay in the linear response regime and to avoid breaking off individual pillars. An example for such large amplitudes and the results of the algorithm are shown in Figure 4.10.

In order to study the general performance of the algorithm, an image with moving pillars is simulated. By superimposing two non-driven images of pillars with a few pixels offset, the resulting image resembles an image where every pillar is vibrating, with an amplitude of half the offset between the two images. Such a simulated image and its reference is presented in Figure 4.11.

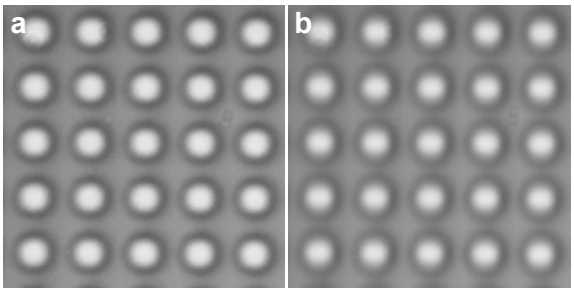

Figure 4.11: **Simulated measurement image. a**, Recorded reference image converted to gray-scale. **b**, Measurement image with a 5 px amplitude linear vertical vibration of all pillars.

The studies of the algorithm with simulated data with different amplitudes shows, that small amplitudes below 4 to 5 px are not consistently detected. Larger amplitudes, on the other hand, are reliably detected. Nonetheless, the simulated data and the real data show rather different contrasts. This limits the comparison of the two data sets and thus, sets limits to the significance of this test for the validity of the algorithm. By detecting real moving pillars, the algorithm seems much more effective than in the simulated test

which is confirmed visually. Still, small detected amplitudes need to be treated carefully and occasionally a moving pillar with a small amplitude is not detected by the algorithm, which needs to be taken into consideration. In general, the algorithm is rather effective in detecting linear and elliptical motions of nanopillars recorded in the imaging detection setup.

A way to overcome these limitations in the future could be a machine learning algorithm for the detection of moving pillars.

4.3 Eigenfrequency distribution in a nanopillar array

In Section 2.4, I showed that the inhomogeneous surrounding of a pillar or a group greatly influences the etch depth. The main consequence is an array of pillars with different heights, where the highest pillars are located at the edge of the array and shortest ones in the center. This directly translates into a frequency gradient over the array.

In this section, I propose different array layouts that can reduce this frequency gradient. Particularly, the surroundings of the array are altered in order to homogenize the surrounding of every pillar. The layouts investigated here are merely first approaches to the challenge of overcoming the systematic frequency gradient in arrays and still leave room for further optimization in future works.

Three different nanopillar array layouts are investigated. A simple pillar array as shown in Figure 4.12**a** consists of closely packed nanopillars and a blank surrounding. Such an array is presumably inherent of a systematic frequency gradient.

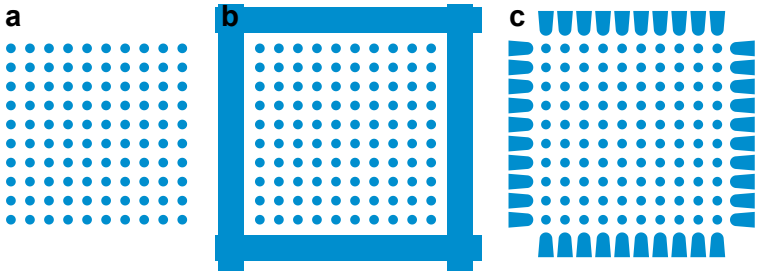

Figure 4.12: **Array layouts.** **a**, Simple 10×10 pillar array layout without wall. **b**, 10×10 pillar array layout with simple block wall. **c**, 10×10 pillar array layout with "knob wall".

Figure 4.12**b** &**c** show two alternative layouts with a homogenized surrounding in the form of a wall around the pillar array. The design in Figure 4.12**b** is a wall consisting of rectangles. This represents the most simple approach, however, mimicking a continuation of the array even beyond its boundaries in order to create homogeneous etch

conditions is most likely better in the design in Figure 4.12**c**. This third layout, on the other hand, while imitating pillars surrounding the actual array better, is also more fragile and stands greater risk of vibrating at similar frequencies as the nanopillars themselves.

In this first attempt, the edge-to-edge distance of the outer pillar rows and columns to the respective wall is matched with the edge-to-edge pillar distance to mimic the continuation of the array. Further, both walls are designed to be considerably stiffer than the pillars themselves, to avoid vibrations of the wall in the same frequency range as the pillars vibrate.

Now, the actual frequency distribution in such arrays is investigated to determine the influence of the different wall designs.

Exemplary pillar arrays with bottom radius $r \approx 290\,\mathrm{nm}$, approximate height[5] $H \approx 7.5\,\mu\mathrm{m}$, taper angle $\varphi \approx 1.6°$ and center-to-center distance $d = 2.6\,\mu\mathrm{m}$ are examined. Figure 4.13**a** shows scanning electron micrographs of the three array types.

The resonance frequencies are mapped out by measuring frequency response curves with the laser-based detection scheme. The laser is focused on a single pillar in the array. However, due to the closeness of the pillars and the size of the laser spot, there is some stray field detection of neighboring pillars. Because of that and because of possible coupling, the frequency response spectrum shows several peaks. The main peak can be determined employing the laser-induced tuning, since mostly the observed pillar is heated up. Due to possible coupling however, the frequencies are not clearly assigned to a single pillar. Since the pillars here are moderately far apart ($d = 2.6\,\mu\mathrm{m}$) one could assume a rather small coupling rate (cf. Section 3.3.3) compared to the frequency disorder. Based on this, coupling should probably have a negligible impact on the eigenfrequencies in these particular arrays. Nevertheless, identifying the main peak in the spectrum is only an approximation to determine the frequency spread of the array.

The frequency distributions in these arrays are summarized in Figure 4.13**b** & **c**. For each array, there are two maps of resonance frequencies, distinguished in a lower and a higher frequency mode. The two mode branches are generally split far apart for this particular sample with mostly consistent direction of motion in a particular branch – horizontal or vertical, respectively. This is caused by a large anisotropy in the nanopillar heads as shown previously (cf. Section 2.4).

[5] The height of pillars can only be measured in arrays without a wall and only for outermost pillars, which are usually longer than central ones (cf. Section 2.4). Thus, the given height is measured for the outer pillars of an array with the layout from Figure 4.12**a**. All different array types are on the same sample and thus, the pillars should be roughly of the same height.

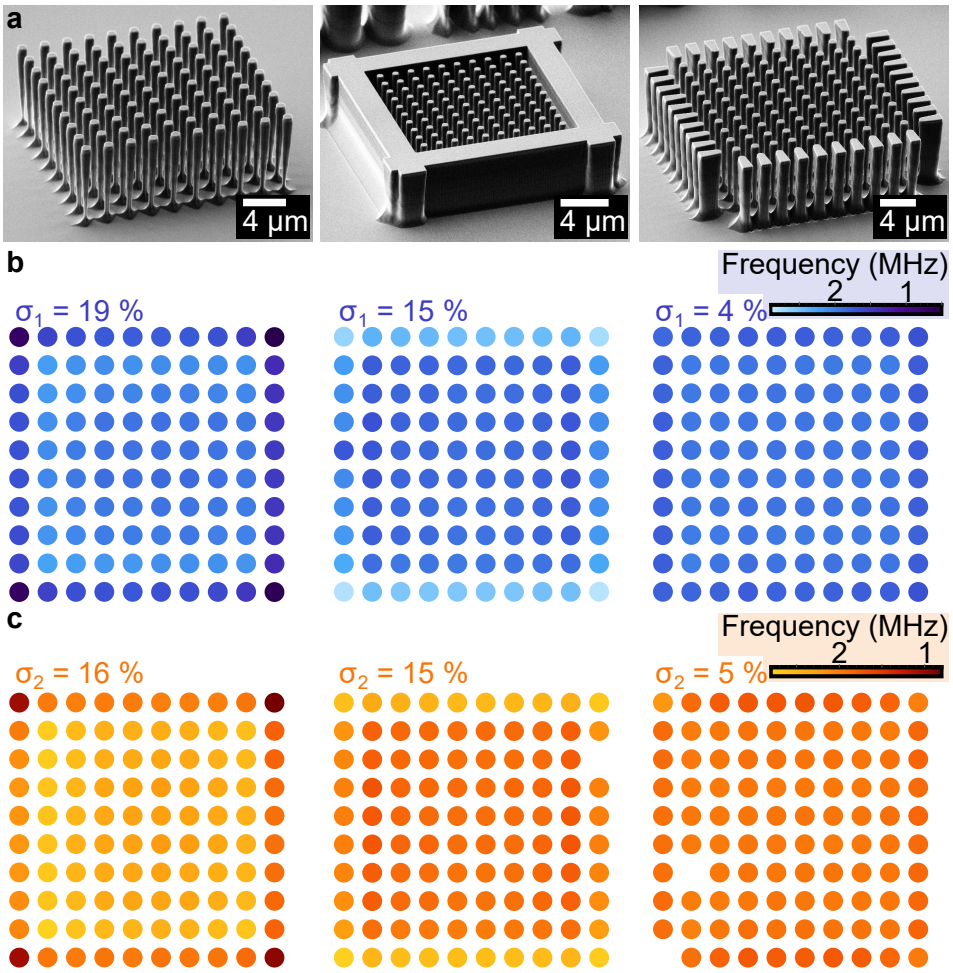

Figure 4.13: **Array statistics.** **a**, Scanning electron micrographs of arrays with the three different layouts from Figure 4.12 in a 60° tilted view. **b**, Frequency map of the lower frequency mode of each pillar in the array. **c**, Frequency map of the higher frequency mode of each pillar in the array. Corresponding array micrographs and frequency maps are aligned on top of each other. All frequencies are detected with the laser based detection scheme. Standard deviation with respect to the frequency mean is indicated above the frequency maps. Missing dots in **c** are undetectable modes.

However, the branch separation is not fully consistent, because the systematic frequency gradient from the center towards the edge can influence the two directions of motion with different strength.

With the observations in Section 2.4, the simple array in the left column of Figure 4.13 behaves as expected. The frequencies of both modes are higher in the center and drop gradually when observing nanopillars closer to the edges. As a measure for compari-

son of the arrays, the standard deviation of the whole array with respect to the mean frequency is calculated, σ_1 for the lower frequency mode and σ_2 for the higher frequency mode. For both modes these values are very high in the simple array design with $\sigma_1 = 19\,\%$ and $\sigma_2 = 16\,\%$. The branches are considered separately to disregard of the anisotropy for the moment which is a different disorder effect than the one targeted here.

Contrary to this is the frequency distribution of the array with the simple block wall, displayed in the middle column of Figure 4.13. There, the eigenfrequencies increase towards the edge, instead of decreasing. The standard deviations are $\sigma_1 = 15\,\%$ and $\sigma_2 = 15\,\%$. In comparison, the standard deviation is slightly reduced to the simple array. However, the improvement is rather small and could potentially even lie within random deviations as indicated by the asymmetrical standard deviation in the first array.

The continuous wall presents a much stronger confinement for the plasma during etching than a neighboring pillar. This, in turn, leads to an overcompensation of the etch inhomogeneity and thus, to the observed reversed eigenfrequency gradient.

The third layout option, the "knob wall", is shown in the right column of Figure 4.13. It is immediately visible, that the distribution of the eigenfrequencies is much narrower than for the first two designs. This becomes apparent through the absence of very dark or very bright measurement dots. Instead, the color distribution looks rather homogeneous with only a very slight gradient towards the array edges. Only the outermost pillars are slightly affected by the edge effect, they show a slightly smaller eigenfrequency than the central pillars.
The standard deviations of frequencies in this third design array amount to $\sigma_1 = 4\,\%$ and $\sigma_2 = 5\,\%$. This shows clearly a drastic improvement in the homogeneity of the eigenfrequencies. Therefore, the "knob wall" design clearly beats the two other designs in overcoming the systematic eigenfrequency gradient.
However, there still is a slight decrease towards the edges as well as the standard deviation is still larger than random fluctuations, which are usually up to $2\,\%$ according to analysis of pillars in the center of an array. This indicates, that there still is room for improvement.

Both of the proposed alternative designs are suitable to alter the systematic eigenfrequency distribution. Small adjustments in these designs could already render the eigenfrequencies in the array more uniform. The adjustment of the spacing between the outermost pillars and the respective wall seems particularly suitable to improve the designs: Increasing the spacing from the simple block wall to the pillars gradually should release the strong confinement progressively and leave an optimum before it again approaches the simple array design without wall. Similarly, one could adjust the distance of the knobs in the third array design. Since the eigenfrequencies are still a little bit too low, a decrease of the distance should improve the uniformity and possibly even fully

erase the systematic frequency disorder in arrays. To obtain the optimum distance of the wall to the array one can in the future either advance iteratively or implement a simulation of the etching process for different wall designs.

4.4 Collective dynamics of nanomechanical pillar arrays

In this section, the collective dynamics of a lattice of nanopillars is investigated.

The collective dynamics of the arrays is investigated by the aforementioned imaging method and image processing scheme. All measurements discussed here are taken at atmospheric pressure to increase the overlap of orthogonal modes. Furthermore, the driving shear piezo was placed at an angle of 45° relative to the sample edge to equalize the drive strength of horizontal and vertical modes.

There are many different factors determining whether a particular array is suitable for the measurement of collective dynamics, e.g.: the pillars have to be long to show amplitudes large enough to be detected; the frequency anisotropy in each pillar should be small to find overlap in the two modes; the disorder should not be too large in order to observe coupling; the frequency gradient towards the edges of the array should be small so that many pillars in the array can contribute to collective modes. These combined conditions are rare to find and from all investigated arrays, two that fulfill most (but not all) of these criteria are discussed here. The two arrays are, however, not equipped with the "knob" wall that has proven best to diminish the systematic frequency gradient. Nevertheless, the two arrays are still most suitable for the investigations here.

The first array under investigation is a 20×20 square lattice, with lattice parameter $d = 2.0\,\mu m$. The array is surrounded by a simple rectangular wall as introduced in Figure 4.12. The pillars[6] have a bottom radius of $r \approx 330\,nm$, a height of $H \approx 9.3\,\mu m$ and a taper angle of $\varphi \approx 1°$. A scanning electron micrograph of the investigated array is shown in Figure 4.14**a**. Note that for all measurements presented here, the array was still intact. The missing pillars in Figure 4.14**a** are lost later on.

To have an overview of the frequency response of the array a frequency resolved histogram is plotted in Figure 4.14**b**. The number of moving pillars are counted for each frequency. The histogram clearly indicates several frequency ranges, where a number of pillars is moving.

[6]Note that these parameters are measured for other arrays on the same sample, which should approximately have the same parameters. As before the wall prevents measurements of the geometry of the array under investigation.

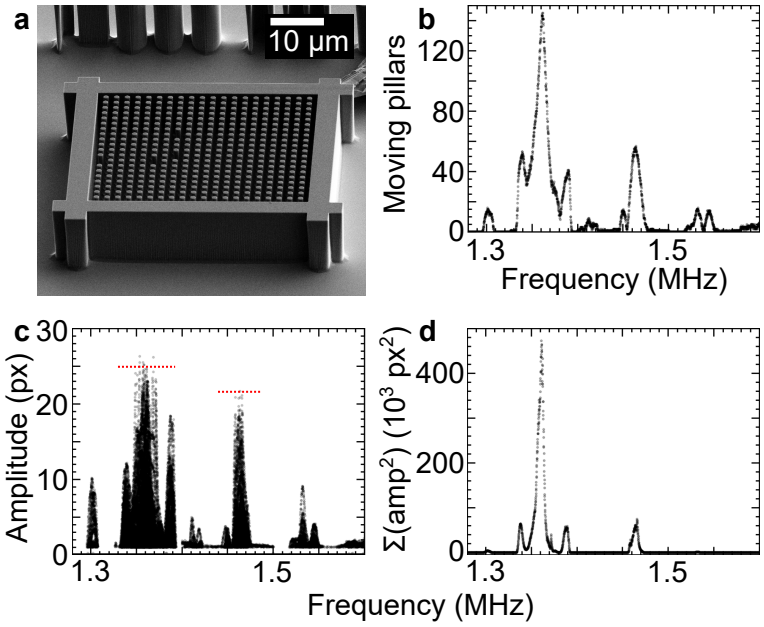

Figure 4.14: **Overview of a first coupled pillar array.** **a**, Scanning electron micrograph of the investigated pillar array in a 60° tilted view. **b**, Histogram of the pillar array, counting the number of moving pillars for each frequency. **c**, Overlay of the frequency response of each pillar in the array. Red lines indicate the upper detection threshold for amplitudes. **d**, Sum over all squared pillar amplitudes for each frequency.

We find a number of distinct peaks in the histogram in Figure 4.14**b**. The peaks are clearly defined without any outliers and blurring of the shape. Additionally, many pillars are part of single vibration patterns with the result that up to 140 pillar vibrate at the same frequency.

To identify the amplitude evolution, the frequency response of every pillar is plotted in Figure 4.14**c**. In the frequency response traces the same peaks as the ones in the previous histogram (Figure 4.14**b**) can be found again and identified as linear response modes of several pillars vibrating at once. Each peak in the frequency response traces can be clearly distinguished and has roughly the width of a single pillar mode of several kHz. This indicates that the modes show a simultaneous amplitude evolution and all involved pillar traces peak at the same frequency, since otherwise the peaks should be broadened from disorder and random outliers. Thus, it suggests that every peak is a single mode with a large number of coupled pillars vibrating.

It should be noted that the peaks are cutoff at large amplitudes above roughly 23 px (indicated by red lines in Figure 4.14**c**). This is because pillars with very large amplitudes are not recognized by the image analysis program as described in Section 4.2.3. While

these pillars are counted in the total number of moving pillars in Figure 4.14**b**, there are no amplitude values that can be added in the frequency responses. This leads to a cutoff at high amplitudes. The exact cutoff amplitude also depends on the amplitude of the surrounding pillars. Nevertheless, the peaks' evolution as described above can be clearly distinguished.

The same modes as before can also be identified in the sum over all squared amplitudes per frequency shown in Figure 4.14**d**. This quantity is proportional to the energy of the system and shows clearly separated modes with especially high energy around 1.35 MHz. As before, the peaks are well separated and a large number of pillars contribute especially to the largest peaks. Again, this suggests the assignment of each of the peaks to separate collective modes.

If we consider the the tight-binding model describing such an array, one would expect a large number of collective modes. In a coupled 20×20 array with 2 inherent modes per pillar one should observe 800 coupled modes. However, the observed number of collective modes here is considerably smaller. This can be explained by the overlap of the modes with the drive field. The overlap of the drive field with the eigenmodes of the system determine the steady state solution. This overlap is maximum for eigenmodes that are close to the Γ-point of the bandstructure. Typically for coupled nanopillars the eigenmodes at the Γ-point are the ones at the lower end of the eigenmode spectrum. Depending on the drive strength only very few modes at the lower end of the eigenmode spectrum are effectively driven in this scheme.

Now, we have a closer look at specific peaks in Figure 4.15. All modes above 1.4 MHz show patterns where mainly pillars towards the edges are vibrating. All modes below 1.4 MHz show central pillars vibrating. This separation between edge modes and central modes agrees very well with the results from Section 4.3, where a frequency gradient due to the diffusion limited etch process was observed even for the case of the simple rectangular bounding wall.

We concentrate on the central pillar modes and thus, on the sweep from 1.28 MHz to 1.40 MHz. Exemplary images at selected frequencies show the vibration patterns evolving during the frequency sweep in Figure 4.15. The patterns show a large number of vibrating pillars which are mostly located close together. For each of the central peaks three images are taken from the sweep to indicate the pattern evolution during the frequency sweep (cf. Figure 4.15**b-d**). They show that all involved pillars reach their maximum amplitude in the center of the respective peak, indicating simultaneous frequency evolution. These are again clear signs of collective dynamics in the array.

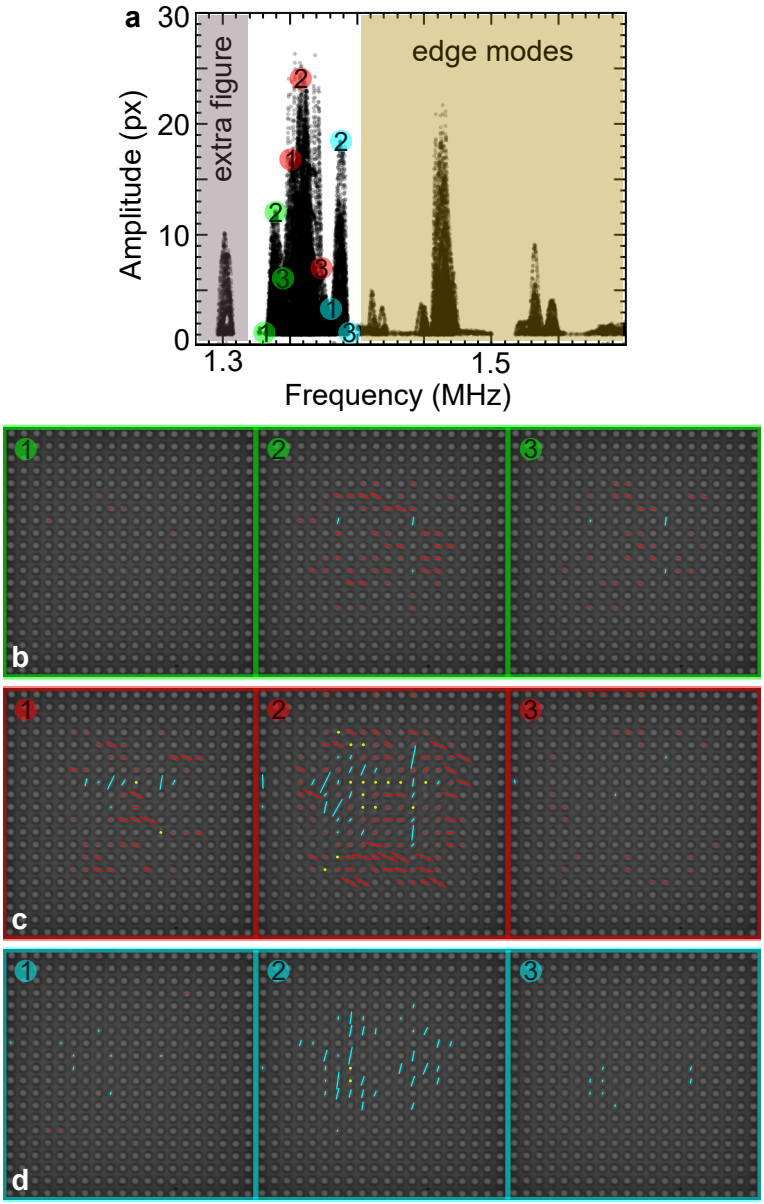

Figure 4.15: **Vibration pattern of single peaks. a**, Overlay of the frequency response of each pillar in the array. Vibration patterns of drive frequency values labeled by numbers can be found in **b** (green), **c** (red) & **d** (cyan).

Now, we have a closer look on the dynamics in each of the single peaks. As introduced in Section 4.2.3, linear motion with a roughly horizontal movement is marked in red, vertical motion is marked in cyan. We analyze the patterns as we follow the spectrum from lower to higher frequencies. At rather low frequencies, the vibration patterns show predominantly horizontal linear motion (cf. Figure 4.15**b**). Moving along the sweep from low to high frequency, the modes evolve from horizontal motion patterns to mixed

patterns (cf. Figure 4.15**c**) when more and more vertical vibrations come into play. The frequency sweep ends with modes predominantly consisting of vertical pillar motions (cf. Figure 4.15**d**). This clearly indicates a systematic anisotropy in the array despite the optimizations in the fabrication, which can only be controlled down to a certain random level.

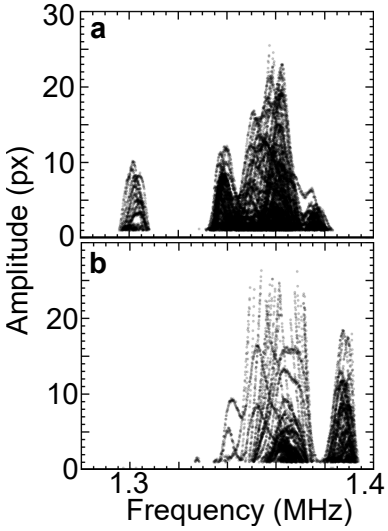

Figure 4.16: **Direction resolved frequency responses. a**, Overlay of the frequency response for roughly horizontally vibrating pillars. **b**, Overlay of the frequency response of roughly vertically moving pillars.

This anisotropy becomes even more obvious, when considering the overlaid frequency responses of vertical and horizontal pillar motions separately in Figure 4.16. While the responses of the horizontal modes (Figure 4.16**a**) show much more non-zero data points on the left side of the spectrum, the vertical modes' responses (Figure 4.16**b**) dominate at higher frequencies while there is a region with overlapping horizontal and vertical motion in the center.

Ultimately, a closer look is taken at the peak at the lower end of the spectrum highlighted in Figure 4.17**a** with a zoom on a central area of the array marked in Figure 4.17**b**. Then, a fine resolved sweep across the leftmost peak in the spectrum is displayed in Figure 4.17**c** with a zoom on the region where pillars are moving. As before, mostly spatially close pillars are found to couple in a single mode. This can be addressed to the decrease of the coupling with larger distance as shown in Section 3.3.3. The high frequency resolution of this sweep allows for the observation that the amplitudes of all pillars peak around the same drive frequency indicating a simultaneous amplitude evolution.

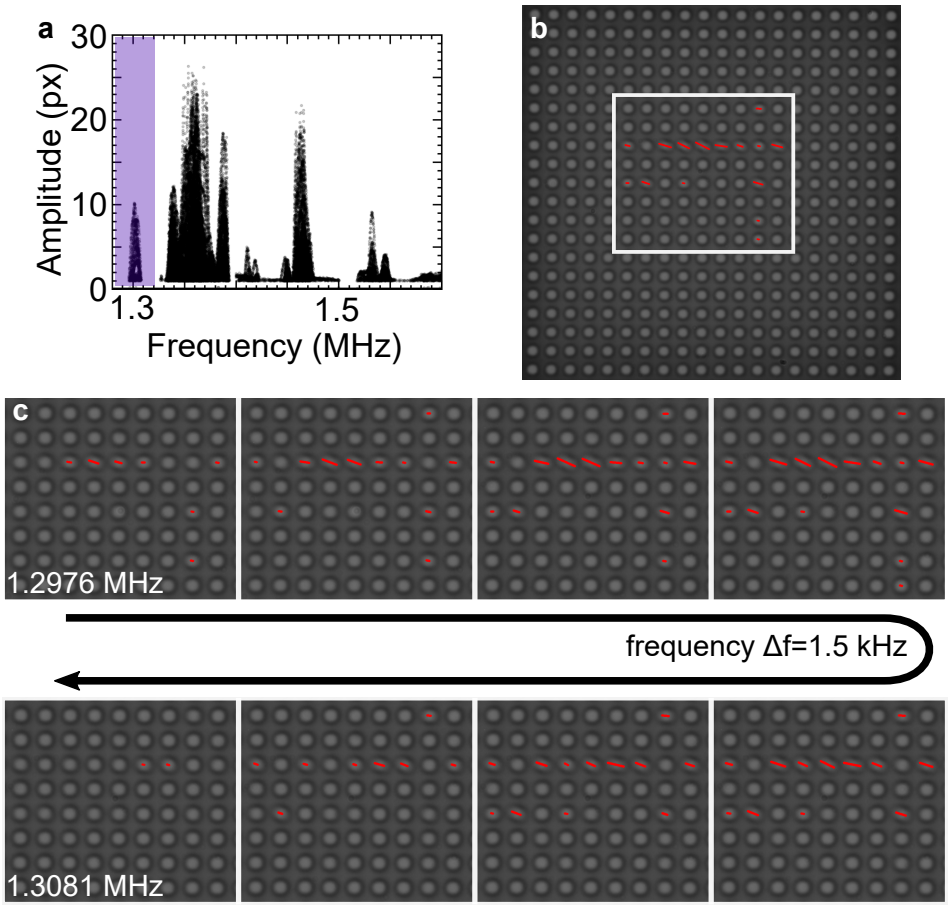

Figure 4.17: **Vibration patterns in a sweep.** **a**, Overlay of the frequency response for all pillars. **b**, Image of the whole array for $f_{\text{drive}} = 1.3021\,\text{MHz}$. **c**, Vibration patterns of zoom region from **b** across the peak marked in purple in **a**. The frequency increases along the arrow. Start and end frequencies are stated in the corresponding panels and all images in between are taken at equal frequency steps of 1.5 kHz.

The simultaneous amplitude evolution with increasing frequency as well as the formation of collective modes in spatially close pillars can be observed with even higher frequency resolution in the attached Movie M3 (see attached USB stick).

Thus, the measurements show strong indication of collective motion in an array of nanomechanical pillars.

To confirm these findings, a second pillar array is investigated. It is a 20×20 square array with lattice constant $d = 1.4\,\mu\text{m}$ and without a surrounding wall. The pillars are $r \approx 150\,\text{nm}$ in foot radius and $H \approx 6.5\,\mu\text{m}$ in height and they have a taper angle of $\varphi \approx 1.5°$. Due to a large contrast gradient towards the edges the two outmost pillar

lines have been omitted in the evaluation.

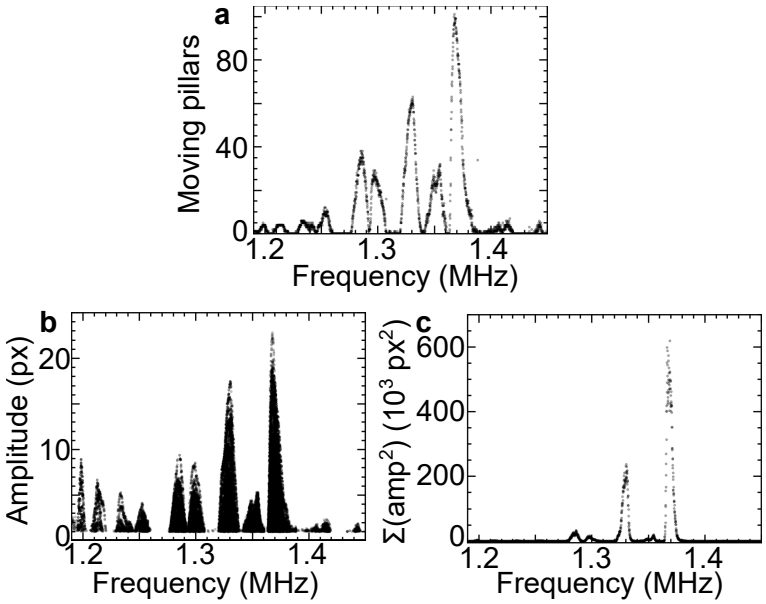

Figure 4.18: **Overview over a second coupled pillar array. a**, Histogram of the pillar array, counting the number of moving pillars for each frequency. **b**, Overlay of the frequency response of each pillar in the array. **c**, Sum over all squared pillar amplitudes for each frequency.

Again, an overview of the response of the array is provided by a histogram counting the number of moving pillars as well as frequency responses and the sum of the squared amplitudes in Figure 4.18. As on the previous sample, a number of clearly distinguished modes can be identified. In some of the modes a large number of pillars is involved.
A typical vibration pattern of each peak is shown in Figure 4.19. The peaks to the left and right side of the spectrum are rather small and only a few pillars are vibrating. The peaks 5 through 10 show vibrations of a large number of pillars mostly in the center of the array, but not limited to it. The pillars often vibrate in small groups but are spread over the whole array even within a single mode. These are again signs of collective dynamics in the presence of some disorder.

The distinction of horizontal and vertical pillars is color coded as before. However, the array shows a large mix of vibration directions and thus, the meaning of the colors is limited. For example, some pillars show red amplitudes in both of their orthogonal eigenstates, as they are vibrating in a 45° angle. Such amplitudes can also jump between the two colors from frequency to frequency due to small fluctuations. Nonetheless, the color coding is still used as it provides distinction of the vibration direction to some extent

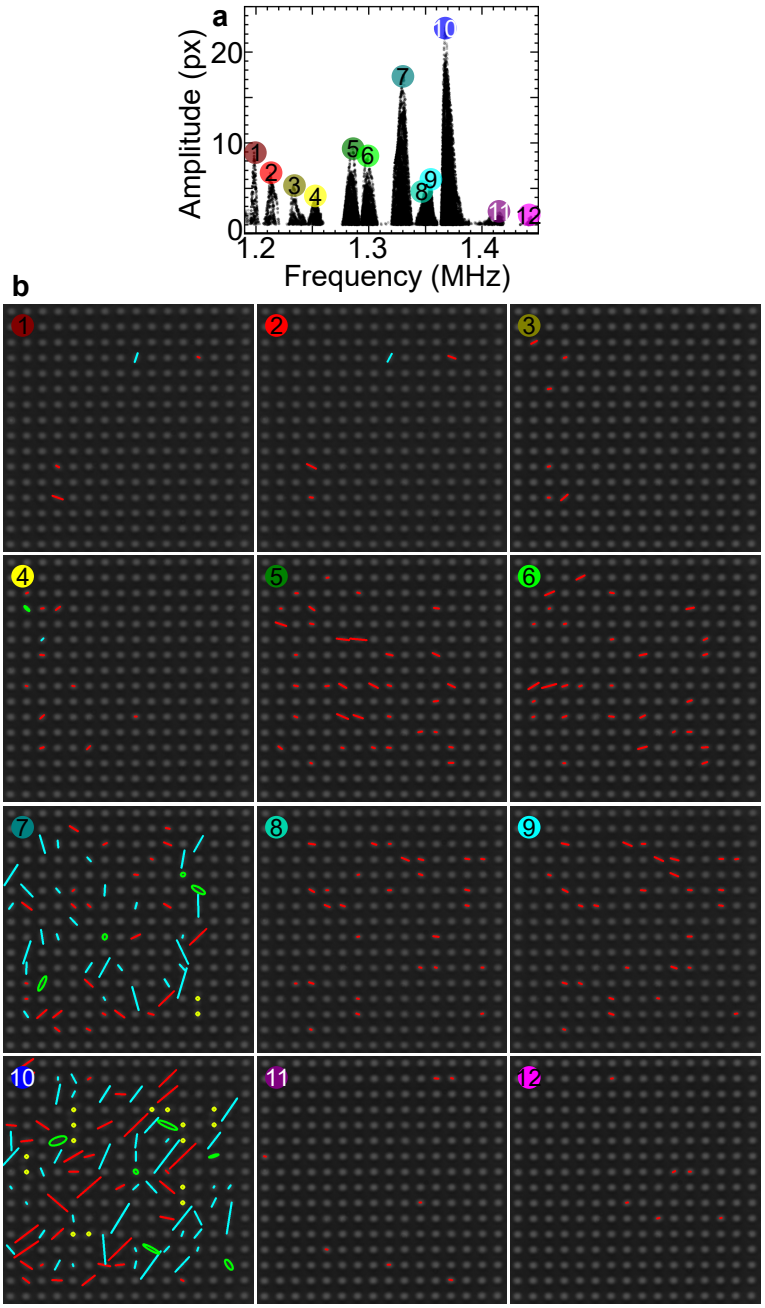

Figure 4.19: **Vibration pattern of single peaks in the second array.** **a**, Overlay of the frequency response of each pillar in the array with peaks labeled. **b**, Vibration patterns of drive frequencies labeled by numbers in **a**.

Contrary to the previous sample, the array response is not limited to horizontal and vertical vibrations only. The pillars in the second array show a large variety of vibration directions.

Especially in peaks 7 and 10 there is no clear preferred vibration direction, but the pillars vibrate in many different directions. This can be seen even more clearly by the comparison of the overlaid frequency responses of vibrations that are more inclined towards the horizontal axis and the ones towards the vertical axis (cf. Figure 4.20). Though there are few peaks with only approximately horizontal vibration directions, all peaks in the overlay of frequency responses of vertical motion coincide with a peak in the horizontal amplitude graph.

Additionally to an increased variety of vibration directions, even elliptical motion (green) can be identified. This suggests, that the asymmetry in the pillars is much smaller than for the previous sample. Elliptical motion patterns prove, that there is an overlap of the two orthogonal frequencies in some pillars.

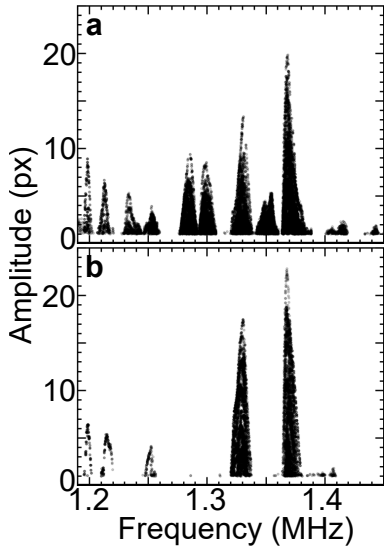

Figure 4.20: **Direction resolved frequency responses for the second array. a**, Overlay of the frequency response for roughly horizontally vibrating pillars. **b**, Overlay of the frequency responses of roughly vertically moving pillars.

The origin of elliptical pillar motion is investigated in Figure 4.21. There, peak 7 is more closely inspected (cf. Figure 4.21**a**). We focus on the pillar in the center of the zoom region marked in Figure 4.21**b**. The sweep across the peak is displayed in Figure 4.21**c**. On the left flank of the peak, the pillar shows a linear vibration roughly along the horizontal direction (red). Increasing the frequency, the linear motion continuously transforms into an elliptical trajectory (green). At first, the ellipse is very flat and with the major axis along the previous vibration direction. The ellipse then broadens and the minor and major axis become equal. Continuing along the sweep, the ellipse narrows again, but now the major axis is oriented orthogonal to the original vibration direction,

roughly vertical. At the right flank of the peak the pillar vibration transforms again into a linear one which is oriented vertically (cyan).

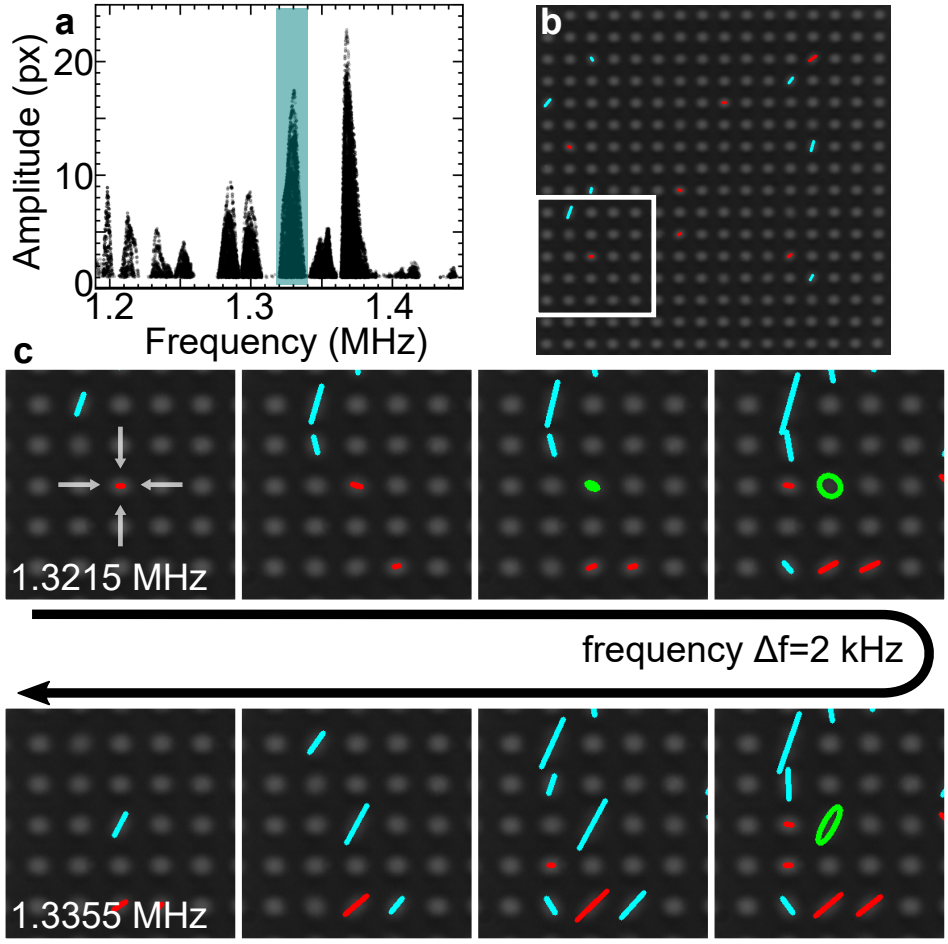

Figure 4.21: **Zoom on frequency sweep across peak 7.** **a**, Overlay of the frequency response for all pillars with the sweep region marked in turquoise. **b**, Image of the whole array with the zoom region marked by a rectangle. **c**, Vibration patterns of zoom region from **b** across the peak marked in **a**. The considered pillar is marked by arrows in the first sweep image. The frequency increases along the arrow. Start and end frequencies are stated in the corresponding panels and all images in between are taken at equal frequency steps of 2 kHz.

To explain this behavior, the amplitude spectrum has to be considered. If the two orthogonal modes of a pillar lie close together, depending on the linewidth, the two modes can overlap to some extent. This means, if one sweeps the frequency, the vibration continuously transforms from one linear vibration direction to the one orthogonal to it. To achieve a continuous transformation, the trajectory transitions through an elliptical

vibration pattern.

With this in mind, we can have a closer look on the whole array again. Figure 4.22 shows a sweep across peak 10 (cf. Figure 4.19). As for the previous sample, the amplitudes of the pillars evolve simultaneously, so that the largest number of pillars vibrate with their maximum amplitude reached roughly at the center of the peak. Again, this is a strong indication of a coupled mode. Further, one finds a vibration pattern, that consists of linear motion at very different angles. Approximately horizontal and vertical vibrations contribute almost equally (cf. Figure 4.20) to the collective mode. Several elliptical trajectories can be found as well.

All of these signatures can also be observed in a fine resolved frequency sweep of the array shown in Movie M4 (see attached USB stick).

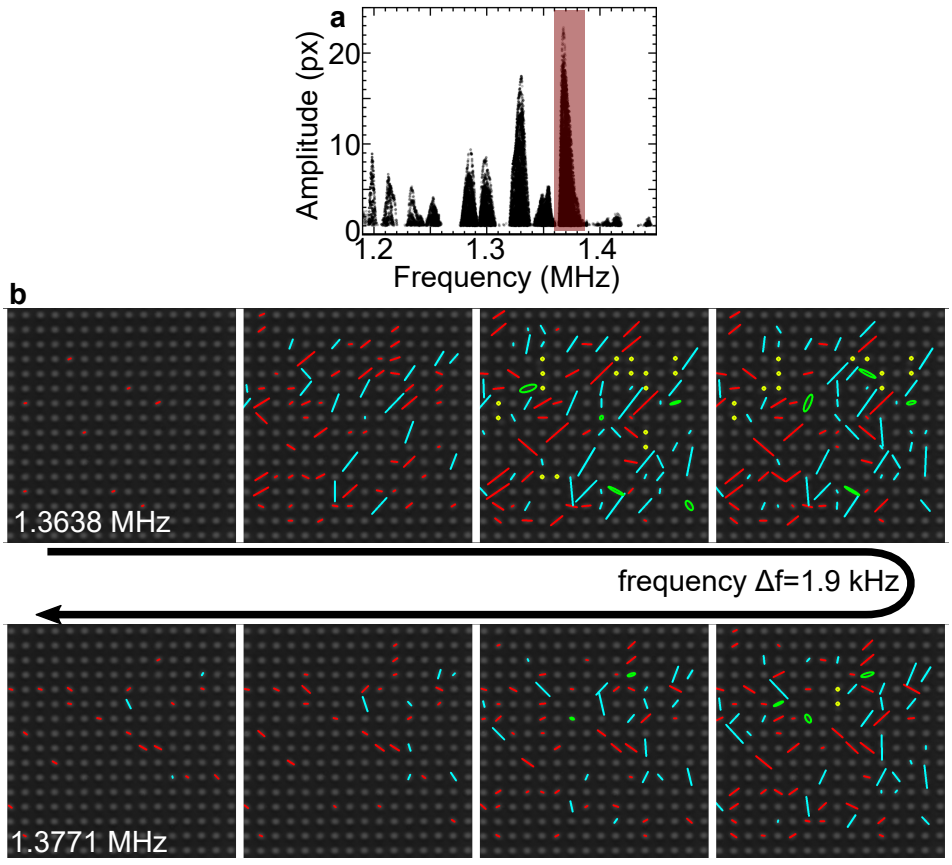

Figure 4.22: **Frequency sweep across peak 10. a**, Overlay of the frequency response for all pillars with the sweep region marked in dark red. **b**, Vibration patterns of a frequency sweep with increasing frequency along the arrow. Start and end frequencies are stated in the corresponding panels and all images are taken at equal frequency steps of 1.9 kHz.

Thus, this array already shows some of the characteristics of the simulations based on the theoretical tight-binding model from Section 4.1. Although, we have no means of measuring all involved experimental parameters, for a comparison the parameters are roughly estimated based on the experimental studies of previous chapters.

The asymmetry between the two eigenmodes is estimated to be $1\,\%$ based on SEM measurements of the pillar heads' geometry, from which the frequency anisotropy can be calculated with the single pillar theory (cf. Section 2.1.1). The two eigenfrequencies are set to $\omega_x = 1.35\,\mathrm{MHz}$ and $\omega_y = 1.3635\,\mathrm{MHz}$, reflecting the $1\,\%$ asymmetry. An order of magnitude estimation for the coupling is based on the findings in Chapter 3. By using the known distance and pillar geometry parameters, transversal-transversal coupling $J_{\mathrm{tt}} = 10\,\mathrm{kHz}$ can be estimated. A relative estimation of the other coupling parameters are based on previous insights from simulations, e.g. it is assumed that $J_{\mathrm{ll}} \approx J_{\mathrm{tt}}$, because of the ridge, that can also be found between nearest neighbors of the square lattice. Due to the coupling dependence on the separation and lack of a ridge to the next nearest neighbors diagonal couplings are estimated to $J_{\mathrm{d,ll}} = 5\,\mathrm{kHz}$ and $J_{\mathrm{d,tt}} = 2.5\,\mathrm{kHz}$. According to Section 4.3 and Section 2.4 the disorder in the center of the array can generally be estimated to *disorder* $= 2$. The linewidth of the peaks is estimated to $\Gamma \approx 6\,\mathrm{kHz}$.

Figure 4.23 shows the simulation results of the described array for two exemplary excitation frequencies at different points of the spectrum.

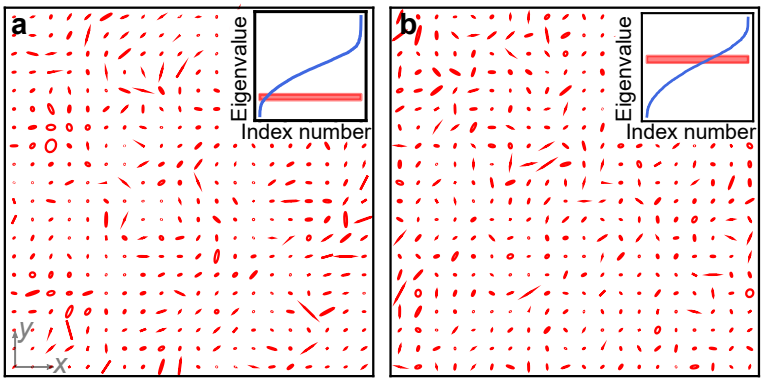

Figure 4.23: **Tight-binding simulation for the second array.** Vibration pattern of a pillar array for an excitation frequency of **a** $\Omega_{\mathrm{exc}} = 1.30\,\mathrm{MHz}$ and **b** $\Omega_{\mathrm{exc}} = 1.37\,\mathrm{MHz}$. Insets show the overlap of the drive (red) with the array eigenvalues (blue).

The simulation results reveal rather localized vibrations of coupled nanopillars in close proximity of one another. This is similar to the measured vibration patterns. Further the simulations show a mix of different vibration directions as well as elliptical trajectories which can also be found in the measured array. These different trajectories exhibit rather

sharp spatial variations from one pillar to its neighbors. This is also the case in the measured vibration patterns and is probably caused by the disorder in the array. Overall the general characteristics of the simulated and measured array are very similar.

As the overlap of the drive with the eigenmodes should only allow access to modes of the lower end of the spectrum, the vibration pattern in Figure 4.23**a** should be closer to the measurements. Nevertheless, both examples are shown for comparison and found to not differ qualitatively.

To conclude this section, I have demonstrated collective dynamics in strain-coupled nanomechanical pillar arrays. The observed dynamics agree qualitatively with the introduced theoretical tight-binding model. Yet, more profound analysis of the data and the theory is needed to complement the picture. Nonetheless, the measured arrays show clear signs of collective dynamics. Furthermore, in the second array even an interplay of the two orthogonal modes has been seen. This doubles the number of interacting modes and allows access to an additional degree of freedom lying in the two orthogonal spatial directions in which the pillars vibrate. The appearance of elliptical trajectories to the well-known linear ones resembles the predicted appearance of topological C points and L lines in two dimensional arrays with two polarizations[58] and needs further investigation.

CHAPTER 5

CONCLUSION & OUTLOOK

In this thesis, nanomechanical pillar resonators and their collective dynamics are investigated. Intrinsic coupling between two neighboring nanopillars is demonstrated and employed for the investigation of collective dynamics in nanopillar arrays.

The foundation is laid by a detailed understanding of the single nanopillar's dynamics. A theoretical model based on Euler-Bernoulli theory and already investigated in previous works[24] is complemented by finite element simulations. Contrary to the theoretical model, in the simulation model, subtle geometrical characteristics can be incorporated. Here, I implement an advanced clamping point architecture to account for the smooth transition from the pillar structure to the substrate. A comparison of theory and simulation shows very good agreement. The fabrication of nanopillars is optimized with respect to the circular symmetry of their cross-section. This decreases the asymmetry of the two orthogonal modes of a nanopillar, which can be rather large as demonstrated in statistical measurements. Further statistical analysis of pillar eigenmodes in loose groups shows, that there is a frequency gradient in groups of pillars which are as far as 10 µm apart from each other. Due to a diffusion limited etch process, the etch rate changes in the center of a pillar group compared to the edges, which yields a gradient in pillar height. This in turn is responsible for the frequency gradient in pillar groups. To overcome such fabrication fluctuations between pillars, a frequency tuning mechanism is established. A red laser spot focused on a single pillar is partially absorbed and heats up the nanopillar. A change of temperature affects the elastic properties of the material and thus, the eigenfrequency decreases. This laser-induced frequency tuning mechanism works reversibly in a range of about 0.3 % of the frequency and can be reproduced in simulations. Further irreversible frequency change can be achieved at very high laser powers, that induce temperatures at which the nanopillar starts melting.

The coupling mechanism between neighboring pillars is explored in pairs of nanopillars. The simulation of nanopillar pairs is supplemented by a ridge between the two pillars, which arises in the fabrication because of the diffusion limited etch process. The ridge causes a frequency splitting which can also be found in measured pairs. The coupling rate in simulations is found by simulating an avoided level crossing sweeping the Young's modulus, which simulates laser-induced frequency tuning.

Pairs of nanopillars are measured in the SEM, where pillar vibrations can be imaged. With this technique, it is demonstrated, that pillar pairs show mode hybridization. A frequency sweep reveals, that the amplitudes of the two neighboring pillars evolve simultaneously despite the eigenfrequencies being well separated, which is signature of a hybridized mode. Moreover, pillar pairs are investigated under laser-induced tuning. This enables the revelation of avoided level crossings between flexural modes of neighboring nanopillars. These avoided level crossings provide further evidence of strong coupling between neighboring nanomechanical pillars. Furthermore, the measured avoided level crossings are used to determine the coupling rate for several different pillar pair geometries. Under comparison to simulation results, the geometry dependent measurements reveal a clear drop of the coupling rate with inter-pillar distance. This observation confirms, that coupling is mediated via strain in the substrate. An increase of the coupling rate with increasing radius as well as decreasing height is also indicated. Although simulations suggest a dependence of the coupling on the orientation angle of the pair on the substrate, no evidence for that is found. Due to a high geometrical asymmetry the pillars always vibrate along the main crystal directions which could be responsible for the deviation of simulation and measurements.

Arrays of nanopillars can theoretically be described by a tight-binding model which has been developed in collaboration with Tirth Shah, Thomas Fösel and Florian Marquardt from the Max-Planck Institute for the Science of Light in Erlangen. Based on experimental experiences, the model also allows the incorporation of frequency disorder within the array and frequency asymmetry within every single pillar. For the characterization of arrays a different measurement method is employed. The driven pillars are imaged from the top. The imaging setup provides a good resolution as well as large field of view. An image analysis algorithm allows for the automatized analysis of a large number of images taken during a frequency sweep. In the following, different array layouts are developed to overcome the frequency gradient induced by the diffusion limited etch process. One design in particular allows a strong reduction of the frequency gradient to an almost homogeneous array. Further optimization promises a complete elimination of the frequency gradient.

With that, collective modes in nanomechanical pillar arrays are revealed. Signatures of collective modes are the simultaneous amplitude evolution of a large number of spatially close pillars. These signatures are shown for two particular arrays. While the first array shows collective modes with both mode polarizations separated, in the second array, the overlap of the two orthogonal modes of a pillar leads to more complex mode shapes.

This gives rise to elliptical trajectories, that can be found among the usually linear ones. The coupling of these modes leads to rather complex collective mode patterns distantly resembling patterns of topological polarization singularities. [58]

With these findings, the field of possible research topics based on nanomechanical pillar resonators increases even further. But before we come to the possibilities, research on collective dynamics of pillars offers, we need to revisit single pillars, since they still provide a broad band of interesting topics. This starts with two particular proposals in on-going collaborations.

In a collaboration with Guillermo Villanueva of the École Polytechnique Fédérale de Lausanne, the fabrication of silicon nanopillars is explored beyond our local attempts. Not only would silicon nanopillars allow for a comparison between the two material systems with different elastic properties, it would also benefit especially biological applications, [23] since silicon is not poisonous to most cells contrary to GaAs. Eventually, investigations on collective dynamics with silicon pillars can be performed supplementary to the ones presented here.

In a second collaboration with Mike Hettich from the Research Center for Non-Destructive Testing GmbH in Linz the anomalous Young's modulus inside GaAs nanopillars [24] is investigated. Time-resolved femtosecond pump-probe spectroscopy allows for the excitation and detection of elastic pulses along the z-axis of individual pillars. By a fixed offset of the lasers repetition rates, the asynchronous optical sampling (ASOPS) technique [59] enables a fast sweep over the time measurement window without a mechanical delay stage. The portion of the optical probe pulses reflected off the static pillar interfaces and the propagating acoustic pulse inside the pillar interfere similar to the ones in a Fabry-Perot cavity with varying thickness. Since the propagation of these acoustic pulses along the pillar depends on the sound velocity at which the pulse propagates, information about the elastic properties of the material can be deduced. Thus, the elastic properties of nanopillars can be resolved spatially along its height. Preliminary measurements by Paul Stritt and Mike Hettich show a proof-of-principle for using the picosecond ultrasonics technique on nanopillars. [60]

A single pillar can now be equipped with an additional degree of freedom such as a quantum dot, [26,31] a surface acoustic wave, [30] a confined electromagnetic mode [29] or a spin [32] to form a hybridized system with the mechanical mode. The straightforward integration of such hybrid pillars into coupled arrays, can significantly boost the functionality of the system. [61,62]

However, even without an additional functionality beyond the mechanical degree of freedom, the coupled nanopillar array offers a large number of open research paths. Additional optimizations can further improve the existing array schemes. The optimization of the wall layouts, especially the distance of the wall to the array, could lead to a much

more homogeneous frequency distribution in the array. Thus, all the extra modes appearing in the array (cf. Figure 4.14) due to the frequency gradient could be eliminated. A further homogenization of the frequencies in an array can be achieved by laser-induced frequency tuning in a pillar array via a spatial light modulator.
So far, we have not exploited the full potential of the vacuum chamber. The chamber allows to adjust the atmosphere surrounding the pillars, i.e. pressure or even gas composition. This would directly affect the linewidth through a changed damping. As the appearance of elliptical pillar trajectories depends on the asymmetry but also on the linewidth, the atmosphere control in the chamber would allow to directly influence the mode overlap.
Such further investigations on the pillar array dynamics, could close the gap between experimental data and theoretical description. This could eventually allow for the identification of topological C points and L lines in a pillar array.[58]
The range of accessible collective modes could then even be expanded by employing a new driving scheme. So far, we have only been able to drive all pillars in an array simultaneously by the shear piezo. In the past, this type of drive scheme has also shown large phase lags between different resonators across a sample.[63] Although we do not directly observe this an effect, a different drive scheme could allow to exclude such an influence of the drive on the observed collective modes. In the Master's thesis by Milan Jubitz,[64] we have shown that a dielectric drive scheme can effectively excite a single nanopillar. A system of four electrode tips placed around a nanopillar can be asymmetrically connected to create a large electric field gradient. In a future project the investigation of such a driving mechanism in an array could allow to drive only a single pillar or a small subgroup of pillars in the array, contrary to the shear piezo drive where all pillars are excited equally. This could eventually allow access to different collective modes that overlap with the different drive scheme.

These optimizations eventually allow for the investigation of nanomechanical metamaterials,[8,15,20,21] topological effects[7,14,15] or synchronization phenomena[4,12,13,65] in intrinsically coupled nanomechanical pillar arrays.

Appendices

APPENDIX A

FABRICATION

Additionally, to the optimized main fabrication process (cf. Section 2.2), other approaches have been investigated during the course of this work. This chapter will give an overview of these methods and their results.

A.1 Fabrication batches

The fabrication of the nanopillars for this work, including the etch runs in the clean room of the *LMU Munich*, was done in two major fabrication cycles. As the optimization of the fabrication process, especially the preparation of the etch mask, was done in between these two cycles, the nanopillars of the two batches show slightly different characteristics. The two batches are referred to as *batch 2017* and *batch 2019*. *batch 2019* has been fabricated according to the final optimized process described in Section 2.2. The differences of *batch 2017* to the optimized process are described in the following.

A.1.1 Batch 2017

The basic structure of the fabrication process used in 2017 is the same as for the optimized fabrication process, which has been developed later. However, especially for the etch mask fabrication a few changes have been made to optimize the isotropy of the two fundamental resonance frequencies (see Section 2.2). Additionally, the etch run itself has an unexpected impact on this specific batch, which in turn led to a deeper understanding of the etch run and precautions for the seasoning in future runs.

Contrary to the optimized process, here, *Poly methyl methacrylate (PMMA) 950k A4* was used as an electron beam resist and lithography is done with a 30 µm aperture. 5 kV

EHT as well as working distance and area dose are unchanged. Especially, the larger aperture has an impact on the circularity of the nanopillar cross-section as shown in Figure 2.6 in the main part. Hence, all nanopillars from *batch 2017* show a rather large anisotropy for the two fundamental flexural modes.

For the subsequent etch mask evaporation, 100 nm nickel ($1\,\text{Å}\,\text{s}^{-1}$ evaporation rate) is used instead of SiO_2. As for the etch selectivity as well as the pillar dynamics, there is no notable impact of the usage of a nickel etch mask versus a SiO_2 etch mask.

The etch parameters for this particular batch can be found in Table A.1. Although some parameters are different than the ones mentioned in Table 2.2, the etch results should in general not be different as has been found in previous works.[36–38]

parameter	setting
$SiCl_4$ flow	13 sccm
N_2 flow	0.1 sccm to 0.2 sccm
RF power	65 W
ICP power	50 W
pressure	2 mTorr
helium flow	5 Torr

Table A.1: **Etch parameters *batch 2017*.** Etch parameters for the chlorine-based anisotropic ICP reactive ion etch as used for *batch 2017*.

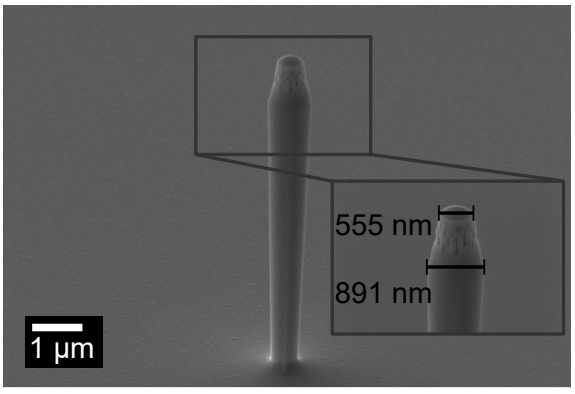

Figure A.1: **Typical nanopillar from *batch 2017*.** Micrograph of a typical nanopillar from *batch 2017*. Close up on the nanopillar head, with measured diameter 555 nm at the top and 891 nm at the broadest part.

However, in this particular batch, the dynamics of the nanopillars is rather unusual, such that it neither fits theory (Section 2.1.1) nor simulation (Section 2.1.2). The origin of

the deviation from theoretical descriptions can be found, when studying the nanopillars in a electron microscope. Figure A.1 shows the electron micrograph of a nanopillar from *batch 2017*.

Considering the head of the nanopillar, one finds a rather slim top cross-section. When moving towards the clamping point, the cross-section increases at first till a maximum radius and then decreases with the known negative taper. A measurement shows, that the radius at the top is with 278 nm rather close to the nominal value 300 nm. The maximum radius for this pillar 446 nm is far beyond the nominal radius, which was lithographically defined. It has been seen, that the etch mask alone does not increase the radius beyond its nominal value significantly. This indicates, that the etch process increases the radius beyond the defined radius by adding a rather thick passivation layer. An energy dispersive X-ray spectroscopy (EDX) measurement reveals traces of silicon and oxygen on the pillar wall, additionally to the expected gallium and arsenic. This fits well to previous findings[39] with the difference of the passivation layer being rather thick. Closer investigations reveal, that the thickness of the passivation layer varies: For pillars etched later in the cycle the passivation layer thins down to a few nanometers.

This leads to the conclusion, that a long seasoning of the etch process is necessary to achieve good stability with regards to thin passivation walls.
To conclude the remarks on *batch 2017*, we find a large frequency anisotropy within each pillar, caused by the non-optimized lithography. Since in *batch 2017* mostly pairs are fabricated, this effect is overlaid with the anisotropy caused by the diffusion limited etch in a group (cf. Section 2.4). Furthermore, the theory and simulation based frequency calculation does quantitatively not hold for this batch due to a big influence on the frequency of the rather thick passivation layer. However, qualitative predictions are still possible.

A.2 Negative resist

For the optimization of the etch mask, a negative resist was tested as an option to the *PMMA* positive resist, but discarded after rather poor results. The negative resist *ma-N 2403* is tested as an etch mask for the preceding fluorine etch which reveals the SiO_2 mask for the proceeding chlorine etch (cf. Section 2.2).

Here, a brief overview is given on the limits of the *ma-N 2403* negative resist for the nanopillar fabrication.

Lithography is done with the same main parameters and adapted area dose. The results after development are shown in Figure A.2**a**. To compensate the roughness of the edges, a resist reflow was performed on the *ma-N 2403* mask, where the sample is heated to

145° for 5 min (cf. Figure A.2**b**). The surface of the resist structures is minimized when heating the resist above post-bake temperature. This should result in a more circular shape and smoother edges.

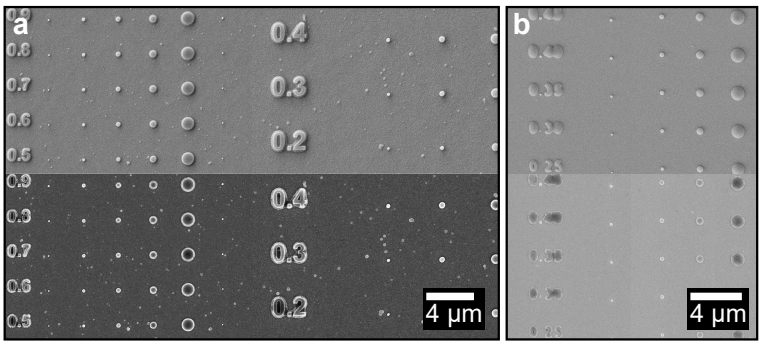

Figure A.2: ***ma-N 2403* etch mask. a**, *ma-N 2403* after development for different area doses indicated on the left on each row. **b**, *ma-N 2403* after resist reflow for different area doses indicated on the left of each row. Upper (lower) panels show images of the secondary electron (in-lens) detector.

The resist reflow reveals good results with regards to the smoothness and circularity. However, the images suggest a curved profile of the resist structures. This could lead to an inhomogenous mask stability.

Independent of the mask shape, the selectivity of the *ma-N 2403* in the fluorine reactive ion etch is not high enough to etch through the 100 nm SiO_2 and protect the structures. Thus, this approach has not been investigated further.

A.3 Nickel etch mask

Both, nickel and SiO_2 have sucessfully been used as etch mask in the clorine-based anisotropic etch of GaAs for the fabrication of nanopillars. While nickel can successfully be used to fabricate nanomechanical pillar resonators, SiO_2 provides a few advantages over nickel for an optimized process. The selectivity of 100 nm nickel versus GaAs in the clorine-based etch is sufficient for the fabrication of nanopillars with a height of $> 10\,\mu m$ and is thus, similar to the selectivity of SiO_2. In general, the use of one or the other etch mask does not have any influence on the dynamics of a nanopillar.

However, during the etch process, the nickel on top of the nanopillars transforms into a nickel-chlorine compound as confirmed by EDX measurements. Additionally, no electrically conducting bond can be put directly on the nickel-chlorine compound. Thus, nickel should not be used on electrodes that are for example needed in dielectric control experiments. [64]

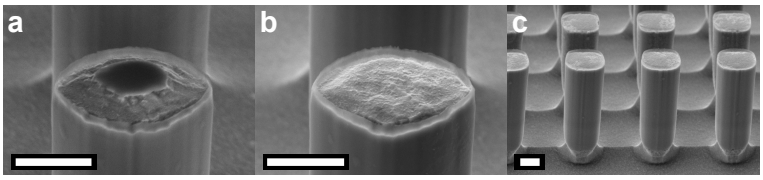

Figure A.3: **Nickel mask removal**. Close up on nanopillar with partially removed nickel mask (**a**) and fully removed nickel mask (**b**). **c**, Micrograph of entire nanopillar with removed nickel etch mask. Scale bars in **a** & **b** correspond to 200 nm, the one in **c** to 1 µm. Images are from a 60° tilted view.

The nickel-chlorine compound proved rather difficult to be removed. While it is often not necessary to remove the remains of the etch mask from the nanopillar, it can become necessary occasionally. If necessary, a 10 min dip in deionized water,[1] which first removes the nickel-chlorine compound followed by a 5 min dip in iron(III) chloride removes the etch mask completely. On the down side, it can also attack the GaAs slightly. Nanopillars with partially (**a**) and fully (**b**) removed masks are shown in Figure A.3, along with the the clamping point of these pillars, which is slightly etched (**c**).

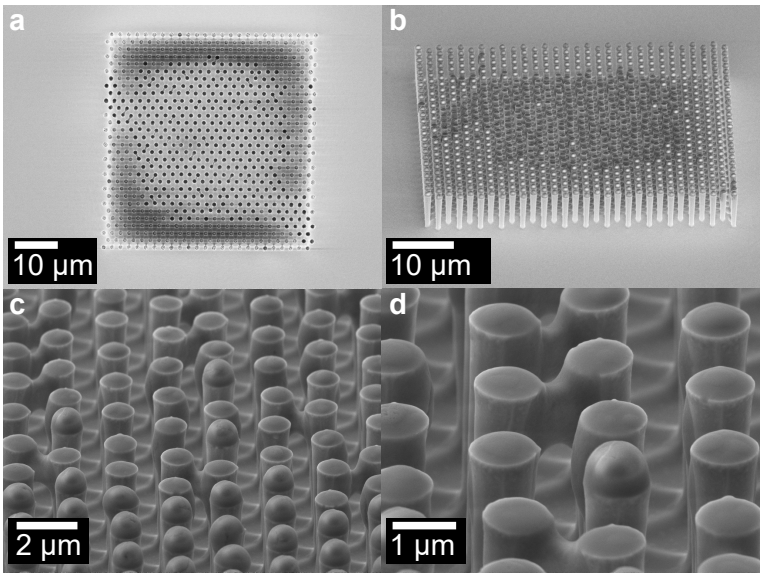

Figure A.4: **Nickel mask deformation. a-d**, Electron micrographs of nanopillars with deformed etch mask roughly one year after fabrication. **b-d** show a 60° tilted view.

In rare occasions, it can also happen, that the nickel-chlorine compound transforms its shape over time, leading to a behavior that resembles a very viscous liquid as displayed in Figure A.4.

[1] A preceding isopropanol dip ensures the water flowing in between the pillars.

To avoid all these complications the evaporation of a SiO_2 etch mask is preferred, which – apart from being stable – can easily be removed with hydrofluoric acid.

A.4 Tuning-in of the anisotropic etch process

In this section, some notes are given on the tuning-in of the anisotropic ICP reactive ion etch in the clean room at the LMU Munich.

Since the anisotropic etch process tends to become unstable with any small disturbance, some precautions are met: The respective etch machine needs to be blocked from running other processes to not change the chemical ambiance in the etch chamber. Additionally, an etch chamber dome dedicated to this particular process is installed and the whole etch chamber is physically cleaned. [36–38]

To start an etch cycle, the etching process should be running for a couple of days straight till stable results can be expected. The etch rate, taper angle and SiO_2 passivation layer thickness are parameters that indicate the stability of the etch process.

Once stable, the etching process needs to be tuned to the desired sidewall smoothness and etch rate. One should keep in mind, that every change of a parameter needs some stabilization time, especially when changing the gas flows. To tune-in all the parameters, there are several points to take into account.
Helium flow and chamber pressure were less influential in the past and are usually not changed. Thus, the parameters one needs to adjust are mainly the gas flows as well as the ICP and RF power. There are some general trends, how these parameters influence the etch. However, one has to keep in mind, that all the parameters influence each other and that there is a certain fragility of the plasma conditions.

The smoothness of the sidewalls is mainly influenced by the passivation which is adjusted by the ratio of the N_2 gas flow to the $SiCl_4$ gas flow. A higher ratio increases the passivation an thus, the smoothness of the sidewalls. At the same time it tends to decrease the taper angle, which can basically even lead to positively tapered nanopillars. Additionally, an increase of $SiCl_4$ gas flow also tends to increase the etch rate. However, there is an upper limit for the $SiCl_4$ gas flow around 14 sccm due to the low gas pressure of $SiCl_4$.
Further, the N_2 mass flow controller used was built for maximum 10 sccm and mass flow controllers are usually recommended to be used down to 5 % of the maximum flow. In case of Table 2.2 and Table A.1 the N_2 flow lies well below that limit. Higher N_2 flows or an even more sensitive mass flow controller can benefit the stability of the etching process.

RF and ICP power, both strongly influence the etch rate. Additionally, the ICP power has strong influence on the smoothness of the sidewalls. Smoother sidewalls can be achieved by using a smaller ICP power, which in turn lowers the etch rate.

Especially, with the long stabilization time one needs to plan sufficient time for an etch cycle of several weeks.

A.5 Alternative etch strategies

As an alternative to the sensitive chlorine-based etch at LMU Munich with limited access time, two strategies are employed in the Nanostructure Laboratory at the University of Konstanz. Although both strategies do not yet meet the requirements needed for a nanopillar etch, they both can built a foundation of further development of a new pillar etch recipe.

In the first approach, a chlorine-based GaAs etch is explored at the *Oxfort Plasmalab 100* at the University of Konstanz. The second approach attempts the fabrication of silicon nanopillars based on a fluorine etch process. Although GaAs has advantages over silicon such as its piezo electricity or the possibility to implant quantum dots it is potentially poisonous to most biological cells. Silicon on the other side is mostly non-poisonous and thus, brings advantages in biosensing based on nanopillars. [22,23]

A.5.1 GaAs nanopillar etching in the Nanostructure laboratory

A series of GaAs nanopillar etches with $SiCl_4$ were done in the Nanostructure laboratory at the University of Konstanz (Nanolab) during a student's project with F. Johannsen. [66]

In a first approach, an existing III-V semiconductor etch recipe developed by M. Bückle [67] is used in an attempt to etch nanopillars. The process was developed for doubly clamped string resonators on GaAs substrate. Thus, it is developed to only etch several hundred nanometer into the substrate instead of several micrometers as needed for nanopillars. The used etch parameters are shown in Table A.2

parameter	settings approach 1	settings approach 2
$SiCl_4$ flow	3 sccm	15 sccm
N_2 flow		1.5 sccm
Ar flow	9 sccm	
RF power	60 W	60 W
ICP power	250 W	250 W
pressure	2 mTorr	2 mTorr
temperature	30 °C	30 °C

Table A.2: **Etch parameters for chlorine etch in the Nanolab.** Etch parameters for the existing chlorine-based etch from M. Bückle[67] (approach 1) and for the process basing on nitrogen passivation (approach 2).

A long etch is performed and reveals very short pillars as in Figure A.5**a**. It can be seen, that the original 100 nm SiO_2 etch mask is fully etched away and leaves a crater. EDX measurements show no residual SiO_2 on the top of the pillar.
Further studies attempted to reduce the rather strong physical etch component which affects the mask almost as strongly as the substrate. However, neither tweaking the gas ratio nor the ICP or RF power within the limits of the stabilization of the process, has any significant effect on that.

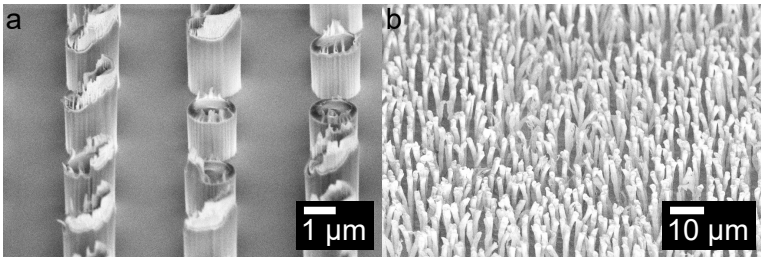

Figure A.5: **GaAs etch results in the Nanolab.** **a**, Scanning electron micrograph of the etch results from approach 1 in a 60° tilted view. **b**, Scanning electron micrograph of the etch results from approach 2 in a 60° tilted view.

In a second approach, we attempt to reestablish the process done at the LMU Munich. In the process at LMU Munich a very tiny amount of nitrogen is added to the $SiCl_4$. However, the *Oxford Plasmalab 100* in the Nanolab is not equipped with a mass flow controller of such a fine resolution and only allows a N_2 flow down to 1.3 sccm. To keep the N_2 to $SiCl_4$ ratio small despite the high N_2 flow, we attempt to increase the $SiCl_4$ flow. This flow, however, is limited[2] to roughly 15 sccm for long etch runs due to the

[2]The limit here is slightly different from the one experienced at the equipment at LMU Munich. This might be due to a heated $SiCl_4$ line in the Nanolab in Konstanz contrary to the one at LMU Munich.

rather small gas pressure of $SiCl_4$.

Nevertheless, etches with the increased ratio are implemented with parameters shown in Table A.2. The results are shown in Figure A.5**b**. Similar to the creation of black silicon (cf. Appendix A.5.2), "grass" [68–71] is formed and the GaAs substrate turns black. This indicates overpassivation as was already expected from the high N_2 to $SiCl_4$ ratio. This phenomenon is explained in more detail in the following chapter.

As the N_2 to $SiCl_4$ gas flow ratio can not be decreased, other parameters were swept, but no significant changes observed. As in the following chapter, the gas ratio is the most crucial influence on the passivation. Thus, no improvements on the results in Figure A.5**b** were observed.

Both of the mentioned approaches did not produce smooth nanopillars comparable to the ones etches at LMU Munich. However, further studies on the second approach with a more sensitive mass flow controller for the nitrogen flow can still bring GaAs nanopillars fabricated at the Nanolab in Konstanz within reach.

A.5.2 Fabrication of silicon nanopillars

Deep anisotropic silicon etches are well explored. One well-known method is the *Bosch* process, [72–74] which relies on alternating cycles of etching and passivation. This etch results in high aspect ratio structures with tiny lamellae along the etch depth due to the cycling of the process. The second method is a cryogenic fluorine-etch with oxygen passivation. [68–71] This second approach is employed here.

For tests, simple structures are fabricated by photo lithography and covered with $\approx 100\,\text{nm}$ thermally evaporated aluminum. An alternative alumina etch mask has not been stable enough for high aspect ratio pillar structures.

A cryogenic etch is performed at temperatures of $-90\,^{\circ}\text{C}$ or lower with SF_6 as etchant and additional oxygen, which leads to a passivation of the sidewalls in order to achieve high aspect ratio structures. A small amount of oil is added between the sample and the carrier wafer of the etch machine to ensure thermal contact.

A process proven to produce high aspect ratio structures in deep etches is chosen as a starting point. The corresponding parameters are shown in Table A.3. Although that process has proven to passivate the side walls efficiently for structures above the nanoscale in etches as deep as 100 nm, these results can not be reproduced for nanopillar sized structures. On a smaller scale, the etch recipe leads to roughly 1 µm of under etching from the side though with very smooth sidewalls (cf. Figure A.6**a**).

parameter	setting
SF_6 flow	100 sccm
O_2 flow	8 sccm
RF power	5 W
ICP power	1000 W
pressure	10 mTorr
temperature	−120 °C

Table A.3: **Etch parameters standard cryogenic etch.** Etch parameters for the standard cryogenic fluorine-based reactive ion etch.

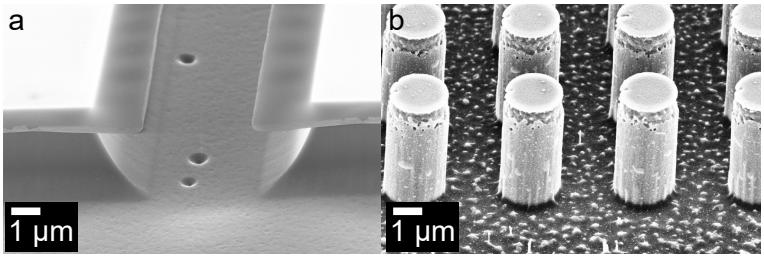

Figure A.6: **Silicon nanopillar etching. a**, Scanning electron micrograph of a structure etched with parameters given in Table A.3 imaged in a 60° tilted view. **b**, Scanning electron micrograph of a structure etched with parameters given in Table A.4 imaged in a 60° tilted view.

As for ICP reactive ion etch processes, there are many parameters to be tweaked with all of them influencing each other. Nevertheless, etch series on all different parameters have narrowed down the main influence on the etch profile by the ratio of etch and passivation gas O_2 and SF_6. A higher O_2 to SF_6 ratio increases sidewall passivation up to a positively tapered profile, while a lower relative oxygen content leads to an undercut. At some point the passivation is so high, that the sample is filled with spikes, due to over-passivation, rendering every tiny roughness into an etch mask. Because light is trapped in such a spiked surface, this is referred to as black silicon.[68,70] The optimum passivation – O_2 to SF_6 ratio – is just before the point, where over-passivation leads to black silicon.
Studies have shown, that the temperature also influences the passivation.[70,71] Since the operation of the machine at such low temperatures is rather tedious due to temperature instabilities, the temperature was kept constant after some preliminary trials. Pressure and RF power also can influence the etch profile, but have a negligible contribution compared to the influence of the gas ratio. Finally, the ICP power mostly influences the etch rate. However, it has to be high enough for the plasma to ignite. The discussed process is only stable over a long time at 1000 W. At lower powers, the plasma tends to

flicker.

The best results for silicon nanopillar etching are shown in Figure A.6**b**. The corresponding recipe is given in Table A.4.

parameter	setting
SF_6 flow	63 sccm
O_2 flow	35 sccm
RF power	25 W
ICP power	1000 W
pressure	10 mTorr
temperature	−120 °C

Table A.4: **Etch parameters improved cryogenic etch.** Etch parameters for the improved cryogenic fluorine-based reactive ion etch.

However, due to the instability of the process at such low temperatures, these results or any other etch results were not sufficiently reproducible. More results on etching nanopillars are shown in Figure A.7. The examples vary between over- and under-passivation.

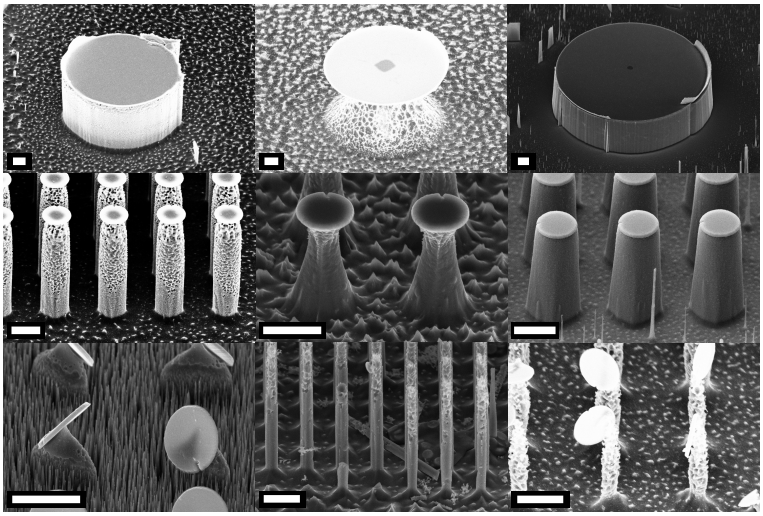

Figure A.7: **Silicon nanopillar etch series.** Examples of fluorine-based ICP reactive ion etch results for silicon nanopillars. All scale bars correspond to 2 µm.

A.6 Calibration samples

For the aforementioned seasoning of all the etch processes, a lot of samples with pillar structures are necessary. The usual fabrication by electron-beam lithography is very consuming in terms of time and resources. In order to circumvent that, samples were prepared via contact photo lithography. The mask for photo lithography consists of several millimeter wide areas with pillars with 2 µm diameter and 4 µm lattice constant.

Contact lithography of these structures proofs particularly difficult owing to the very small feature size near the resolution limit of conventional photo lithography as well as the wide area over which these structures are spread. Many photo resists have proven inefficient for a pattern of these characteristics. Some photo resists are several micrometers thick and thus, aided by a slight positive taper, are inadequate to reveal such small features. Other photo resists are so viscous, that the resist layer is very uneven and contact can not be ensured over such a large area. A gap between the resist and mask decreases the resolution. Thus, while the structures can be properly resolved in some small areas it is usually not the case over the whole range of the structures.

So far, only *AZ MIR 701 14CP*[3] proved suitable for the pattern definition of the nanopillar calibration samples. This resist has a rather small nominal thickness of 900 nm and forms a layer even enough to ensure sufficient resolution over several centimeters.
Nevertheless good contact between mask and resist as well as a slight overexposure aid the success of the pattern definition.

Although not specified for lift-off, it performs adequate lift-offs with either 100 nm evaporated Nickel or SiO_2.

These samples with large areas of pillar structures can be cleaved after preparation and thus, provide a fast and ample sample stock for calibration and seasoning of any etch process.

[3] provided by MicroChemicals GmbH

APPENDIX B

MEASUREMENT AND ANALYSIS

As an addition to Section 2.3 the detection setup for the laser-based detection scheme is depicted here in more detail.

Image based analysis relies on the approximation that the amplitude of a pillar can be reduced to a two dimensional recording from the top, neglecting the third dimension. This will be justified in the second part of this chapter.

B.1 Laser detection setup

A sketch of the full laser detection setup is shown in Figure B.1.

The 635 nm diode laser can be attenuated with a continuous neutral density filter, which controls the laser-induced tuning (cf. Section 2.5). The laser is then focused onto the sample surface via a $100\times$ microscope objective. The reflexion of the laser beam from the sample is collected in a silicon based photo detector and processed by a vector network analyzer. The network analyzer also controls the RF-input for the driving force, mediated by a piezoelectric shear transducer.

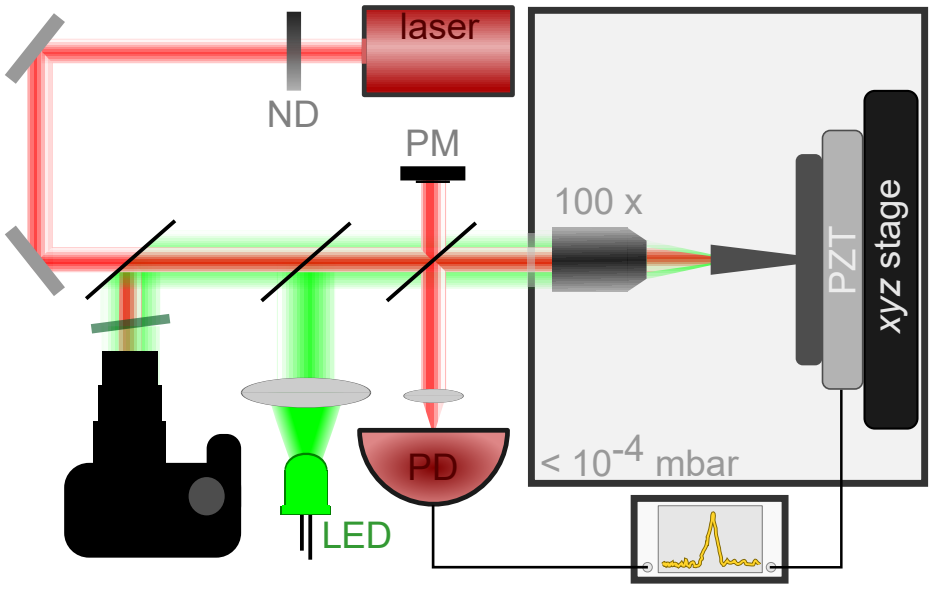

Figure B.1: **Setup for laser-based detection.** Setup for laser based detection scheme with 635 nm laser, neutral density filter (ND), $100\times$ microscope objective, photo detector (PD), power meter (PM), piezoelectric transducer (PZT), vector network analyzer, green LED, DSLR camera with preceding short pass filter at 650 nm and xyz-positioning stage. Beam splitters from left to right have a reflexion to transmission $R:T$ ratio of $8\,\%:92\,\%$, $8\,\%:92\,\%$, $50\,\%:50\,\%$.

An additionally installed imaging system, allows for the imaging of sample and laser and thus, the precise control of the laser position with respect to the sample. A green LED provides a large field illumination of the sample. Both, laser and LED reflexions passing a short pass filter at 650 nm are collected in a DSLR camera. The short pass filter is slightly rotated with respect to the beam axis which shifts the cut-off frequency slightly, so that it attenuates the high intensity laser, which could otherwise damage the camera sensor. A xyz-piezo stage carrying the sample allows for the precise positioning of a specific nanopillar in the laser spot focus.

B.2 Analysis of two dimensional images

In all imaging analysis methods, particularly in Section 3.3.1 and Section 4.2.3, the amplitude is approximated to its projection into the image plane from the top. Thus, the shortened height of a deflected pillar is not taken into account (cf. Figure B.2).

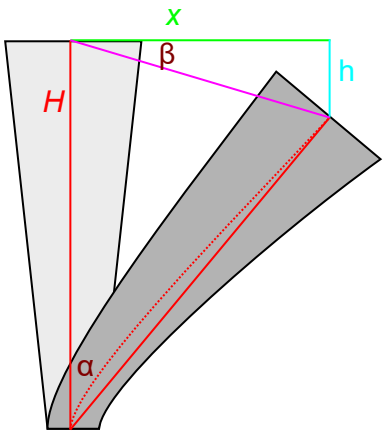

Figure B.2: **Amplitude approximation.** Sketch of a deflected and non-deflected pillar. All relevant parameters are indicated.

In an Euler-Bernoulli pillar, the neutral plane of the deflected pillar is of length H as indicated in Figure B.2 (dashed, red). For deflections x much smaller than the height H, $x \ll H$, the curvature in this plane can be neglected and approximated by a line (solid, red). The two solid red lines Figure B.2 enclose an isosceles triangle. This allows for the identification of

$$\beta = 90° - \frac{180° - \alpha}{2} = \frac{\alpha}{2}. \tag{B.1}$$

With the condition $x \ll H$ one finds

$$\frac{x}{H} = \sin\alpha \approx \alpha \ll 1. \tag{B.2}$$

This can be used to deduce

$$\begin{aligned} \frac{\alpha}{2} &\ll 1 \\ \Leftrightarrow \tan\alpha/2 &\ll 1 \\ \Leftrightarrow \frac{h}{x} &\ll 1 \\ \Leftrightarrow h &\ll x. \end{aligned} \tag{B.3}$$

Thus, the amplitude can be approximated by x in the case $x \ll H$. Due to the image analysis algorithm being limited to amplitudes $x < r$ and $r \ll H$ for all regarded pillars (also see Euler-Bernoulli conditions), $x \ll H$ follows for all pillars in this thesis.

APPENDIX C

SUPPLEMENTAL TO PAIRS OF COUPLED NANOMECHANICAL PILLAR RESONATORS

Here, additional simulations and measurements on pairs of coupled nanomechanical pillars are shown. The information is supplementary to Chapter 3.

C.1 Ridge influence on coupling strength

In Section 3.2 the details of the simulation model for a pair of nanopillars are introduced. A ridge is included as an addition to the single pillar model. The main influence of this ridge, leading to a frequency splitting is already discussed in Section 3.2. However, the detailed influence on the coupling strength is not discussed yet and will be shown here.

A comparison of the simulation with and without ridge is shown in Figure C.1. As shown, the coupling strength does not change significantly and stays in the same order of magnitude for both simulation models.

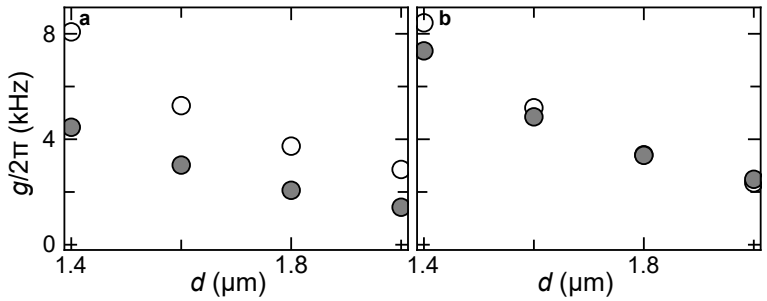

Figure C.1: **Ridge influence on coupling strength.** Coupling strength $g/2\pi$ depending on the center-to-center distance of the pillars d for in-plane (○) and out-of-plane (●) modes **a** without ridge and **b** with ridge. The image is taken from the supplementary information of Reference [45].

However, without the ridge, in-plane and out-of-plane coupling are split considerably presumably because of the difference in the strain field overlap for the two modes. Including the ridge in the simulation model almost nullifies this difference of the coupling strength for the two modes. As shown in Figure 3.4**a** the strain field for the model with ridge is mostly confined within the ridge which presumably helps to overcome the large differences between the in-plane and out-of-plane mode coupling strength.

C.2 Additional avoided level crossings

All data shown in Figure 3.12 and Figure 3.13 is extracted from avoided level crossings measured for a variety of nanopillar pairs. All of these measurements are shown in Figure C.2 with the exception of the two shown in Figure 3.9 and Figure 3.10.

The fitted coupling rates can be found in Figure 3.12 and Figure 3.13.

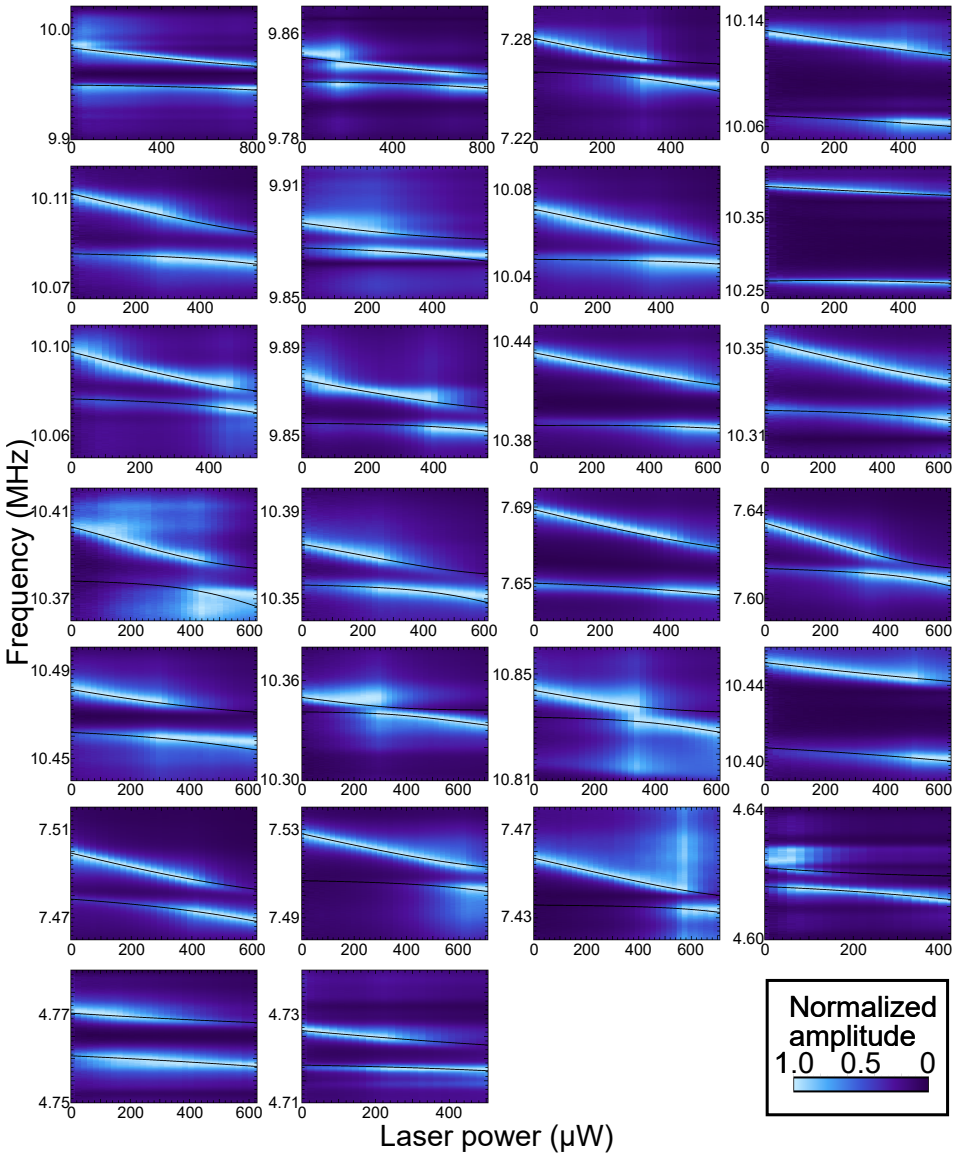

Figure C.2: **Avoided level crossings.** Frequency response with increasing laser power for various nanopillar pairs. Geometry parameters are from left to right and top to bottom: 10°: $r \approx 430\,\text{nm}$, $H \approx 7.1\,\mu\text{m}$, $d \approx 1.8\,\mu\text{m}$; $r \approx 420\,\text{nm}$, $H \approx 7.0\,\mu\text{m}$, $d \approx 2.0\,\mu\text{m}$; 15°: $r \approx 300\,\text{nm}$, $H \approx 7.0\,\mu\text{m}$, $d \approx 1.3\,\mu\text{m}$; 20°: $r \approx 430\,\text{nm}$, $H \approx 7.0\,\mu\text{m}$, $d \approx 1.3\,\mu\text{m}$; $r \approx 430\,\text{nm}$, $H \approx 7.0\,\mu\text{m}$, $d \approx 1.7\,\mu\text{m}$; $r \approx 430\,\text{nm}$, $H \approx 7.0\,\mu\text{m}$, $d \approx 1.9\,\mu\text{m}$; $r \approx 430\,\text{nm}$, $H \approx 7.0\,\mu\text{m}$, $d \approx 2.0\,\mu\text{m}$; 25°: $r \approx 420\,\text{nm}$, $H \approx 7.0\,\mu\text{m}$, $d \approx 1.2\,\mu\text{m}$; $r \approx 430\,\text{nm}$, $H \approx 7.0\,\mu\text{m}$, $d \approx 2.0\,\mu\text{m}$; 30°: $r \approx 420\,\text{nm}$, $H \approx 7.1\,\mu\text{m}$, $d \approx 2.2\,\mu\text{m}$; $r \approx 420\,\text{nm}$, $H \approx 7.1\,\mu\text{m}$, $d \approx 1.4\,\mu\text{m}$; $r \approx 410\,\text{nm}$, $H \approx 7.0\,\mu\text{m}$, $d \approx 1.5\,\mu\text{m}$; $r \approx 420\,\text{nm}$, $H \approx 7.0\,\mu\text{m}$, $d \approx 1.7\,\mu\text{m}$; 35°: $r \approx 420\,\text{nm}$, $H \approx 7.0\,\mu\text{m}$, $d \approx 1.7\,\mu\text{m}$; $r \approx 320\,\text{nm}$, $H \approx 7.1\,\mu\text{m}$, $d \approx 1.0\,\mu\text{m}$; $r \approx 320\,\text{nm}$, $H \approx 7.0\,\mu\text{m}$, $d \approx 1.2\,\mu\text{m}$; $r \approx 440\,\text{nm}$, $H \approx 7.1\,\mu\text{m}$, $d \approx 1.4\,\mu\text{m}$; 40°: $r \approx 430\,\text{nm}$, $H \approx 7.0\,\mu\text{m}$, $d \approx 1.8\,\mu\text{m}$; $r \approx 470\,\text{nm}$, $H \approx 6.9\,\mu\text{m}$, $d \approx 1.1\,\mu\text{m}$; 45°: $r \approx 430\,\text{nm}$, $H \approx 7.0\,\mu\text{m}$, $d \approx 1.3\,\mu\text{m}$; $r \approx 320\,\text{nm}$, $H \approx 6.9\,\mu\text{m}$, $d \approx 1.0\,\mu\text{m}$; $r \approx 320\,\text{nm}$, $H \approx 7.0\,\mu\text{m}$, $d \approx 1.1\,\mu\text{m}$; $r \approx 320\,\text{nm}$, $H \approx 6.9\,\mu\text{m}$, $d \approx 1.2\,\mu\text{m}$; 0°: $r \approx 330\,\text{nm}$, $H \approx 8.2\,\mu\text{m}$, $d \approx 1.5\,\mu\text{m}$; 20°: $r \approx 330\,\text{nm}$, $H \approx 8.1\,\mu\text{m}$, $d \approx 0.9\,\mu\text{m}$; $r \approx 330\,\text{nm}$, $H \approx 8.2\,\mu\text{m}$, $d \approx 1.5\,\mu\text{m}$.

APPENDIX D

IMAGE ANALYSIS CODE

In this chapter the python code for the image analysis in Section 4.2.3 is shown.

```
#+++++++++++++++++++++++++++++++++++++++++++++++++++++++++++++++++++++++++++++++
# PACKAGES & DEFINITIONS
#+++++++++++++++++++++++++++++++++++++++++++++++++++++++++++++++++++++++++++++++
from pystackreg import StackReg
from skimage import io
import numpy as np
import cv2
import matplotlib.pyplot as plt
import math
import os
from matplotlib.patches import Ellipse
from scipy import ndimage
#+++++++++++++++++++++++++++++++++++++++++++++++++++++++++++++++++++++++++++++++

#+++++++++++++++++++++++++++++++++++++++++++++++++++++++++++++++++++++++++++++++
def plotTheImage(img):
    plt.imshow(img,cmap='gray')
    plt.xticks([]), plt.yticks([])  # to hide tick values on X and Y axis
    plt.show()
#+++++++++++++++++++++++++++++++++++++++++++++++++++++++++++++++++++++++++++++++

#+++++++++++++++++++++++++++++++++++++++++++++++++++++++++++++++++++++++++++++++
# Define parameters for image analysis
#+++++++++++++++++++++++++++++++++++++++++++++++++++++++++++++++++++++++++++++++
# Start and end number of images
start=0; numb=5001

# Rotation angle
rot_angle=2.25 # Angle in degree

# Crop limits for image
x1=110      # Starting x pixel
y1=130     # Starting y pixel
h=1010      # Height of the image
b=1020      # Width of the image

# Constants for the Segmentation, can be adjusted to improve results.
```

```
38  thresholdBlockSize = 71  # Odd number specifying the size of the block for which the local threshold
    ↪  is calculated
39  threshold = -1    # Adaptive threshold for segmentation
40
41  # Constants to select the nano-wires for analysis
42  minArea = 300, maxArea = 1500
43
44  # Tolerance value for x / y center coordinates
45  tol = 10
46  # Amplitude threshold
47  thresh=1
48  #------------------------------------------------------------------------------
49
50
51  #++++++++++++++++++++++++++++++++++++++++++++++++++++++++++++++++++++++++++++++
52  # ANALYSE IMAGE
53  #++++++++++++++++++++++++++++++++++++++++++++++++++++++++++++++++++++++++++++++
54  for x in range(start, numb):
55      # Define Raw-Image directory and load image
56      directory="".join(["StackReg\\StackReg_",str(x),".png"])
57      raw  = cv2.imread(directory, 0)
58      #++++++++++++++++++++++++++++++++++++++++++++++++++++++++++++++++++++++++++++
59
60      #++++++++++++++++++++++++++++++++++++++++++++++++++++++++++++++++++++++++++++
61      # Rotate and crop image
62      rotated = ndimage.rotate(raw, rot_angle) # Number gives angle in degree
63      crop_raw = rotated[y1:y1+h, x1:x1+b] # Crop raw image to y1 - y1+h, x1 - x1+b
64      cv2.imwrite("".join(['Croped\Croped_',str(x),'.png']),  crop_raw) # Save croped image
65      #++++++++++++++++++++++++++++++++++++++++++++++++++++++++++++++++++++++++++++
66
67      #------------------------------------------------------------------------------
68      img = cv2.fastNlMeansDenoising(crop_raw,20,10,7,21) # Denoise image
69      img8Bit = np.uint8(img)
70      binary = cv2.adaptiveThreshold(img8Bit, 255, cv2.ADAPTIVE_THRESH_GAUSSIAN_C, cv2.THRESH_BINARY,
        ↪  thresholdBlockSize, -threshold) # Binarize image
71      #++++++++++++++++++++++++++++++++++++++++++++++++++++++++++++++++++++++++++++
72
73      #------------------------------------------------------------------------------
74      result = cv2.cvtColor(img8Bit, cv2.COLOR_GRAY2RGB)
75      #------------------------------------------------------------------------------
76      out = open("".join(['Results\Results_',str(x),'.txt']),"w+")
77      out.write("# x y maxjor_x major_y minor_x minor_y EV1 EV2 (larger EV = major axis) theta\n")
78      #------------------------------------------------------------------------------
79      contours, hierarchy = cv2.findContours(binary, cv2.RETR_CCOMP, cv2.CHAIN_APPROX_SIMPLE)
80      for contour in contours:
81              if(maxArea > cv2.contourArea(contour) > minArea):
82                      cv2.drawContours(result, [contour], 0, (0,0,255), 3) # Draw contours within
                        ↪  specified area
83                      #------------------------------------------------------------------------------
84                      # Use "moments" to calculate major and minor axes as well as angle of orientation
                        ↪  of blob
85                      #------------------------------------------------------------------------------
86                      M = cv2.moments(contour)
87                      # Calculate center of mass (xC,yC) with moments
88                      xC =  M['m10']/M['m00']
89                      yC =  M['m01']/M['m00']
90                      mu20 = M['m20']/M['m00']-(xC**2)
91                      mu11 = M['m11']/M['m00']-(xC*yC)
92                      mu02 = M['m02']/M['m00']-(yC**2)
93                      cov = np.array([[mu20,mu11],[mu11,mu02]])
94
95                      # Find eigenvalues and eigenvectors
96                      evals, evecs = np.linalg.eig(cov) # Eigenvalues and eigenvectors of covariance
                        ↪  matrix
```

```
97                      sort_indices = np.argsort(evals)[::-1] # Sort eigenvalues in decreasing order
98                      x_v1, y_v1 = evecs[:, sort_indices[0]] # Eigenvector with largest eigenvalue
99                      x_v2, y_v2 = evecs[:, sort_indices[1]] # Eigenvector with smallest eigenvalue
100                     # Calculate angle of orientation of blob
101                     if evals[0]>evals[1]:
102                         theta=np.arctan2(y_v1,x_v1) # Use Eigenvector with larger eigenvalue
                            ↪  y_v1/x_v1 if EV1 is larger
103                     else:
104                         theta=np.arctan2(y_v2,x_v2) # or y_v2/x_v2 if EV2 is larger
105                     #-------------------------------------------------------------------------
106                     # Build up graph
107                     #-------------------------------------------------------------------------
108                     pMajor1 = (int(xC  - x_v1*(2*math.sqrt(evals[0]))), int(yC -
                        ↪  y_v1*(2*math.sqrt(evals[0])))) # define start point of major line
109                     pMajor2 = (int(xC  + x_v1*(2*math.sqrt(evals[0]))), int(yC +
                        ↪  y_v1*(2*math.sqrt(evals[0])))) # define end point of major line
110                     pMinor1 = (int(xC  - x_v2*(2*math.sqrt(evals[1]))), int(yC -
                        ↪  y_v2*(2*math.sqrt(evals[1])))) # define start point of minor line
111                     pMinor2 = (int(xC  + x_v2*(2*math.sqrt(evals[1]))), int(yC +
                        ↪  y_v2*(2*math.sqrt(evals[1])))) # define end point of minor line
112                     cv2.line(result, pMajor1, pMajor2, (0,255,0),   3) # draw major line from
                        ↪  pMajor1 to pMajor2
113                     cv2.line(result, pMinor1, pMinor2, (255,255,0), 3) # draw minor line from
                        ↪  pMinor1 to pMinor2
114                     #-------------------------------------------------------------------
115                     out.write("{:.3e}".format(xC) + " {:.3e}".format(yC) + " {:.3e}".format(x_v1) +
                        ↪  " {:.3e}".format(y_v1) + " {:.3e}".format(x_v2) + " {:.3e}".format(y_v2) +
                        ↪  " {:.3e}".format(2*math.sqrt(evals[0])) + "
                        ↪  {:.3e}".format(2*math.sqrt(evals[1])) + " {:.3e}".format(theta) + "\n")#
116             else:
117                     cv2.drawContours(result, [contour], 0, (225,0,0), 3) # Draw contours in new
                        ↪  color for contours outside specified area
118     cv2.imwrite("".join(['Overlay\Overlay_',str(x),'.png']),  result) # Save croped image with
        ↪  contours and major and minor axes
119     out.close()
120 #++++++++++++++++++++++++++++++++++++++++++++++++++++++++++++++++++++++++++++++++++++
121
122
123 #++++++++++++++++++++++++++++++++++++++++++++++++++++++++++++++++++++++++++++++++++++
124 # ANALYSE IMAGE REFERENCES
125 #++++++++++++++++++++++++++++++++++++++++++++++++++++++++++++++++++++++++++++++++++++
126 for x in range(start, numb):
127     #Define Raw-Image directory and load image
128     directory="".join(["StackReg\\Reference_",str(x),".png"])
129     raw  = cv2.imread(directory, 0)
130     # Load image results to measure pillars at same angle
131     results = np.loadtxt("".join(['Results\Results_',str(x),'.txt']))
132     #++++++++++++++++++++++++++++++++++++++++++++++++++++++++++++++++++++++++++++++++++++
133
134     #++++++++++++++++++++++++++++++++++++++++++++++++++++++++++++++++++++++++++++++++++++
135     # Rotate and crop image
136     rotated = ndimage.rotate(raw, rot_angle) # Number gives angle in degree
137     crop_raw = rotated[y1:y1+h, x1:x1+b] # Crop raw image to y1 - y1+h, x1 - x1+b
138     cv2.imwrite("".join(['alt\\Croped\Reference_',str(x),'.png']),  crop_raw) # Save croped image
139     #++++++++++++++++++++++++++++++++++++++++++++++++++++++++++++++++++++++++++++++++++++
140
141     #-------------------------------------------------------------------------
142     img = cv2.fastNlMeansDenoising(crop_raw,20,10,7,21) # denoise image
143     img8Bit = np.uint8(img)
144     binary = cv2.adaptiveThreshold(img8Bit, 255, cv2.ADAPTIVE_THRESH_GAUSSIAN_C, cv2.THRESH_BINARY,
        ↪  thresholdBlockSize, -threshold) # Binarize image
145     #++++++++++++++++++++++++++++++++++++++++++++++++++++++++++++++++++++++++++++++++++++
146
147     #++++++++++++++++++++++++++++++++++++++++++++++++++++++++++++++++++++++++++++++++++++
```

```
148     result = cv2.cvtColor(img8Bit, cv2.COLOR_GRAY2RGB)
149     #-------------------------------------------------------------------------
150     out = open("".join(['Results\Reference_',str(x),'.txt']),"w+")
151     out.write("# x y maxjor_x major_y minor_x minor_y EV1 EV2 (larger EV = major axis) theta\n")
152     #-------------------------------------------------------------------------
153     contours, hierarchy = cv2.findContours(binary, cv2.RETR_CCOMP, cv2.CHAIN_APPROX_SIMPLE)
154     for contour in contours:
155             if(maxArea > cv2.contourArea(contour) > minArea):
156                     cv2.drawContours(result, [contour], 0, (0,0,255), 3) # Draw contours within
                        ↪ specified area
157                     # use "moments" to calculate center of mass
158                     M = cv2.moments(contour)
159                     # Calculate center of mass (xC,yC) with moments
160                     xC =  M['m10']/M['m00']
161                     yC =  M['m01']/M['m00']
162
163                     # Testvariable, to find out whether there is a corresponding pillar in results
164                     test = 0 # reset testvariable to 0
165                     # Find corresponding pillar in measurement image
166                     for z in range(0,len(results)):
167                         if xC-tol <= results[z,0] <= xC+tol and yC-tol <= results[z,1] <= yC+tol:
168                             # Use same angle of major/minor axes orientation as in measurement image
                                ↪ for each pillar
169                             theta=results[z,8] # Read results angle for corresponding measurement
                                ↪ image and pillar
170                             es = np.array([[np.cos(theta), np.sin(theta)],[-np.sin(theta),
                                ↪ np.cos(theta)],]).T
171                             dists = np.dot(contour,es)
172                             wh = dists.max(axis=0) - dists.min(axis=0) # wh gives  width of blob,
                                ↪ for "radius" divide by 2
173                             test = 1 # set testvariable to 1, if there is a corresponding measurement
                                ↪ pillar
174                     #-------------------------------------------------------------------------
175                     # If there is no corresponding pillar in results go back to original method
176                     if test == 0: # check test variable to see whether there is a corresponding
                        ↪ pillar
177                         wh=np.empty([1,2])
178                         mu20 = M['m20']/M['m00']-(xC**2)
179                         mu11 = M['m11']/M['m00']-(xC*yC)
180                         mu02 = M['m02']/M['m00']-(yC**2)
181                         cov = np.array([[mu20,mu11],[mu11,mu02]])
182                         # l and w are length and width of blob
183                         wh[0,0] = 2*
                            ↪ math.sqrt(2*(mu20+mu02+math.sqrt(4*(mu11**2)+((mu20-mu02)**2)))) # Only
                            ↪ half of blob size, i.e. major / minor axis
184                         wh[0,1] = 2*
                            ↪ math.sqrt(2*(mu20+mu02-math.sqrt(4*(mu11**2)+((mu20-mu02)**2))))
185
186                         # Find eigenvalues and eigenvectors
187                         evals, evecs = np.linalg.eig(cov) # Eigenvalues and eigenvectors of
                            ↪ covariance matrix
188                         sort_indices = np.argsort(evals)[::-1] # Sort eigenvalues in decreasing
                            ↪ order
189                         es = np.empty([2,2]) # Set empty es array
190                         es[0,0], es[0,1] = evecs[:, sort_indices[0]] # Eigenvector with largest
                            ↪ eigenvalue
191                         es[1,0], es[1,1] = evecs[:, sort_indices[1]] # Eigenvector with smallest
                            ↪ eigenvalue
192                         # Calculate angle of orientation of blob
193                         if evals[0]>evals[1]:
194                             theta=np.arctan2(es[0,1],es[0,0]) # Use Eigenvector with larger
                                ↪ eigenvalue y_v1/x_v1 if EV1 is larger
195                         else:
196                             theta=np.arctan2(es[1,1],es[1,0]) # or y_v2/x_v2 if EV2 is larger
```

```
197                     #-------------------------------------------------------------------------------
198                     # Build up graph
199                     #-------------------------------------------------------------------------------
200                     pMajor1 = (int(xC  - np.cos(theta)*wh[0,0]/2), int(yC -
                        ↪  np.sin(theta)*wh[0,0]/2)) # define start point of major line
201                     pMajor2 = (int(xC  + np.cos(theta)*wh[0,0]/2), int(yC +
                        ↪  np.sin(theta)*wh[0,0]/2)) # define end point of major line
202                     pMinor1 = (int(xC  - np.cos(np.pi/2+theta)*wh[0,1]/2), int(yC -
                        ↪  np.sin(np.pi/2+theta)*wh[0,1]/2)) # define start point of minor line
203                     pMinor2 = (int(xC  + np.cos(np.pi/2+theta)*wh[0,1]/2), int(yC +
                        ↪  np.sin(np.pi/2+theta)*wh[0,1]/2)) # define end point of minor line
204                     cv2.line(result, pMajor1, pMajor2, (0,255,0),   3) # draw major line from
                        ↪  pMajor1 to pMajor2
205                     cv2.line(result, pMinor1, pMinor2, (255,255,0), 3) # draw minor line from
                        ↪  pMinor1 to pMinor2
206                     #-------------------------------------------------------------------------------
207                     out.write("{:.3e}".format(xC) + " {:.3e}".format(yC) + " {:.3e}".format(es[0,0])
                        ↪  + " {:.3e}".format(es[0,1]) + " {:.3e}".format(es[1,0]) + "
                        ↪  {:.3e}".format(es[1,1]) +  " {:.3e}".format(wh[0,0]/2) + "
                        ↪  {:.3e}".format(wh[0,1]/2) + " {:.3e}".format(theta) + "\n")
208             else:
209                     cv2.drawContours(result, [contour], 0, (225,0,0), 3) # Draw contours in new
                        ↪  color for shapes outside specified area
210     #cv2.imwrite("".join(['Overlay\\Reference_',str(x),'.png']),  result)  # Save croped image with
        ↪  contours and major and minor axes
211     out.close()
212 #################################################################################
213
214
215 #################################################################################
216 # CALCULATE VIBRATION AMPLITUDE
217 #################################################################################
218 # Load single measurement data and corresponding reference data
219 for z in range(start, numb):
220     #-------------------------------------------------------------------------------
221     # Load data
222     results = np.loadtxt("".join(['Results\Results_',str(z),'.txt']))# Load txt file with position
        ↪  and vibration axes data
223     reference = np.loadtxt("".join(['Results\Reference_',str(z),'.txt']))# Load reference data
224     #-------------------------------------------------------------------------------
225
226         #-------------------------------------------------------------------------------
227     # Define empty matrices
228     diff=np.empty([len(reference),7]) # define empty difference matrix
229     amp=np.empty([1,7]) # define empty amplitude array
230     pairs=np.empty(len(reference)) # define empty reference / results pairs matrix
231     alert=np.empty([1,3]) # define empty alert matrix for missing reference positions
232     pairs1=0
233     #-------------------------------------------------------------------------------
234
235     #-------------------------------------------------------------------------------
236     # for loop sorts each pillar position of measurement and reference and calculates differences of
        ↪  EVs.
237     for y in range(0, len(reference)):
238         for x in range(0, len(results)):
239             if results[x,0]-tol <= reference[y,0] <= results[x,0]+tol and results[x,1]-tol <=
                ↪  reference[y,1] <= results[x,1]+tol: # compare x/y position of data and reference
                ↪  within tol
240                 diff[y]=[results[x,0],results[x,1],results[x,6],results[x,7],
241                 (results[x,6]-reference[y,6]),(results[x,7]-reference[y,7]),results[x,8]] # build
                    ↪  difference matrix: x/y position, major/minor axis, major/minor amplitudes, angle
242                 pairs[y]=y # put all y (reference pillars) that have a corresponding x (measurement
                    ↪  pillars) in an array
243                 pairs1=np.append(pairs1,y)
```

```
244     pairs1=np.delete(pairs1,0)
245 
246     for y in range(0, len(reference)):
247         if y not in pairs1: # find y that don't have corresponding x
248             alert=np.append(alert,[[reference[y,0],reference[y,1],y]],axis=0) # collect all lonely y
                ↪  in alert matrix
249     #-------------------------------------------------------------------------
250     # Delete beginning position of alert, which was only used as start with no real data in it
251     alert=np.delete(alert,0,0)
252     # Save alert if it is not empty
253     if alert.size!=0:
254         np.savetxt("".join(['Alert\Alert_',str(z),'.txt']),alert)
255     #-------------------------------------------------------------------------
256     # Delete non-filled positions
257     diff=np.delete(diff,alert[...,2],0)
258     #-------------------------------------------------------------------------
259     # Sort amplitudes above certain threshold (1 pixel) from diff in amp: position x/y, EV1, EV2,
        ↪  diff1, diff2, theta
260     for x in range (0,len(diff)):
261         if diff[x,5]>thresh or diff[x,4]>thresh:
262             amp=np.append(amp,[diff[x]],axis=0)
263     #-------------------------------------------------------------------------
264     # Delete first position which was used as starting array for append
265     amp=np.delete(amp,0,0)
266     #-------------------------------------------------------------------------
267 
268     #-------------------------------------------------------------------------
269     # Save amplitude txt file only if it is not empty
270     if amp.size!=0:
271         np.savetxt("".join(['Amplitudes\Amplitudes_',str(z),'.txt']),amp)
272 #-----------------------------------------------------------------------------
273 
274 
275 #+++++++++++++++++++++++++++++++++++++++++++++++++++++++++++++++++++++++++++++
276 # MARK VIBRATING PILLARS WITH LINES
277 #+++++++++++++++++++++++++++++++++++++++++++++++++++++++++++++++++++++++++++++
278 # Scale factor and linewidth
279 scale=3; lw=5
280 #+++++++++++++++++++++++++++++++++++++++++++++++++++++++++++++++++++++++++++++
281 # Loop through images
282 for z in range(start, numb):
283     #-------------------------------------------------------------------------
284     # Get croped image
285     raw  = cv2.imread("".join(['Croped\Croped_',str(z),'.png']), 1)
286     #-------------------------------------------------------------------------
287 
288     #-------------------------------------------------------------------------
289     # Load txt file with position, amplitude and angle data
290     if os.path.exists("".join(['Amplitudes\Amplitudes_',str(z),'.txt'])):
291         amp = np.loadtxt("".join(['Amplitudes\Amplitudes_',str(z),'.txt']))
292 
293         # Read position data
294         x=amp[...,0] # x position vector
295         y=amp[...,1] # y position vector
296         l=amp[...,4] # length vector, only real amplitude (meas-ref)
297         w=amp[...,5] # width vector, only real amplitude
298         b=amp[...,6] # angle vector, b=90+amp[...,6]*180/math.pi#+90
299         #---------------------------------------------------------------------
300 
301         #-----------------------------------------------------------------------------
302         # Loop through coordinate vectors, minor/major axes and angle
303         if x.size>1: # for loop doesn't work for vector with only one position
304             for xx,yy,ll,ww,bb in zip(x,y,l,w,b):
```

```
305                 pMajor1 = (int(xx  - np.cos(math.pi/2+bb)*ww*scale), int(yy -
                    ↪  np.sin(math.pi/2+bb)*ww*scale))# start point of major line
306                 pMajor2 = (int(xx  + np.cos(math.pi/2+bb)*ww*scale), int(yy +
                    ↪  np.sin(math.pi/2+bb)*ww*scale)) # end point of major line
307                 pMinor1 = (int(xx  - np.cos(bb)*ll*scale), int(yy - np.sin(bb)*ll*scale)) # start
                    ↪  point of minor line
308                 pMinor2 = (int(xx  + np.cos(bb)*ll*scale), int(yy + np.sin(bb)*ll*scale)) # end
                    ↪  point of minor line
309                 if ww>thresh and ll<=thresh: # Cases: amplitude only along w-axis
310                     cv2.line(raw, pMajor1, pMajor2, (255,0,0),lw) # draw only along w-axis
311                 elif ll>thresh and ww<=thresh: # Cases: amplitude only along l-axis
312                     cv2.line(raw, pMinor1, pMinor2, (0,0,255), lw) # draw only along l-ais
313                 elif ll>thresh and ww>thresh: # Cases: amplitude along w- & l-axis
314                     cv2.ellipse(raw, (int(xx),int(yy)), (int(scale*ll),int(scale*ww)),
                        ↪  bb*180/math.pi, 0, 360, (0,255,0), lw) # draw elliptical amplitude
315             else: # deal with vectors with only one position
316                 pMajor1 = (int(x  - np.cos(math.pi/2+b)*w), int(y - np.sin(math.pi/2+b)*w)) # start
                    ↪  point of major line
317                 pMajor2 = (int(x  + np.cos(math.pi/2+b)*w), int(y + np.sin(math.pi/2+b)*w)) # end point
                    ↪  of major line
318                 pMinor1 = (int(x  - np.cos(b)*l), int(y - np.sin(b)*l)) # start point of minor line
319                 pMinor2 = (int(x  + np.cos(b)*l), int(y + np.sin(b)*l)) # end point of minor line
320                 if w>thresh and l<=thresh: # Cases: amplitude only along w-axis
321                         cv2.line(raw, pMajor1, pMajor2, (255,0,0),lw) # draw only along w-axis
322                 elif l>thresh and w<=thresh: # Cases: amplitude only along l-axis
323                     cv2.line(raw, pMinor1, pMinor2, (0,0,255), lw) # draw only along l-ais
324                 elif l>thresh and w>thresh: # Cases: amplitude along w- & l-axis
325                     cv2.ellipse(raw, (int(x),int(y)), (int(scale*l),int(scale*w)), b*180/math.pi, 0,
                        ↪  360, (0,255,0),lw) # draw elliptical amplitude
326             #-------------------------------------------------------------------------
327
328             #-------------------------------------------------------------------------
329             # Add yellow dots for too large amplitudes that are collected in Alert_x.txt
330             if os.path.exists("".join(['Alert\Alert_',str(z),'.txt'])): # Load Alert_x.txt if it exists
331                 alert = np.loadtxt("".join(['Alert\Alert_',str(z),'.txt']))
332                 #---------------------------------------------------------------------------
333
334                 #---------------------------------------------------------------------------
335                 # Read position data in x and y vector of pillars with too large amplitude
336                 x=alert[...,0] # x position vector of alert pillars
337                 y=alert[...,1] # y position vector of alert pillars
338                 #---------------------------------------------------------------------------
339
340                 #---------------------------------------------------------------------------
341                 # Loop through coordinate array, and create a yellow circle at each x,y pair from alert
342                 if x.size>1:
343                     for xx,yy in zip(x,y):
344                         cv2.circle(raw,(int(xx),int(yy)),5,(0,255,225),lw)
345                 else:
346                     cv2.circle(raw,(int(x),int(y)),5,(0,255,255),lw)
347             #-------------------------------------------------------------------------
348             # Save croped image with overlay of amplitude lines and ellipses
349             cv2.imwrite("".join(['Lines\Lines_',str(z),'.png']),  raw)
350 #++++++++++++++++++++++++++++++++++++++++++++++++++++++++++++++++++++++++++++++++++++
```

APPENDIX E

SUPPLEMENTARY COUPLED NANOMECHANICAL PILLAR ARRAYS

This chapter provides supplementary information to the tight-binding model of coupled nanopillar arrays in Section 4.1.

In the introduced tight-binding theory from Section 4.1, the diagonal part of the Hamiltonian $H_{\mathsf{d}}^{i,j}$ for a central pillar at (i,j) is given by

$$\begin{aligned} H_{\mathsf{d}}^{i,j} = & \\ -\Bigg[\Bigg(& J_{\mathsf{d,ll}}\left(\frac{b_x^{i,j\dagger}+b_y^{i,j\dagger}}{\sqrt{2}}\right)\left(\frac{b_x^{i+1,j+1}+b_y^{i+1,j+1}}{\sqrt{2}}\right)+J_{\mathsf{d,tt}}\left(\frac{b_x^{i,j\dagger}-b_y^{i,j\dagger}}{\sqrt{2}}\right)\left(\frac{b_x^{i+1,j+1}-b_y^{i+1,j+1}}{\sqrt{2}}\right) \\ & +J_{\mathsf{d,lt}}\left(\frac{b_x^{i,j\dagger}-b_y^{i,j\dagger}}{\sqrt{2}}\right)\left(\frac{b_x^{i+1,j+1}+b_y^{i+1,j+1}}{\sqrt{2}}\right)+J_{\mathsf{d,lt}}\left(\frac{b_x^{i,j\dagger}+b_y^{i,j\dagger}}{\sqrt{2}}\right)\left(\frac{b_x^{i+1,j+1}-b_y^{i+1,j+1}}{\sqrt{2}}\right)\Bigg)+\mathsf{h.c.}\Bigg] \\ -\Bigg[\Bigg(& J_{\mathsf{d,ll}}\left(\frac{b_x^{i,j\dagger}-b_y^{i,j\dagger}}{\sqrt{2}}\right)\left(\frac{b_x^{i+1,j-1}-b_y^{i+1,j-1}}{\sqrt{2}}\right)+J_{\mathsf{d,tt}}\left(\frac{b_x^{i,j\dagger}+b_y^{i,j\dagger}}{\sqrt{2}}\right)\left(\frac{b_x^{i+1,j-1}+b_y^{i+1,j-1}}{\sqrt{2}}\right) \\ & +J_{\mathsf{d,lt}}\left(\frac{b_x^{i,j\dagger}-b_y^{i,j\dagger}}{\sqrt{2}}\right)\left(\frac{b_x^{i+1,j-1}+b_y^{i+1,j-1}}{\sqrt{2}}\right)+J_{\mathsf{d,lt}}\left(\frac{b_x^{i,j\dagger}+b_y^{i,j\dagger}}{\sqrt{2}}\right)\left(\frac{b_x^{i+1,j-1}-b_y^{i+1,j-1}}{\sqrt{2}}\right)\Bigg)+\mathsf{h.c.}\Bigg]. \end{aligned} \tag{E.1}$$

Following the calculations in the main part, a solution

$$\begin{pmatrix} x(t)^{i,j} \\ y(t)^{i,j} \end{pmatrix} = 2x_{\mathsf{zpf}}\begin{pmatrix} A\cos\left(\omega_{\mathsf{exc}}t+\Phi_x\right) \\ B\cos\left(\omega_{\mathsf{exc}}t+\Phi_y\right) \end{pmatrix} \tag{E.2}$$

can be found.

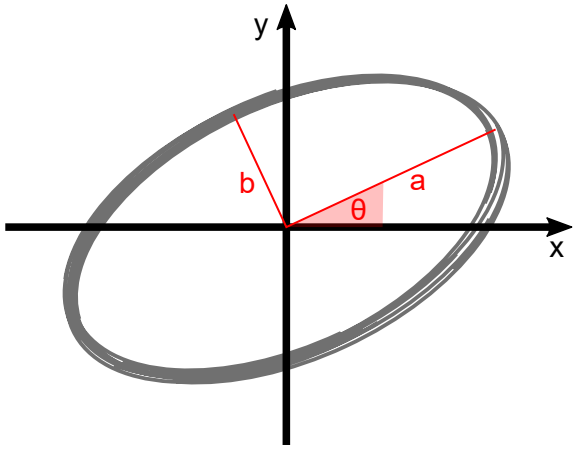

Figure E.1: **Sketch of the pillar trajectory.** Sketch from a general pillar trajectory viewed from above. Major and minor axes a and b as well as orientation angle Θ are marked.

With Figure 4.4 the extension of the trajectory can be found. The major and minor axes a and b as in Figure E.1 are

$$a, b = \frac{AB}{\sqrt{2}} \left[\frac{1}{A^2} + \frac{1}{B^2} \pm \left(\left(\frac{1}{A^2} - \frac{1}{B^2} \right)^2 + \frac{4}{A^2 B^2} \cos^2(\Phi_x - \Phi_y) \right)^{1/2} \right]^{1/2} \tag{E.3}$$

with orientation angle Θ

$$\Theta = \arctan \left[\frac{-AB}{2\cos(\Phi_x - \Phi_y)} \left[\frac{1}{A^2} - \frac{1}{B^2} - \left(\left(\frac{1}{A^2} - \frac{1}{B^2} \right)^2 + \frac{4}{A^2 B^2} \cos^2(\Phi_x - \Phi_y) \right)^{1/2} \right] \right]. \tag{E.4}$$

THANKS

Here, I would like to thank everyone who contributed to this work in his or her own way.

First of all, I want to thank *Prof. Eva Weig* who was my supervisor on this project. Dear Eva, you gave me the possibility to work on this very exciting research project. During the time of my thesis I always felt supported by you, either through your ideas and expertise in this field or through your confidence in my own approaches and suggestions. You also managed to maintain a constructive, respectful and pleasant atmosphere in the nanomechanics group at all times which made the time in your group not only productive but also enjoyable. I further want to thank you for enabling countless opportunities and experiences outside the laboratory, e.g. visiting conferences or meetings.

I want to thank *Prof. Elke Scheer*, who thankfully agreed to take the time to read and review this thesis. I also want to thank you together with *Prof. Wolfgang Belzig* for completing the examination board in my defense where the two of you cover the experimental and theoretical special topic.

I would also like to thank our collaborators from the LMU Munich. *Philipp Paulitschke* and *Heribert Lorenz*, both of you always took the time to discuss new results or problems we encountered and contributed into pushing the project forward. Especially you, Philipp were always ready to help with your experience in the topic. The two of you also enabled my work in the cleanroom of the LMU Munich which was crucial for the fabrication of nanopillars. Further thanks goes to *Philipp Altpeter* and *Ester Porcellato*. The two of you always took the time to help me with your technical expertise in the cleanroom. I also want to thank *Valentin Stierle* from the Munich crew, who helped me getting acquainted with python image processing and set up a first code lines.

I wish to thank our collaborators from the Max-Planck Institute for the Science of Light

in Erlangen – *Tirth Shah*, *Thomas Fösel* and *Prof. Florian Marquardt*, who developed the tight-binding theory. In countless discussions we were able to use our combined theoretical and experimental view to drive the project to its current state. Tirth, I want to thank you especially for taking the time to answer my many theory related questions.

Many thanks goes to *Mike Hettich* from the Research Center for Non-Destructive Testing GmbH in Linz. Your enthusiasm led to many fruitful discussions and I hope the project continues to produce interesting results. *Paul Stritt*, in the course of this collaboration I got to work with you together on an actual research experiment after our experimenting together in school as *Experimentemann* and *Denkefrau*. It was a joy to work with you.

Special thanks go to my two Master students *Simon Hönl* and *Milan Jubitz*. Both of you brought your own valuable contributions to this project. Thanks also to *Daniela Mink* and *Florian Johannsen* for great work in their student's projects.

I would like to thank *Matthias Hagner*, head of the Nanolab in Konstanz, for all his professional advice in his kind and uncomplitated way.

Of course I want to thank the whole nanomechanics group and former members: *Louis Kukk*, *Maximilian Bückle*, *Katrin Gajo*, *Felix Rochau*, *Alexandre Brieussel*, *Jana Ochs*, *Yannick Klaß*, *Anh Tuan Le*, *Irene Sánchez Arribas* and *Avishek Chowdhury*. It was great to work and spend time with all of you, be it at physics discussions, everyone with his or her own expertise, at political discussions or just having a great time in one of our coffee breaks, cooking actions in or outside the university, *Weinfest* or *Fasnet* with you. Maximilian, through many more or less rough discussions and arguments you have become a great friend and office buddy to me. Katrin, I enjoyed the time we went to conferences together sharing a room. You became a dependable friend occasionally helping out with chocolate when it was necessary. Louis, thanks for all your technical expertise, when you again and again magically provided the perfect solution to any mechanical problem I encountered. Louis, with your friendliness and your thoughtfullness working with you was always a joy.

I want to thank all the people who provided helpful input when proof-reading this thesis: Maximilian, Felix, Jana, Yannick, Tuan, Irene, Tirth, David, Paul and Eva.

Finally, I would like to thank my family *Frank*, *David* and *Dominik* and especially my mother *Margot Doster*. You always encouraged me to pursue what I wanted, you supported and motivated me. Thank you.

BIBLIOGRAPHY

[1] Christiaan Huygens. *Oeuvres complètes de Christiaan Huygens. Publiées par la Société hollandaise des sciences*. M. Nijhoff, La Haye, 1888. doi: 10.5962/bhl.title.21031.

[2] Henrique M. Oliveira and Luís V. Melo. Huygens synchronization of two clocks. *Scientific Reports*, 5(1):11548, 2015. doi: 10.1038/srep11548. URL https://www.nature.com/articles/srep11548.

[3] R. Bader. *Nonlinearities and Synchronization in Musical Acoustics and Music Psychology*, volume 2 of *Current Research in Systematic Musicology*. Springer, Berlin, Heidelberg, 2013. ISBN 9783642360985. URL https://books.google.de/books?id=xQhHAAAAQBAJ.

[4] A. Pikovsky, J. Kurths, and M. Rosenblum. *Synchronization: A universal concept in nonlinear sciences*, volume 12 of *Cambridge nonlinear science series*. Cambridge University Press, Cambridge, 2001. ISBN 9780521533522. doi: 10.1017/CBO9780511755743. URL https://doi.org/10.1017/CBO9780511755743.

[5] Grigory V. Osipov, J. Kurths, and C. Zhou. *Synchronization in oscillatory networks*. Springer series in synergetics. Springer, Berlin and London, 1. aufl. edition, 2007. ISBN 3540712682. URL http://site.ebrary.com/lib/alltitles/docDetail.action?docID=10189258.

[6] G. Bánfalvi. Overview of Cell Synchronization. In G. Bánfalvi, editor, *Cell cycle synchronization*, Springer protocols, pages 3–27. Humana Press, New York, 2017. ISBN 978-1-4939-6603-5.

[7] M. Z. Hasan and C. L. Kane. Topological Insulators. *Review of Modern Physics*, 82 (4):3045–3067, 2010. doi: 10.1103/RevModPhys.82.3045. URL https://link.aps.org/doi/10.1103/RevModPhys.82.3045.

[8] N. Engheta and R. W. Ziolkowski. *Electromagnetic metamaterials: Physics and engineering aspects*. Wiley and John Wiley [distributor], Hoboken, N.J. and Chichester, 2005. ISBN 9780471761020.

[9] T. Ozawa, H. M. Price, A. Amo, N. Goldman, M. Hafezi, L. Lu, M. C. Rechtsman, D. Schuster, J. Simon, O. Zilberberg, and I. Carusotto. Topological photonics. *Review of Modern Physics*, 2018. URL https://journals.aps.org/rmp/abstract/10.1103/RevModPhys.91.015006.

[10] M. Aspelmeyer, T. J. Kippenberg, and F. Marquardt. Cavity optomechanics. *Review of Modern Physics*, 86(4):1391–1452, 2014. doi: 10.1103/RevModPhys.86.1391. URL https://journals.aps.org/rmp/abstract/10.1103/RevModPhys.86.1391.

[11] D. Lee, K. W. Lee, Jeffrey V. Cady, P. Ovartchaiyapong, and A. C. Bleszynski Jayich. Topical review: spins and mechanics in diamond. *Journal of Optics*, 19(3): 033001, 2017. ISSN 2040-8986. doi: 10.1088/2040-8986/aa52cd. URL https://iopscience.iop.org/article/10.1088/2040-8986/aa52cd.

[12] M. H. Matheny, M. Grau, L. G. Villanueva, R. B. Karabalin, M. C. Cross, and M. L. Roukes. Phase Synchronization of Two Anharmonic Nanomechanical Oscillators. *Physical Review Letters*, 112(1):014101, 2014. doi: 10.1103/PhysRevLett.112.014101. URL http://link.aps.org/doi/10.1103/PhysRevLett.112.014101.

[13] M. Zhang, S. Shah, J. Cardenas, and M. Lipson. Synchronization and Phase Noise Reduction in Micromechanical Oscillator Arrays Coupled through Light. *Physical Review Letters*, 115(16):163902, 2015. doi: 10.1103/PhysRevLett.115.163902. URL http://link.aps.org/doi/10.1103/PhysRevLett.115.163902.

[14] T. Tian, Y. Ke, L. Zhang, S. Lin, Z. Shi, Pu Huang, C. Lee, and J. Du. Observation of dynamical phase transitions in a topological nanomechanical system. *Physical Review B*, 100(2):024310, 2019. ISSN 1098-0121. doi: 10.1103/PhysRevB.100.024310. URL https://journals.aps.org/prb/abstract/10.1103/PhysRevB.100.024310.

[15] J. Cha and C. Daraio. Electrical tuning of elastic wave propagation in nanomechanical lattices at MHz frequencies. *Nature Nanotechnology*, 2018. doi: 10.1038/s41565-018-0252-6. URL https://doi.org/10.1038/s41565-018-0252-6.

[16] R. B. Karabalin, M. C. Cross, and M. L. Roukes. Nonlinear dynamics and chaos in two coupled nanomechanical resonators. *Physical Review B*, 79(16):25, 2009. ISSN 1098-0121. doi: 10.1103/PhysRevB.79.165309. URL https://doi.org/10.1103/PhysRevB.79.165309.

[17] K. Gajo, S. Schüz, and E. M. Weig. Strong 4-mode coupling of nanomechanical string resonators. *Applied Physics Letters*, 111(13):133109, 2017. ISSN 0003-6951. doi: 10.1063/1.4995230. URL https://doi.org/10.1063/1.4995230.

[18] M. Pernpeintner, P. Schmidt, D. Schwienbacher, R. Gross, and H. Huebl. Frequency Control and Coherent Excitation Transfer in a Nanostring-resonator Network. *Physical Review Applied*, 10(3), 2018. doi: 10.1103/physrevapplied.10.034007. URL https://doi.org/10.1103/PhysRevApplied.10.034007.

[19] D. Hatanaka, I. Mahboob, K. Onomitsu, and H. Yamaguchi. Phonon waveguides for electromechanical circuits. *Nature Nanotechnology*, 9(7):520–524, 2014. doi: 10.1038/nnano.2014.107. URL https://www.nature.com/articles/nnano.2014.107.

[20] J. Cha, K. W. Kim, and C. Daraio. Experimental realization of on-chip topological nanoelectromechanical metamaterials. *Nature*, 564(7735):229–233, 2018. doi: 10.1038/s41586-018-0764-0. URL https://www.nature.com/articles/s41586-018-0764-0.

[21] M. K. Zalalutdinov, J. W. Baldwin, M. H. Marcus, R. B. Reichenbach, J. M. Parpia, and B. H. Houston. Two-dimensional array of coupled nanomechanical resonators. *Applied Physics Letters*, 88(14):143504, 2006. ISSN 0003-6951. doi: 10.1063/1.2190448. URL https://aip.scitation.org/doi/full/10.1063/1.2190448.

[22] W. Hällström, M. Lexholm, D. B. Suyatin, G. Hammarin, D. Hessman, L. Samuelson, L. Montelius, M. Kanje, and C. N. Prinz. Fifteen-piconewton force detection from neural growth cones using nanowire arrays. *Nano Letters*, 10(3):782–787, 2010. doi: 10.1021/nl902675h.

[23] P. Paulitschke, F. Keber, A. Lebedev, J. Stephan, H. Lorenz, S. Hasselmann, D. Heinrich, and E. M. Weig. Ultra-flexible nanowire array for label- and distortion-free cellular force tracking. *Nano Letters*, 2018. doi: 10.1021/acs.nanolett.8b02568. URL https://pubs.acs.org/doi/10.1021/acs.nanolett.8b02568.

[24] P. Paulitschke, N. Seltner, A. Lebedev, H. Lorenz, and E. M. Weig. Size-independent Young's modulus of inverted conical GaAs nanowire resonators. *Applied Physics Letters*, 103(26):261901, 2013. ISSN 0003-6951. doi: 10.1063/1.4851897. URL https://doi.org/10.1063/1.4851897.

[25] D. v. Scheible and R. H. Blick. Silicon nanopillars for mechanical single-electron transport. *Applied Physics Letters*, 84(23):4632–4634, 2004. ISSN 0003-6951. doi: 10.1063/1.1759371. URL https://aip.scitation.org/doi/10.1063/1.1759371.

[26] I. Yeo, P.-L. de Assis, A. Gloppe, E. Dupont-Ferrier, P. Verlot, N. S. Malik, E. Dupuy, J. Claudon, J.-M. Gérard, A. Auffèves, G. Nogues, S. Seidelin, J.-Ph. Poizat, O. Arcizet, and M. Richard. Strain-mediated coupling in a quantum dot-mechanical oscillator hybrid system. *Nature Nanotechnology*, 9(2):106–110, 2014. doi: 10.1038/NNANO.2013.274. URL https://doi.org/10.1038/nnano.2013.274.

[27] N. Rossi, F. R. Braakman, D. Cadeddu, D. Vasyukov, G. Tütüncüoglu, A. Fontcuberta i Morral, and M. Poggio. Vectorial scanning force microscopy using a nanowire sensor. *Nature Nanotechnology*, 12(2):150–155, 2017. doi: 10.1038/NNANO.2016.189. URL https://doi.org/10.1038/nnano.2016.189.

[28] L. Mercier de Lépinay, B. Pigeau, B. Besga, P. Vincent, P. Poncharal, and O. Arcizet. A universal and ultrasensitive vectorial nanomechanical sensor for imaging 2D force fields. *Nature Nanotechnology*, 12(2):156–162, 2017. doi: 10.1038/NNANO.2016.193. URL https://doi.org/10.1038/nnano.2016.193.

[29] S. Anguiano, A. E. Bruchhausen, B. Jusserand, I. Favero, F. R. Lamberti, L. Lanco, I. Sagnes, A. Lemaître, N. D. Lanzillotti-Kimura, P. Senellart, and A. Fainstein. Micropillar Resonators for Optomechanics in the Extremely High 19-95-GHz Frequency Range. *Physical Review Letters*, 118(26):263901, 2017. doi: 10.1103/PhysRevLett.118.263901. URL https://doi.org/10.1103/PhysRevLett.118.263901.

[30] S. Benchabane, R. Salut, O. Gaiffe, V. Soumann, M. Addouche, V. Laude, and A. Khelif. Surface-Wave Coupling to Single Phononic Subwavelength Resonators. *Physical Review Applied*, 8(3), 2017. doi: 10.1103/physrevapplied.8.034016. URL https://doi.org/10.1103/PhysRevApplied.8.034016.

[31] D. Wigger, C. Schneider, S. Gerhardt, M. Kamp, S. Höfling, T. Kuhn, and J. Kasprzak. Rabi oscillations of a quantum dot exciton coupled to acoustic phonons: coherence and population readout. *Optica*, 5(11):1442, 2018. doi: 10.1364/OPTICA.5.001442. URL https://doi.org/10.1364/OPTICA.5.001442.

[32] M. Pelliccione, A. Jenkins, P. Ovartchaiyapong, C. Reetz, E. Emmanouilidou, N. Ni, and A. C. Bleszynski Jayich. Scanned probe imaging of nanoscale magnetism at cryogenic temperatures with a single-spin quantum sensor. *Nature Nanotechnology*, 11(8):700–705, 2016. URL http://dx.doi.org/10.1038/nnano.2016.68.

[33] W. Weaver, S. P. Timošenko, and D. H. Young. *Vibration problems in engineering*. A Wiley Interscience publication. Wiley, New York, 5. ed. edition, 1990. ISBN 978-0-471-63228-3.

[34] Michael E. Mortenson. *Mathematics for computer graphics applications: An introduction to the mathematics and geometry of CAD/CAM, geometric modeling, scientific visualization, and other CG applications / Michael Mortenson*. Industrial Press, New York, 2nd ed. edition, 1999. ISBN 9780831131111. URL https://books.google.de/books?id=YmQy799flPkC.

[35] T. B. Bateman, H. J. McSkimin, and J. M. Whelan. Elastic Moduli of Single–Crystal Gallium Arsenide. *Journal of Applied Physics*, 30(4):544–545, 1959. ISSN 0021-8979. doi: 10.1063/1.1702401. URL https://aip.scitation.org/doi/10.1063/1.1702401.

[36] P. Paulitschke. *Mechanische Charakterisierung einzelner & periodisch angeordneter nanoskaliger GaAs-Säulen*. Doctoral thesis, Ludwigs-Maximilians-Universität, München, 2011.

[37] P. Loch. *Beugungsdetektion zweidimensionaler Beugungsdetektion zweidimensionaler GaAs-Säulengitter in verschiedenen Umgebungsmedien*. Master's thesis, Ludwigs-Maximilians-Universität, München, 2012.

[38] T. Mittereder. *Diffraction measurements on a lattice of actuated nanomechanical GaAs pillars*. Master's thesis, Ludwigs-Maximilians-Universität, München, 2012.

[39] M. Volatier, D. Duchesne, R. Morandotti, R. Arès, and V. Aimez. Extremely high aspect ratio GaAs and GaAs/AlGaAs nanowaveguides fabricated using chlorine ICP etching with N2-promoted passivation. *Nanotechnology*, 21(13):134014, 2010. ISSN 0957-4484. doi: 10.1088/0957-4484/21/13/134014.

[40] B. Sanii and P. D. Ashby. High sensitivity deflection detection of nanowires. *Physical Review Letters*, 104(14):147203, 2010. doi: 10.1103/PhysRevLett.104.147203. URL https://doi.org/10.1103/PhysRevLett.104.147203.

[41] J. Molina, D. Ramos, E. Gil-Santos, J. E. Escobar, J. J. Ruz, J. Tamayo, Á. San Paulo, and M. Calleja. Optical Transduction for Vertical Nanowire Resonators. *Nano Letters*, 20(4):2359–2369, 2020. doi: 10.1021/acs.nanolett.9b04909. URL https://pubs.acs.org/doi/10.1021/acs.nanolett.9b04909.

[42] S. Hoenl. *Dynamics and Mechanical Coupling Dynamics and Mechanical Phenomena in Negatively Tapered Gallium Arsenide Nanowires*. Master's thesis, University of Konstanz, Konstanz, 2016.

[43] P. Paulitschke. *Anregung dreidimensionaler Halbleiter Nano-/Mikrostrukturen*. Diplomarbeit, Ludwigs-Maximilians-Universität, München, 2007.

[44] A. P. Foster, J. K. Maguire, J. P. Bradley, T. P. Lyons, A. B. Krysa, A. M. Fox, M. S. Skolnick, and L. R. Wilson. Tuning Nonlinear Mechanical Mode Coupling in

GaAs Nanowires Using Cross-Section Morphology Control. *Nano Letters*, 16(12): 7414–7420, 2016. doi: 10.1021/acs.nanolett.6b02994. URL https://pubs.acs.org/doi/abs/10.1021/acs.nanolett.6b02994.

[45] J. Doster, S. Hoenl, H. Lorenz, P. Paulitschke, and E. M. Weig. Collective dynamics of strain-coupled nanomechanical pillar resonators. *Nature Communications*, 10(1): 5246, 2019. ISSN 2041-1723. doi: 10.1038/s41467-019-13309-9. URL https://doi.org/10.1038/s41467-019-13309-9.

[46] E. Gil-Santos, C. Baker, A. Lemaître, C. Gomez, G. Leo, and I. Favero. Scalable high-precision tuning of photonic resonators by resonant cavity-enhanced photoelectrochemical etching. *Nature Communications*, 8:14267, 2017. ISSN 2041-1723. doi: 10.1038/ncomms14267. URL https://www.nature.com/articles/ncomms14267.

[47] M. Levinshtein, S. Rumyantsev, and M. Shur. *Handbook Series on Semiconductor Parameters - Volume 2: Ternary And Quaternary III-V Compounds*, volume 2. WORLD SCIENTIFIC, 1996. ISBN 978-981-02-1420-3. doi: 10.1142/2046-vol2. URL http://www.ioffe.ru/SVA/NSM.

[48] D. E. Aspnes, S. M. Kelso, R. A. Logan, and R. Bhat. Optical properties of AlxGa1−xAs. *Journal of Applied Physics*, 60(2):754–767, 1986. ISSN 0021-8979. doi: 10.1063/1.337426. URL https://aip.scitation.org/doi/10.1063/1.337426.

[49] A. Kiraz, P. Michler, C. Becher, B. Gayral, A. Imamoğlu, L. Zhang, E. Hu, W. V. Schoenfeld, and P. M. Petroff. Cavity-quantum electrodynamics using a single InAs quantum dot in a microdisk structure. *Applied Physics Letters*, 78(25):3932–3934, 2001. ISSN 0003-6951. doi: 10.1063/1.1379987. URL https://doi.org/10.1063/1.1379987.

[50] J. P. Reithmaier, G. Sek, A. Löffler, C. Hofmann, S. Kuhn, S. Reitzenstein, L. V. Keldysh, V. D. Kulakovskii, T. L. Reinecke, and A. Forchel. Strong coupling in a single quantum dot-semiconductor microcavity system. *Nature*, 432(7014): 197–200, 2004. doi: 10.1038/nature02969. URL https://doi.org/10.1038/nature02969.

[51] T. Yoshie, A. Scherer, J. Hendrickson, G. Khitrova, H. M. Gibbs, G. Rupper, C. Ell, O. B. Shchekin, and D. G. Deppe. Vacuum Rabi splitting with a single quantum dot in a photonic crystal nanocavity. *Nature*, 432(7014):200–203, 2004. doi: 10.1038/nature03119. URL https://doi.org/10.1038/nature03119.

[52] L. Novotny. Strong coupling, energy splitting, and level crossings: A classical perspective. *American Journal of Physics*, 78(11):1199–1202, 2010. ISSN 0002-9505. doi: 10.1119/1.3471177. URL https://doi.org/10.1119/1.3471177.

[53] P. Ovartchaiyapong, K. W. Lee, B. A. Myers, and A. C. Bleszynski Jayich. Dynamic strain-mediated coupling of a single diamond spin to a mechanical resonator. *Nature Communications*, 5:4429, 2014. ISSN 2041-1723. doi: 10.1038/ncomms5429. URL https://doi.org/10.1038/ncomms5429.

[54] M. A. Hopcroft, W. D. Nix, and T. W. Kenny. What is the Young's Modulus of Silicon? *Journal of Microelectromechanical Systems*, 19(2):229–238, 2010. ISSN 1057-7157. doi: 10.1109/JMEMS.2009.2039697. URL https://doi.org/10.1109/JMEMS.2009.2039697.

[55] M. Aspelmeyer, T. J. Kippenberg, and F. Marquardt, editors. *Cavity Optomechanics: Nano- and Micromechanical Resonators Interacting with Light*. Quantum Science and Technology. Springer Berlin Heidelberg and Imprint: Springer, Berlin Heidelberg, 1st ed. 2014 edition, 2014. ISBN 9783642553127.

[56] R. Mukundan. *Moment functions in image analysis: Theory and applications*. World Scientific Pub. Co, Singapore, 1998. ISBN 9789812816092.

[57] L. Rocha, L. Velho, and P.C.P. Carvalho. Motion reconstruction using moments analysis. In A. de Albuquerque Araújo, editor, *XVII Brazilian Symposium on Computer Graphics and Image Processing*, pages 354–361, Los Alamitos Calif., 2004. IEEE Computer Society. ISBN 0-7695-2227-0. doi: 10.1109/SIBGRA.2004.1352981. URL https://ieeexplore.ieee.org/abstract/document/1352981.

[58] T. Fösel, V. Peano, and F. Marquardt. L lines, C points and Chern numbers: Understanding band structure topology using polarization fields. *New Journal of Physics*, 19(11):115013, 2017. ISSN 1367-2630. doi: 10.1088/1367-2630/aa8a9f. URL http://iopscience.iop.org/article/10.1088/1367-2630/aa8a9f.

[59] A. Bartels, R. Cerna, C. Kistner, A. Thoma, F. Hudert, C. Janke, and T. Dekorsy. Ultrafast time-domain spectroscopy based on high-speed asynchronous optical sampling. *The Review of scientific instruments*, 78(3):035107, 2007. ISSN 0034-6748. doi: 10.1063/1.2714048. URL https://aip.scitation.org/doi/full/10.1063/1.2714048.

[60] P. Stritt. *Weiterentwicklung und Anwendung eines ASOPS-Systems für die Festkörperspektroskopie*. Master's thesis, University of Konstanz, Konstanz, 2018.

[61] T. Oeckinghaus, S. A. Momenzadeh, P. Scheiger, T. Shalomayeva, A. Finkler, D. Dasari, R. Stöhr, and J. Wrachtrup. Spin-Phonon Interfaces in Coupled Nanomechanical Cantilevers. *Nano Letters*, 20(1):463–469, 2020. doi: 10.1021/acs.nanolett.9b04198. URL https://pubs.acs.org/doi/10.1021/acs.nanolett.9b04198.

[62] K. Makino, Y. Hashimoto, J.-I. Yoshikawa, H. Ohdan, T. Toyama, P. van Loock, and A. Furusawa. Synchronization of optical photons for quantum information processing. *Science advances*, 2(5):e1501772, 2016. doi: 10.1126/sciadv.1501772. URL https://advances.sciencemag.org/content/2/5/e1501772.

[63] I. Bargatin, E. B. Myers, J. S. Aldridge, C. Marcoux, P. Brianceau, L. Duraffourg, E. Colinet, S. Hentz, P. Andreucci, and M. L. Roukes. Large-scale integration of nanoelectromechanical systems for gas sensing applications. *Nano Letters*, 12(3): 1269–1274, 2012. doi: 10.1021/nl2037479.

[64] M. Jubitz. *Dielectric control of nanomechanical pillar resonators*. Master's thesis, University of Konstanz, Konstanz, 2018.

[65] M. H. Matheny, J. Emenheiser, W. Fon, A. Chapman, A. Salova, M. Rohden, J. Li, M. Hudoba de Badyn, M. Pósfai, L. Duenas-Osorio, M. Mesbahi, J. P. Crutchfield, M. C. Cross, R. M. D'Souza, and M. L. Roukes. Exotic states in a simple network of nanoelectromechanical oscillators. *Science*, 363(6431), 2019. doi: 10.1126/science.aav7932. URL https://science.sciencemag.org/content/363/6431/eaav7932.

[66] F. B. Johannsen. *Fabrication of GaAs nanopillars by inductively coupled plasma reactive ion etching*. Student's project report, University of Konstanz, Konstanz, 2020.

[67] M. Bückle. *Nanomechanical Systems Based on Tensile-Stressed Crystalline Indium Gallium Phosphide*. Doctoral thesis, University of Konstanz, Konstanz, 2020.

[68] H. Jansen, M. de Boer, R. Legtenberg, and M. Elwenspoek. The black silicon method: a universal method for determining the parameter setting of a fluorine-based reactive ion etcher in deep silicon trench etching with profile control. *Journal of Micromechanics and Microengineering*, 5(2):115–120, 1995. ISSN 0960-1317. doi: 10.1088/0960-1317/5/2/015. URL https://iopscience.iop.org/article/10.1088/0960-1317/5/2/015/meta.

[69] S. Aachboun and P. Ranson. Deep anisotropic etching of silicon. *Journal of Vacuum Science & Technology A: Vacuum, Surfaces, and Films*, 17(4):2270–2273, 1999. ISSN 0734-2101. doi: 10.1116/1.581759. URL https://avs.scitation.org/doi/10.1116/1.581759.

[70] H. Jansen, M. de Boer, H. Wensink, B. Kloeck, and M. Elwenspoek. The black silicon method. VIII. A study of the performance of etching silicon using SF6/O2-based chemistry with cryogenical wafer cooling and a high density ICP source. *Microelectronics Journal*, 32(9):769–777, 2001. ISSN 0026-2692. doi: 10.1016/S0026-2692(01)00039-8. URL http://www.sciencedirect.com/science/article/pii/S0026269201000398.

[71] M. J. de Boer, J.G.E. Gardeniers, H. V. Jansen, E. Smulders, M.-J. Gilde, G. Roelofs, J. N. Sasserath, and M. Elwenspoek. Guidelines for etching silicon MEMS structures using fluorine high-density plasmas at cryogenic temperatures. *Journal of Microelectromechanical Systems*, 11(4):385–401, 2002. ISSN 1057-7157. doi: 10.1109/JMEMS.2002.800928. URL https://ieeexplore.ieee.org/document/1022850.

[72] Laermer, F. (Stuttgart, DE), Schilp, A. Method of anisotropically etching silicon, . URL https://www.freepatentsonline.com/5501893.html.

[73] Laermer, F. (Stuttgart, DE), Schilp, A. Method for anisotropic etching of silicon, . URL https://www.freepatentsonline.com/6284148.html.

[74] Laermer, F. (Stuttgart, DE), Schilp, A. Method of anisotropic etching of silicon, . URL https://www.freepatentsonline.com/6531068.html.